Rocket system recovery using rotative wings

João Pedro Caldeira de Sousa Marques

Thesis to obtain the Master of Science Degree in

Aerospace Engineering

Supervisors: Prof. Filipe Szolnoky Ramos Pinto Cunha
Dr. Alain de Souza

Examination Committee

Chairperson: Prof. Afzal Suleman
Supervisor: Prof. Filipe Szolnoky Ramos Pinto Cunha
Member of the Committee: Prof. Luiz Carlos Sandoval Góes

November 2022

To my family and friends.

Declaration

I declare that this document is an original work of my own authorship and that it fulfills all the requirements of the Code of Conduct and Good Practices of the Universidade de Lisboa.

Acknowledgments

Firstly, I would like to thank Instituto Superior Técnico for the people and memories that it has given me, for the life lessons and for making me grow, both on a professional and personal level. I will always cherish these moments and the past years.

Secondly, an enormous thank you to Professor Filipe Cunha and Dr. Alain de Souza, for the relentless hours of discussion and for the guiding and transfer of knowledge during the production of this thesis.

An additional thank you to the Rocket Experiment Division team, for the data provided to perfect this work.

To all my friends, for standing by my side and for always distracting me with amusing moments, even in the moments of stress, thank you. I must also express my gratitude to my girlfriend, for tirelessly listening to my worries, for the motivation and for consistently inspiring me to be better and surpass myself everyday.

Finally, and most importantly, a huge thank you to my parents, sister and grandparents. They have blessed me with continuous education, dedication, support and love through my whole life, which I hope to fully repay one day.

Resumo

Neste trabalho, a viabilidade da recuperação de naves espaciais utilizando asas rotativas é analisada. Esta tecnologia baseia-se no fenómeno de autorrotação, no qual o rotor não tem motor associado. Possui a capacidade de efetuar aterragens seguras e controladas, permitindo a reutilização do foguetão em diferentes missões.

De modo a cumprir o objetivo, desenvolveu-se um modelo computacional que simula a descida do primeiro estágio de um foguetão. Baseia-se em teorias aerodinâmicas de rotores e cinemática e determina diversos parâmetros do rotor que possibilitam a análise da performance do sistema. Além disso, recorre também a dados experimentais para aumentar a exatidão dos resultados. A verificação do modelo efetuou-se através da comparação do seu comportamento com dados da literatura.

Os estudos consideraram a recuperação de uma sonda existente. Para compreender como cada parâmetro de design influencia o sistema, realizou-se um estudo paramétrico das principais variáveis do rotor. Concluiu-se que o ângulo de picada das hélices é extremamente importante para a performance do sistema e deve ser cuidadosamente selecionado, e que aumentos de massa resultantes de raios excessivos das hélices podem ser prejudiciais.

Além disso, realizou-se uma otimização com o objetivo de minimizar a velocidade terminal do foguetão e o design obtido reduziu a velocidade em 72.7%, em comparação com a velocidade inicial. Finalmente, uma manobra de flare foi demonstrada para reduzir a velocidade de aterragem, resultando numa velocidade terminal de $3.89\ m/s$.

Concluiu-se que este sistema de recuperação é altamente promissor, embora careça de trabalhos futuros em várias áreas de estudo.

Palavras-chave: Sistemas de Recuperação de Foguetões, Dinâmica de Autorrotação, Asas Rotativas, Sistemas de Recuperação em Autorrotação, Otimização do Design de Sistemas de Recuperação

Abstract

In this work, the feasibility of spacecraft recovery using rotative wings is analysed. This technology is based on the autorotation phenomenon, in which the rotor is driven without power associated. It possesses the ability to perform a safe and controlled landing, allowing the spacecraft to be reused and utilised in missions with different requirements.

To fulfill the objective, a computational model that simulates the descent of a rocket's first stage was developed. It is based on rotor's aerodynamic theories and kinematics and computes several rotor parameters that allow the analysis of the system's performance. Moreover, it resorts to experimental data to increase the results' accuracy. The model's verification was successfully carried out by comparing its behaviour with literature data.

The studies considered the recovery of an existing sounding rocket. To understand how each design parameter influences the system, a parametric study of the rotor design variables was held. It was concluded that the blade's pitch angle is extremely important for the system's performance and should be carefully selected, and that weight penalties resultant from excessive blade's number or radius can be prejudicial.

Furthermore, a design optimisation was conducted, aiming to minimise the rocket's terminal velocity. The optimised solution decreased the terminal velocity by 72.7%, in comparison to the initial velocity. Finally, a flare manoeuvre was disclosed to reduce the touchdown velocity, resulting in a terminal velocity of $3.89\ m/s$.

This recovery system is concluded to be highly promising, though requiring further work in several fields of study.

Keywords: Rocket Recovery Systems, Autorotation Dynamics, Rotative Wings, Autorotation Recovery Systems, Recovery System Design Optimisation

Contents

Acknowledgments . . . vii
Resumo . . . ix
Abstract . . . xi
List of Tables . . . xv
List of Figures . . . xvii
Nomenclature . . . xxi
Glossary . . . xxv

1 Introduction 1
1.1 Motivation . . . 1
1.2 Topic Overview . . . 2
1.3 Objectives . . . 3
1.4 Thesis Outline . . . 4

2 Literature Review 5
2.1 Autorotation . . . 5
2.2 Payload Recovery Methods . . . 7
2.3 Recovery Using Rotative Wings . . . 9
  2.3.1 Early Concepts . . . 9
  2.3.2 Kaman's *Rotochute* . . . 9
  2.3.3 NASA's Wind Tunnel Testing . . . 14
  2.3.4 Space Rotor . . . 15
  2.3.5 NASA Ames Research Center's Program . . . 15
  2.3.6 Rotary Rocket's *Roton* . . . 18
  2.3.7 Recent Concepts . . . 19
2.4 Comparison of Recovery Methods . . . 22

3 Methods 24
3.1 Autorotation Aerodynamic Analysis in Axial Flight . . . 24
3.2 Computational Model . . . 30
  3.2.1 Axial Induced Velocity in Axial Flight . . . 40
  3.2.2 Model Verification . . . 42

3.2.3 Mesh Study 51
3.3 Genetic Optimisation 54

4 Computational Experiments **55**
4.1 *Baltasar* Sounding Rocket 55
4.2 Parametric Study 56
4.2.1 Variation of R 56
4.2.2 Variation of N_b 60
4.2.3 Variation of θ 64
4.3 Genetic Optimisation 70
4.4 Optimised Solution 72
4.4.1 Collective Flare Manoeuvre 76

5 Conclusions **78**
5.1 Achievements 78
5.2 Future Work 79

Bibliography **81**

A Model Flowchart **87**

B Axial Induced Velocity Study **89**

List of Tables

2.1 Comparison between the main existent recovery methods and rotative wings. 23

3.1 Rotor's design parameters for the verification of the model. 43
3.2 Parameters of the simulation for the verification of the model. 43
3.3 Values of dx and dt selected to perform the mesh study. 51
3.4 Values and errors obtained for the final values of v_v, a_v and a_{ang} in the dx mesh study. . . 53
3.5 Values and errors obtained for the final values of v_v, a_v and a_{ang} in the dt mesh study. . . 54

4.1 Initial fixed conditions for the simulations run for the RED's rocket, *Baltasar*. 56
4.2 Parameters of the simulation for the parametric study. 56
4.3 Rotor's design parameters for the R variation study. 57
4.4 Values of the terminal v_v for each R and its percentage decrease from $v_{v_{deploy}}$. 60
4.5 Rotor's design parameters for the N_b variation study. 60
4.6 Values of the terminal v_v for each N_b and its percentage decrease from $v_{v_{deploy}}$. 64
4.7 Rotor's design parameters for the θ variation study. 64
4.8 Values of the terminal v_v for each θ and its percentage decrease from $v_{v_{deploy}}$. 70
4.9 Design variables and respective bound constraints for the genetic optimisation. 70
4.10 Design variables that resulted in the optimised solution. 71

List of Figures

2.1 Scheme of the *Autogiro*. The unpowered rotor provides both lift and propulsion forces [16]. 6

2.2 First Apollo parachute drop test, in May of 1963 [21]. 7

2.3 Landing of the Space Shuttle Discovery at NASA's Kennedy Space Center, in 2001 [23]. . 8

2.4 Controlled descent of the side boosters of SpaceX's Falcon Heavy [25]. 9

2.5 Kaman Model *KRC-6M Rotochute* under wind tunnel testing [28]. 10

2.6 Phases of operation during the recovery of Kaman's *Rotochute* [12]. 11

2.7 Rotor's drag coefficient variation with axial advance ratio and solidity [12]. 12

2.8 Variation of the rotor's mass percentage with disk loading and rotor solidity [12]. 12

2.9 KRC-6 *Rotochute* Test Vehicle [12]. 13

2.10 Telescopic (top) and flexible inflatable (down) blade concepts [12]. 13

2.11 Unstable (left), marginally stable (centre) and stable (right) configurations, in which the difference between the corresponding models is the hub inertia [31]. 14

2.12 Configurations of hypersonic gliders (Space Rotor) proposed [32]. 15

2.13 Autorotation dimensionless tip velocity ratio with blade pitch angle, for a typical low velocity operation (left) and predicted by theory using Newtonian flow for supersonic velocities (right) [33]. 16

2.14 Rotor vehicle operating modes proposed by Smith and Levin [33]. 17

2.15 Variation of the capsule's drag coefficient with and without the rotor, with Mach number [37]. 18

2.16 Proof of concept for the Mars rotor developed by NASA Ames [39]. 20

2.17 Capsule with rotor proposed by Hagen [2]. 20

3.1 Side view of a blade element in autorotation, in axial flight, according to the BET. Adapted from [9]. 26

3.2 Top view of the blade in autorotation, in axial flight. Adapted from [9]. 26

3.3 Blade regions during an axial autorotative descent [10]. 28

3.4 Blade regions and respective aerodynamic forces, for an axial autorotative descent [10]. . 29

3.5 Effect of the blade's θ on the resultant force F_{res} and, consequently, on Q. Adapted from [42]. 30

3.6 CAD model of the autorotation recovery system developed by the students [52]. 31

3.7 Coordinate system of the first stage's body. Adapted from [2]. 32

3.8 $C_{d_{stage}}$ of the first stage as a function of its $AR = (Lt/Dm)_{stage}$. Data collected from [53]. 34

3.9 Atmospheric parameters variation with h. Data extracted from NRLMSIS 2.0 [54]. 35
3.10 C_l and C_d stall data as a function of α used in the original model. The C_l function (red) was computed as a quadratic function and the C_d function (blue) was considered to be a linear function [52]. 37
3.11 C_l (red) and C_d (blue) as a function of α for $Re = 2.5 \cdot 10^5$, for the selected approach. . . . 38
3.12 Moment of inertia, I, for a thin rectangular plate with respect to the x-axis, used for the calculation of I_{blade}. Adapted from [59]. 39
3.13 Induced velocity ratio, v_i/v_h, as a function of the climb velocity ratio, V_c/v_h, in which the windmill brake state and the vortex ring state zones are observable [9]. 41
3.14 Evolution of h (a), v_v (b), a_v (c), g force (d), ω (e) and a_{ang} (f) with t for the verification of the model. 44
3.15 Evolution of a_v (a) and a_{ang} (b) with t, with the second acceleration peak highlighted. . . . 45
3.16 Spanwise distribution of the α of a blade's element for $t = 3.41\ s$, $t = 3.87\ s$ and $t = 116.69\ s$. 46
3.17 C_{d_R} variation with λ_{axial}, indicating a clear transition between the state of full stalled blades and partially stalled blades, noticeable by the sudden increase of C_{d_R}. 47
3.18 C_{d_R} (a) and λ_{axial} (b) evolution with t for the verification of the model. 47
3.19 Evolution of T (a) and Q (b) with t for the verification of the model. 48
3.20 Spanwise distribution of the dQ of a blade's section in autorotation (equilibrium). 49
3.21 Spanwise distribution of the dT of a blade's section in autorotation (equilibrium). 50
3.22 Evolutions of v_v (a), a_v (b), ω (c) and a_{ang} (d) with time for the different dx's studied. . . . 52

4.1 The sounding rocket *Baltasar*. Image provided by the RED team. 55
4.2 Evolution of v_v with t for the several R's studied. 57
4.3 Evolution of a_v with t during the first seconds of the simulation, for the several R's studied. 57
4.4 Evolution of ω with t for the several R's studied. 59
4.5 Evolution of a_{ang} with t during the first seconds of the simulation, for the several R's studied. 59
4.6 More detailed evolution of a_{ang} with t, for the several R's studied. 59
4.7 Evolution of v_v with t for the several N_b's studied. 61
4.8 Evolution of a_v with t during the first seconds of the simulation, for the several N_b's studied. 61
4.9 Evolution of ω with t for the several N_b's studied. 62
4.10 Evolution of a_{ang} with t during the first seconds of the simulation, for the several N_b's studied. 63
4.11 C_{d_R} variation with λ_{axial} for the several N_b's studied. 63
4.12 Evolution of v_v with t for the several θ's studied. 65
4.13 Evolution of a_v with t during the first seconds of the simulation, for the several θ's studied. 65
4.14 Evolution of v_v with t during the first seconds of the simulation, for the several θ's studied. 66
4.15 Evolution of λ_{axial} with t during the first seconds of the simulation, for the several θ's studied. 66
4.16 Evolution of ω with t for the several θ's studied. 67
4.17 Evolution of a_{ang} with t during the first seconds of the simulation, for the several θ's studied. 67

4.18 Spanwise distribution of the α of a blade's element for $\theta = -10°$, $\theta = -4°$ and $\theta = -2°$ . . 68
4.19 Variation of the equilibrium Ω^* (a) and C_{d_R} (b) with θ, demonstrating the clear differences between a partially stalled and fully stalled operation. 69
4.20 Minimum and mean values of v_v for each generation. 71
4.21 Evolution of h with t for the GA solution. 73
4.22 Evolution of v_v with t for the GA solution. 73
4.23 Evolution of a_v with t for the GA solution. 73
4.24 Evolution of ω with t for the GA solution. 74
4.25 Evolution of a_{ang} with t for the GA solution. 74
4.26 Evolution of T (a) and Q (b) with t for the GA solution. 75
4.27 Spanwise distribution of the dQ of a blade's section in the last moment of the simulation. . 75
4.28 Evolution of C_{d_R} with λ_{axial} for the GA solution. 76
4.29 Evolution of v_v with t for the last seconds of the simulation, highlighting the effect of performing a collective flare manoeuvre. 77
4.30 Evolution of a_v with t for the last seconds of the simulation, highlighting the effect of performing a collective flare manoeuvre. 77

A.1 Flowchart representing the model's framework following the deployment of the rotor. . . . 88

B.1 Evolution of v_v with t for the v_i study. 89
B.2 Evolution of a_v with t in the first seconds of the simulation, for the v_i study. 90
B.3 Evolution of ω with t for the v_i study. 90
B.4 Evolution of a_{ang} with t in the first seconds of the simulation, for the v_i study. 91
B.5 Evolution of C_{d_R} with λ_{axial} for the minimised solution. 91

Nomenclature

Greek symbols

α	Angle of attack
α_{crit}	Critical angle of attack
λ_{axial}	Axial advance ratio
μ	Air dynamic viscosity
ω	Angular velocity of the rotor
Ω^*	Dimensionless tip speed
ϕ	Induced angle of attack
ρ	Air density
σ	Solidity of the rotor
θ	Collective pitch angle of the blades

Roman symbols

A_b	Area of a blade
a_v	Acceleration of the system
a_{ang}	Angular acceleration of the rotor
A_{base}	Area of a cylinder’s base
A_{disk}	Disk area
AR	Aspect ratio of a cylinder
c	Chord of a blade
C_d	Coefficient of drag
C_l	Coefficient of lift
C_{d_R}	Rotor’s coefficient of drag

$C_{d_{stage}}$	Coefficient of drag of the rocket’s body
c_{sound}	Velocity of sound
D	Drag force
$d*$	Infinitesimal force or moment (applicable to all)
D_{stage}	Drag force of the rocket’s body
dA	Area of a blade element
DL	Disk loading of the rotor
Dm_{stage}	Diameter of the rocket’s first stage
dt	Time step of the simulation
dx	Length of a blade element
F_y, F_z	Vertical and horizontal forces on the blade
F_{res}	Resultant force on the blade
G	Gravitational constant
g	Gravitational acceleration
h	Rocket’s height
I_{blade}	Moment of inertia of a blade
I_{rotor}	Moment of inertia of the rotor
L	Lift force
Lt_{stage}	Length of the rocket’s first stage
m	Total mass of the system
$m_{control}$	Mass of the control system
m_{Earth}	Mass of the Earth
$m_{recovery}$	Mass of the recovery system
m_{rotor}	Mass of the rotor
m_{stage}	Mass of the rocket’s first stage
M_{tip}	Tip Mach number
N_b	Number of blades
$n_{sections}$	Number of sections of a blade

Q	Torque
R	Span of a blade/Rotor's radius
R_{Earth}	Radius of the Earth
Re	Reynolds number
T	Thrust force
t	Time
Tp	Temperature
U	Resultant velocity on a blade element
U_P	Axial velocity on a blade element
U_T	Radial velocity component on a blade element
V_c	Axial velocity of the airflow relative to the vehicle
v_h	Hover velocity
v_i	Axial induced velocity
v_v	Velocity of the system
V_{tip}	Tip velocity
W	Weight
x	Spanwise coordinate of the blade
x/R	Nondimensional spanwise coordinate of the blade

Subscripts

0	Initial conditions
$deploy$	Deploy conditions
x, y, z	Cartesian components

Superscripts

'	Rocket's coordinate system

Glossary

ARMADA AutoRotation in Martian Descent and Landing is a project consisting of an EDLS that studies the feasibility of rotative wings for Mars' exploration.

BET Blade Element Theory is a mathematical process that predicts the behaviour of propellers by dividing a blade into several infinitesimal sections, calculating the forces on such sections and integrating them along the whole blade.

CAD Computer-Aided Design is a software that assists on the creation, alteration, analysis or optimisation of a design.

CEV Crew Exploration Vehicle was a NASA component designed to transport humans to space.

CFD Computational Fluid Dynamics is a branch of fluid mechanics that uses numerical methods and algorithms to solve problems involving fluid flows.

EADS European Aeronautic Defence and Space Company Astrium was an aerospace manufacturer specialised in civil and military space systems and services.

EDLS Entry, Descent and Landing System is a system that assures, as the name suggests, the entry, descent and landing. It is composed by thermal protection, deceleration and recovery systems and by the landed vehicle itself.

ESA European Space Agency is an intergovernmental organisation of 22 European countries for the space exploration and research.

GA Genetic Algorithm is a heuristic method for solving optimisation problems. It is based on the evolutionary biological process of natural selection, in which the most capable individuals of a population prosper, reproduce and mutate, successively approaching an optimised solution.

LEO Low Earth Orbit is an orbit which is close to the Earth's surface, between 160 km and 1000 km. It is mostly used for satellite imaging.

NACA National Advisory Committee for Aeronautics was a United States federal agency for aeronautical research and the predecessor of NASA.

NASA National Aeronautics and Space Administration is the current United States federal government agency for the civil space program, aeronautical research and space research.

RED Rocket Experiment Division is a team of students from Instituto Superior Técnico, whose goal is the design, building and launch of model-rockets for international university competitions.

RPM Revolutions Per Minute is a unit of rotational velocity around a fixed axis, representing the number of rotations performed in one minute.

SSTO Single-Stage-To-Orbit is a concept vehicle that reaches orbit without the expense of its stages, tanks or engines.

Chapter 1

Introduction

1.1 Motivation

Ever since the dawn of space travel, recovery of spacecrafts has always played an important role in space missions. Even though going to space was and still is an exciting and ground-breaking achievement, it is also necessary to come back to Earth intact. This area requires as much investigation and testing as sending a spacecraft to orbit. Whether for returning the astronauts to Earth in manned spacecrafts, for recovering payloads from space exploration or for landing rocket's first stages or boosters to be reused, recovery is fundamental [1].

The most commonly used method of recovery is the well-known parachute. Over the years, it offered great reliability and the ability to safely decelerate the vehicles until a more or less soft landing [1]. Furthermore, it is a lightweight and simple solution. However, it has a major drawback: the rate of descent and flight path can not be controlled. This means that the spacecraft's descent can not be piloted, neither its velocity can be changed. It also presupposes that it is not possible to exactly predetermine the spacecraft's landing site, what brings a degree of uncertainty to this phase of the mission [2, 3].

Apart from the recovery itself, the reusability of the recovered parts has always been a discussed possibility [1]. Such development would massively reduce the operational launch cost, allowing for more launches per year and thus a higher number of missions [4]. In the past decade, the space industry has been increasingly shifting towards commercialisation and searching for solutions that can make the enterprises economically sustainable. For this reason, efforts have been made for the recovery of boosters or first stages of rockets, allowing for its reuse on several flights, which is even opening the doors for space tourism. Even though parachutes can achieve this goal in certain missions by dropping the part in the sea, where it will be recovered, this method comes with high operational costs [1].

Nowadays, the most successful technology to achieve this purpose is the controlled and autonomous vertical landing of rockets performed by private space companies, like SpaceX [5]. In this recovery method the rocket has its re-entry, descent and landing controlled by extra grid fins and its deceleration assured by the thrust produced by its engines. It represents a major engineering advance in the extent that the spacecraft can be autonomously returned to Earth with a controlled trajectory and rate of descent and eventually land precisely on a predetermined landing site with a close to zero touchdown velocity. This allows to save millions of dollars per flight [6, 7]. However, it also brings disadvantages: it requires the addition of extra fuel specifically for the descent, reducing the payload that the spacecraft can carry and having extra costs by simply carrying and using the referred fuel.

Considering that neither of the referred methods are completely advantageous, the technology available today might be advanced enough to investigate and search for more economical and, above all, flexible recovery methods that solve these disadvantages, such as a rotative wings recovery system.

This application of rotative wings was mainly considered in the second half of the last century, during the space race, having eventually fallen into oblivion. One of the reasons behind this was the lack of technology and knowledge at the time. Nevertheless, all the researchers revealed a great amount of confidence on the capabilities of such method, which showed promising results. The conclusions taken by such authors indicate that, if investigations on this topic were to be made today, maybe the outcome would be different. This it the question that drives this thesis.

1.2 Topic Overview

The recovery of spacecrafts resorting to rotative wings is, in simple words, the deceleration, guiding and landing of space vehicles resorting to a helicopter rotor under autorotation operation, which is mounted on the vehicle and is deployed during the descent.

Autorotation is a state of flight utilised mainly in helicopters, in which the main rotor is driven exclusively by aerodynamic forces, with no power being provided by the engine [8]. The energy that drives the rotor is originated from potential energy converted into kinetic energy from the air flowing upwards through the vehicle [9]. Considering this, it is currently used in helicopter flights, particularly in the event of an engine, transmission or tail rotor failure, allowing for a safe emergency landing. Nowadays, all helicopters require a capability for autorotation to achieve certification [10]. Autorotation is widely studied and its underlying aerodynamics are explained by well accepted analytical theories [9, 11].

This method has certain advantages that make it promising and that have been discussed by several authors, in studies that will be described further on this document [2, 12–14]. Such advantages include:

- High drag, which translates into high deceleration;
- Gliding capability at low velocities, with favourable L/D (lift/drag) ratios and substantial lateral range;
- Manoeuvrability and controlled flight;
- Near zero vertical and horizontal velocities at landing, allowing for an impact with controlled timing and low energy absorption by the vehicle;
- Safe flight and minimal vehicle damages which enable reusability;
- Landing accuracy as for the landing site location;

- Flexible regarding abort situations, such as weather conditions and unexpected change of landing site (hazard avoidance);
- Capability to adjust the descent velocity;
- Low weight penalties suggested by the literature;
- Low operational costs due to the reusability of both vehicle and recovery system;
- Wide range of applications, due to its manoeuvrability and velocity control;

Regarding the disadvantages, there are still some doubts concerning the vehicle and rotor's stability in all operating conditions, which requires additional study. Furthermore, the cost of development and production can be higher than in some of the other existent methods, requiring investment [2].

Considering the advantages of this system, it can potentially represent a breakthrough both in the economics and safety of space transportation, since the idea is conceivable and of relative simplicity [2]. Furthermore, this simplicity and the low weight penalty expected mean that rotative wings might have a lower life cycle cost in comparison to other methods, enabling the possibility to resort to less powerful launchers for the mission to be fulfilled, or to carry higher payloads [15]. In addition, it has the capability to be applied to a wide range of missions [2, 12–14], such as:

- Spacecraft recovery, providing deceleration for the guided delivery and landing of boosters, rocket's stages, manned capsules or payloads, for distinct missions with diverse requirements and conditions;
- Landing on other planets apart from Earth, with different atmospheric conditions;
- Air dropped packages, delivering supply packages dropped from aircrafts to a given location;
- Commercial applications, such as space tourism services;
- Atmospheric research, provoking the retardation of atmospheric probes and allowing for adjusting the descent velocity, which would favour the referred research.

1.3 Objectives

The main objective of this thesis is to address the feasibility of using a rotative wings system for the recovery of spacecraft, discussing its advantages and disadvantages and comparing it with the other traditional methods.

With this intention, a computational model should be developed, which should also offer the possibility to analyse the performance of the system, culminating in a design optimisation.

In order to achieve the proposed objective, the following milestones should be fulfilled:

- Perform a literature review of the topics in order to understand its historical and technical context, the methods used and parameters of analysis;

- Develop a computational model of an autorotative recovery system applied to the recovery, descent and landing of the first stage of a rocket or sounding rocket;
- Verify the model, taking into account the theory and literature review;
- Create the simulation environment, by selecting proper initial conditions for the analysis to be carried out;
- Perform a parametric study to understand the changes provoked by the variation of certain design variables;
- Conduct an optimisation to achieve an optimum design for the system's rotor;
- Analyse the performance of the vehicle and rotor for the optimised design;
- Address the feasibility of the recovery method, considering the studies performed and the results of the optimised solution obtained;
- Compare the method to other recovery methods and discuss its comparative advantages.

The contributions of this work will be the proof of concept on the feasibility of the rotative wings recovery method, from an extensive literature review to the developed model and results obtained in its analysis. The model has the capability to be used for the study of different missions and the flexibility to be further developed in the future with the adding of features that make it more realistic. The major deliverables are the computational model that can be enhanced, as well as the results and conclusions obtained from the performance analysis.

1.4 Thesis Outline

Firstly, chapter 2 consists of an extensive literature review, which is necessary in order to understand autorotation studies and its application on spacecraft recovery, since this operation is, to some extent, little known and studied.

Chapter 3 focuses initially on presenting the theoretical aerodynamics behind autorotation. It then moves to the description of the computational model developed, which is based on such theory, and presentation of the methods used on its conception. The model's verification and mesh studies are also carried out in this chapter.

Following the model's description, chapter 4 displays the computational set-up for each experiment, with the respective description as well as its initial variables and conditions, and the obtained results for each simulation. The results are accompanied by an analysis of the system's performance and conclusions taken for each study. It firstly covers a parametric study, moving then to a design optimisation, discussion of the attained outcome and demonstration of a manoeuvre to improve the results.

Lastly, chapter 5 presents a summary of the conclusions taken from the analysis of the results, as well as suggestions for future developments on the work.

Chapter 2

Literature Review

The following section covers the current state of the art on the use of rotative wings for the recovery of rocket's payload and/or rocket's first stages. This is one of the many applications of rotative wings that has been widely studied ever since the space race, which started in the fifties. Thus, it is important to understand the story behind the theme and how it evolved, as well as the main conclusions of the analysis and experiments conducted over the years of research.

However, it is first necessary to better comprehend the studies on the phenomenon of autorotation, which is behind the functioning of these systems, and the evolution of recovery methods, in order to acknowledge the impact that recovery using autorotative systems can have on the space industry.

That being the case, this chapter will be divided into four sections: autorotation, spacecraft recovery systems, spacecraft recovery using rotative wings and comparison of recovery methods.

2.1 Autorotation

According to Professor Gordon Leishman [9], the Italian Gaetano Crocco and the Russian Boris Yuriev were some of the pioneers on the investigation of this phenomenon, having observed autorotation on rotors circa 1910. The Russian scientist and his students conducted important studies on model helicopter rotors and showed that, under specific conditions of descending and horizontal flight and with the rotor at a positive angle of attack, the rotor could self-rotate without power and eventually be used for safe emergency landings. This phenomenon was baptised as “rotor gliding” [16].

In 1922, Max Munk [17] of the National Advisory Committee for Aeronautics (NACA) led a series of model tests on helicopter propellers functioning as windmills. Through these experiments, autorotation was once again observed, with the rotor reportedly having a decelerating effect 1.5 times as great as that of an ordinary parachute with the same diameter, under the same airstream conditions.

The first personality to consider the implementation of an unpowered rotor into an aircraft in its normal flight was the Spaniard Juan de la Cierva. In 1919 his aircraft, the C-3, stalled and crashed during a presentation flight [16]. Following the crash, de la Cierva began contemplating manners to eliminate stall and consequently increase the flight safety of an aircraft flying at low airspeeds and, specially, close to the ground. He stated that "*the wings of such an aircraft should be moving in relation to the fuselage. The only mechanism able to satisfy this requirement is a circular motion and, moreover, in order to give adequate security to the aforementioned requirement it must be independent of the engine. It was thus necessary that these rotary wings were free-spinning and unpowered.*" (cited by G. Leishman [16]). In 1920, de la Cierva built a free-flying model of a rotative wing vehicle with horizontal and vertical tails for stability and with the rotor being allowed to free spin. During a drop test, the rotor spun freely and allowed for the model to glide until a safe and soft landing [16].

Thus, after several developments, the *Autogiro* (currently *Autogyro*, from the Greek $\alpha\upsilon\tau o\varsigma$ and $\gamma\upsilon\rho o\varsigma$, "self-turning") was born and its first flight was in early 1923 [18]. This innovative aircraft was constituted both by a propeller in its front, which provided forward propulsion, and a rotor on the top, self-rotating due to the airstream and providing both lift and propulsion, as seen in figure 2.1. This type of vehicle would always operate in the autorotative working state and its low disk loading (ratio between the weight of the vehicle and the area swept out by the rotor) meant that only a small upward flow would be sufficient to produce autorotation. It would also require only minimal forward airflow to maintain the flight and, in case of an engine loss, a safe descent would be achieved thanks to the autorotation phenomenon [16].

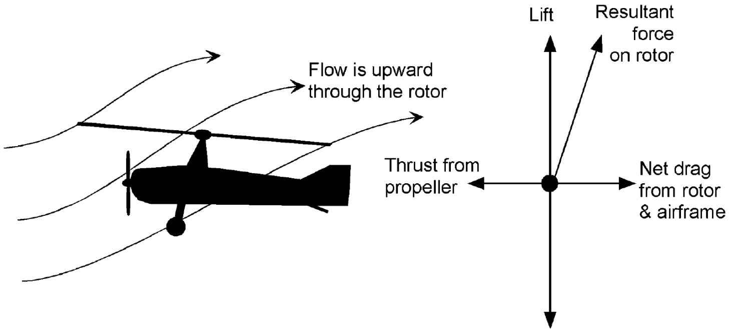
Lift
Resultant force on rotor
Flow is upward through the rotor
Thrust from propeller
Net drag from rotor & airframe

Figure 2.1: Scheme of the *Autogiro*. The unpowered rotor provides both lift and propulsion forces [16].

Being one of the first to better understand the aerodynamics behind autorotation, de la Cierva conducted some of the first theoretical studies on rotors and a series of wind tunnel tests [9] and was able to demonstrate that the *Autogiro* was safe, capable of eliminating stall and, as a result of its low velocities, able to land in enclosed areas [16].

In the subsequent years, autorotation was widely studied and numerous theoretical, experimental and computational works exist, just like the one by Seter and Rosen [19]. Several books regarding helicopter aerodynamics and performance extensively explain the theory behind autorotation [9, 11].

Something somewhat curious is that, as many other physical phenomena studied in engineering, the autorotation state is present in the nature, in the flight of seeds such as maple or sycamore. The flight of samara seeds was analysed by Azuma and Yasuda [20]. The seeds tested in a wind tunnel showed a good aerodynamic performance, with a low descent rate despite of the high wing loading, because of the high rotational velocities. The researchers could understand that the span and area of the "blades", mass of the seed, airfoil, position of the centre of mass and moment of inertia of the seed were all highly connected to the performance of the descent.

2.2 Payload Recovery Methods

During the space race, engineers were already interested in reusing spacecrafts, but such reality was never accomplished until the Space Shuttle, some years ahead. Since the dawn of spacial flights, researchers have always revealed a preference for landable winged return vehicles, that would fly with wings and land on a runway, named spaceplanes. Such vehicles would allow for corrective control, guidance and attitude control, with a L/D ratio (lift/drag ratio) different than 0 [1].

During the National Aeronautics and Space Administration's (NASA) Project Gemini (1961 to 1966), the concept of a paraglider, a deployable and inflatable wing that would turn the capsule into a glider, allowing for a controlled descent and landing on a runway, was considered. Nevertheless, control, stability, manoeuvrability and deployment issues were encountered on many of the conducted tests. The parasail, a midterm concept between the paraglider and the parachute which offered limited manoeuvrability, was also studied and flown successfully, but was always seen as a secondary option [1].

Thus, the rush provoked by the space race and the lack of knowledge and resources for a better and fastest option resulted in the capsules' recovery being assisted by parachutes. The American space programs Mercury, Gemini and Apollo (see figure 2.2) all opted to use parachutes, as well as the Soviet and Chinese manned spacecrafts until the Space Shuttle [1].

Typically, the drogue parachute was firstly deployed, intended for an initial deceleration but mainly for stabilisation of the spacecraft, while the remaining parachutes were deployed later for deceleration and landing. The parachute had the disadvantage of not allowing its manoeuvrability and control for adequate targeting of the landing site. Furthermore, it provoked expensive recovery operations when assisting landings in the sea and did not accomplish to avoid hard landings when on land. On the other hand, it was an effective and relatively simple engineering solution [1].

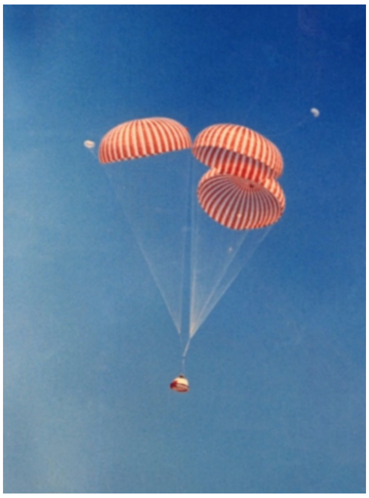

Figure 2.2: First Apollo parachute drop test, in May of 1963 [21].

During the Apollo program, researchers at NASA persisted on attempting to conceive a spaceplane. After many years of design, construction and testing, the Space Shuttle came to life, with its first flight being successful in 1981, allowing for an unpowered landing on a runway [1], as seen in figure 2.3.

The Space Shuttle was a delta-winged vehicle built with innovative materials and technologies for thermal protection. After a flight, the spacecraft would go through maintenance and refurbishing and could be flown in future missions [1]. Moreover, the rocket boosters powering the launch of the Space Shuttle would fall into the ocean assisted by parachutes, and would also be recovered and reutilised [22].

Figure 2.3: Landing of the Space Shuttle Discovery at NASA's Kennedy Space Center, in 2001 [23].

Following the referred engineering events, the most relevant and revolutionary advances on the recovery area were the developments conducted by SpaceX. In 2015, SpaceX's Falcon 9 rocket had its first stage returned to the launching pad, being the first orbital class rocket to do so [6].

The recovery is guaranteed through a controlled and autonomous descent, which is a combination of thrust from the engines and control from the grid fins. During the stages' separation, the first stage is shutoff and thrusters steer the stage to prepare it for the descent, phenomenon that is repeated when the stage reaches the Earth's atmosphere. At the same time, the grid fins are deployed, controlling the orientation of the rocket, and the engine is turned on, creating a heat shield and decelerating the body. This process terminates with a precise and smooth touchdown on a predetermined landing site, consisting on a final deceleration provoked by the thrust provided by the engines, and on the deployment of retractable legs, not only for maintaining the rocket's stable position after landing but also to reduce the impact force [1, 7]. Following its recovery, the stage is inspected and refurbished for further reuse.

In 2017, SpaceX recovered a first stage that was being reused for the first time. Following such success, it also accomplished to land two side boosters of the Falcon Heavy spacecraft, which is observable in figure 2.4 [5]. Finally, the company is currently under testing for the Starship, a fully reusable rocket which will potentially be the most powerful space vehicle in history [24].

In a controlled descent recovery, the mission demands that the rocket possesses enough fuel for the descent, so that the engine burnout (extinction of fuel) does not occur before it. Moreover, a compromise is necessary due to the cost and mass penalties of the additional fuel for landing. For instance, in missions that require the reuse of the first stage the payload must be reduced to comply with the additional mass penalties, meaning that for missions that require a heavy payload, reusability is not possible.

Nevertheless, such cost is substantially lower than the cost of losing the totality of the stage [6].

Figure 2.4: Controlled descent of the side boosters of SpaceX's Falcon Heavy [25].

2.3 Recovery Using Rotative Wings

Being the theme of this thesis, recovery using rotative wings is this chapter's theme that requires more attention as for its developments over the years.

2.3.1 Early Concepts

According to Smith and Levin [13], the first known works in the area are attributed to Igor Bensen [26] and the General Electric Co., who performed theoretical and experimental studies on high altitude rockets. These studies were conducted on the *Rotochute*, a rotary wing air brake aimed to function as an aerodynamic decelerator for rockets.

A model of the *Rotochute* was tested on a supersonic (typically between Mach numbers of 1.2 and 5) wind tunnel in axial flight (airflow normal to the plane of rotation of the blades), since it was expected to function under re-entry conditions [26]. The objective was to assess whether the rotor would be capable of beginning and maintaining its rotary motion. If so, further measurements of drag, rotor RPM (Revolutions Per Minute), coning angle (angle between the rotation plane of the blades and the plane normal to the rotor shaft axis, caused by a sweep of the rotor blades produced by lift and centrifugal forces [10]) and other relevant parameters would be made. These tests were a success since the rotor started its motion instantaneously and sustained a deceleration up to $52\ g$'s, which was a much higher value than the expected [26].

2.3.2 Kaman's *Rotochute*

The promising capabilities reported above led to further developments on the *Rotochute* by the Kaman Aircraft Corporation, in the fifties. This gave birth to the Kaman *Rotochute* vehicles, which were helicopter type rotor systems with two or more blades, used for a controlled aerodynamic retardation and payload recovery in an autorotative descent [13].

These developments included a wind tunnel investigation conducted by a NACA researcher [27], with the purpose of determining the drag, rotational velocity and opening characteristics of a Kaman *Rotochute*'s model, simulating constant rates of descent for subsonic Mach numbers (below Mach number of 0.8) in axial flight. The deployment of the *Rotochute* was verified and the evolution of the drag and rotor revolutions, from the rotor's opening until obtaining a constant rotation velocity, was also observed.

Likewise, the operational feasibility of the Kaman Model *KRC-6M Rotochute* (figure 2.5) was investigated by Professor Norman Ham [28], resorting to wind tunnel testing at transonic (typically between Mach numbers of 0.8 and 1.2) and supersonic regimes, up to a Mach number of 1.5. The feasibility was proved, with the deployment and final governed rotational velocity being successfully achieved. Furthermore, no unusual forces or moments were detected (the lateral forces and moments were small) and the governing characteristics revealed to be predictable theoretically. One interesting conclusion taken from this investigation is the fact that the rotor drag coefficient is dependent on its solidity (ratio between the blades' area and disk area, which is the circular area swept by the rotor), increasing with it [28]. A significant characteristic of the described models was the capability to control the blades' pitch angle (angle at which the rotor blades are set with respect to the plane of rotation) and therefore the rotational velocity [27, 28].

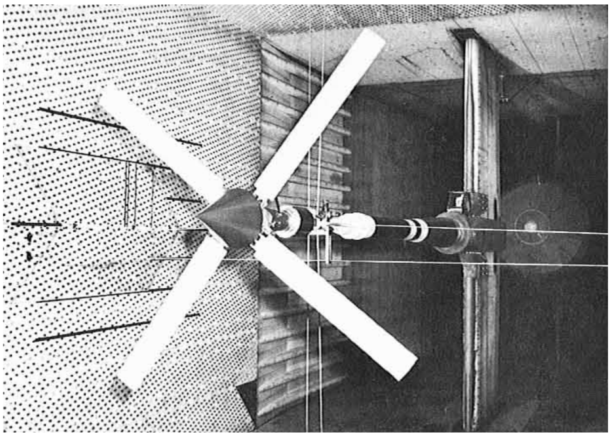

Figure 2.5: Kaman Model *KRC-6M Rotochute* under wind tunnel testing [28].

Justin Barzda [29], from the Kaman Aircraft Corporation, summarises the first developments of the *Rotochute*. As stated, along the years of studies an enormous number of configurations was studied and tested, with rotor's diameters ranging from $0.3\ m$ to $7.3\ m$, payloads from $2.7\ kg$ to $408.2\ kg$, deployment velocities up to $280\ m/s$ and rates of descent as low as $6.1\ m/s$. Barzda also discusses the operational advantages of the *Rotochute* in comparison to the recovery systems available at the time, which result in a safer, more precise and economic recovery operation [29].

The Kaman Aircraft Corporation [12] conducted an even more detailed report on the topic, with the goal of analysing the feasibility and investigating the potential capabilities of the system. It approaches several analytical works on stability, performance and control of different operation regimes: axial flight, glide flight and touchdown. It also contains the report of wind tunnel tests developed from Mach numbers of 0.5 to 3. Finally, drop tests with a remote-controlled rotor were put into practice for comprehending the complexity of the recovery and analysing the stability, control and overall performance of the rotor, as well as identifying potential problems requiring additional efforts [12].

During the recovery operation, Kaman Aircraft proposed two different initial conditions for deployment: one in hypersonic velocities (Mach numbers higher than 5), with possibility for drag and L/D ratio modulation, and other at supersonic velocities. The first one required, at the time, further research work regarding the aerodynamics and heating characteristics of such configuration. Thus, the second option was selected. Following the deployment at supersonic velocities, the vehicle should have an axial deceleration until assuming a near vertical attitude descent, phase during which the rotor achieves equilibrium conditions of autorotation, that are maintained by controlling the pitch angle of the blades [12]. The pitch control is achieved resorting to a governor that reacts to the blade centrifugal force, which varies with the rotor RPM. Consequently, the governor increases the collective pitch angle (pitch angle of all blades collectively) when the rotor RPM surpasses the design values and decreases it whenever it falls below governed velocity [29]. This would be followed by a glide phase, in which the vehicle approaches the landing site with a certain horizontal velocity. Then, the horizontal velocity is controlled with a cyclic flare (differential change of the angle around the rotor, creating a differential lift [10]) with the purpose of reducing the horizontal velocity to a near zero value. In addition, collective pitch is employed to set the blades in near stall values, with maximum generation of lift, to achieve a near zero vertical touchdown velocity, also known as collective flare [12]. The flight profile described is outlined in figure 2.6.

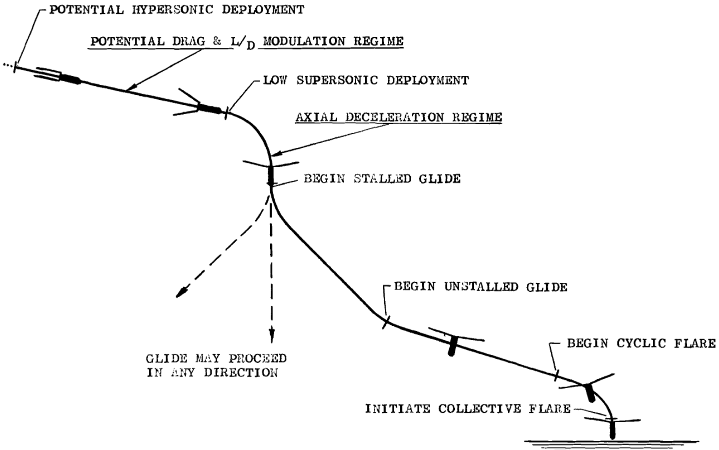
POTENTIAL HYPERSONIC DEPLOYMENT
POTENTIAL DRAG & L/D MODULATION REGIME
LOW SUPERSONIC DEPLOYMENT
AXIAL DECELERATION REGIME
BEGIN STALLED GLIDE
BEGIN UNSTALLED GLIDE
BEGIN CYCLIC FLARE
GLIDE MAY PROCEED IN ANY DIRECTION
INITIATE COLLECTIVE FLARE

Figure 2.6: Phases of operation during the recovery of Kaman's *Rotochute* [12].

Besides this, the authors provide quite interesting studies concerning certain performance parameters. For example, a graph of the rotor's drag coefficient with the axial advance ratio (ratio between the axial descent velocity and the velocity at the rotor's tip) is presented in figure 2.7 for several rotor solidity values [12]. As seen, at low advance ratios most of the blade is unstalled, operating efficiently since the rotor tip velocity is higher than the axial velocity and consequently the angle of attack on most the blade is small (this will be explained in chapter 3). In this region, solidity variations cause a bigger variation on the velocity at which the maximum drag coefficient is achieved, rather than on the drag coefficient value itself. On the contrary, the increasing advance ratio induces the whole blade to be stalled, functioning as a drag plate, with high angles of attack and a low force coefficient which will become relatively constant with the increasing descent velocity. In this situation rotor solidity is nearly proportional to the rotor drag coefficient [29]. This means that compromise must be made in the choice of the blade solidity, considering that typically a higher solidity means higher weight penalties [12].

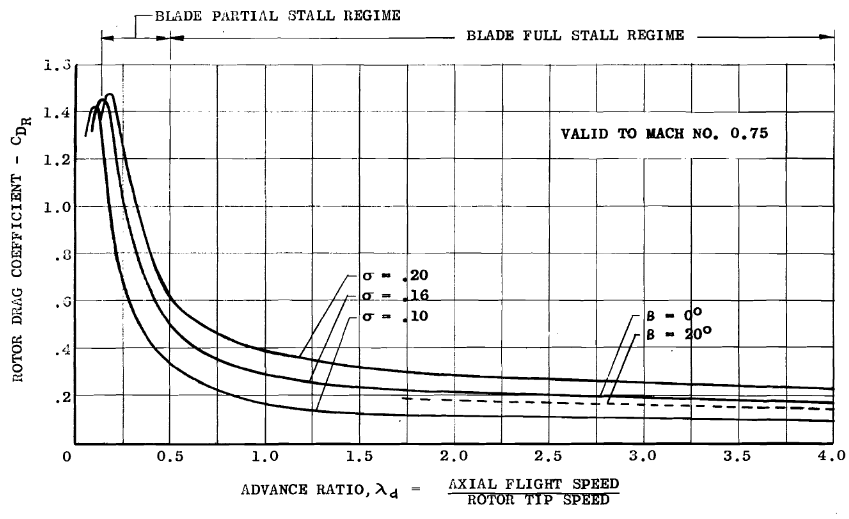

Figure 2.7: Rotor's drag coefficient variation with axial advance ratio and solidity [12].

Finally, the rotor's mass variation was also studied, since it influences the system's design. As observed in figure 2.8, the percentage of the rotor's mass increases with increasing rotor solidity and with decreasing disk loading and is, in this example, located between 6% and 16%, approximately [12]. Barzda takes similar conclusions, stating that 10% of the gross weight for the rotor's mass would be a realistic and feasible value [29].

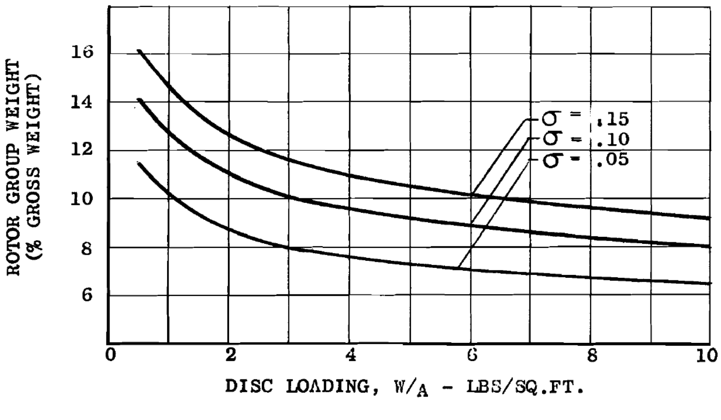

Figure 2.8: Variation of the rotor's mass percentage with disk loading and rotor solidity [12].

The theoretical works revealed that the rotor was liable to be deployed and operated at supersonic velocities during re-entry, with terminal velocities around $15.2\ m/s$ [29] and touchdown velocities of less than $1.6\ m/s$, resorting to flare manoeuvres [12].

On the other hand, the wind tunnel experiments held on the *KRC-6M* model (figure 2.5) revealed excellent correlation with the theoretical analysis, as well as the successful deployment and operation of the rotor up to Mach number 3, in axial flight [12].

Finally, the air drop tests at subsonic velocities for the remotely controlled *KRC-6 Rotochute* (figure 2.9) confirmed the initial potential of the recovery system. The rotor was deployed and gliding, manoeuvring and flare were successfully demonstrated, with the transition between the axial and gliding phase being achieved stably and smoothly. The desired descent rates were achieved, as well as values close to 2.5 of L/D ratio in the glide regime. Some important data were acquired regarding vehicle stability, which was discussed to need some improvements, especially on lateral stability during the cyclic pitch flare manoeuvre. Spiral instability, originated due to operation of the rotor above the stable range of RPM, was also an important parameter studied, and was controlled by an automatic stabilisation system. In the end, it was concluded that both flare manoeuvres required more studying and testing [12].

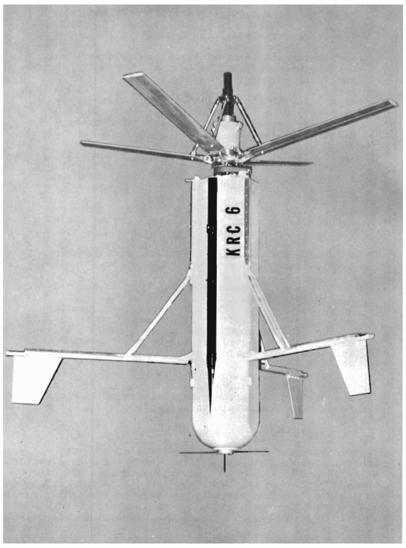

Figure 2.9: KRC-6 *Rotochute* Test Vehicle [12].

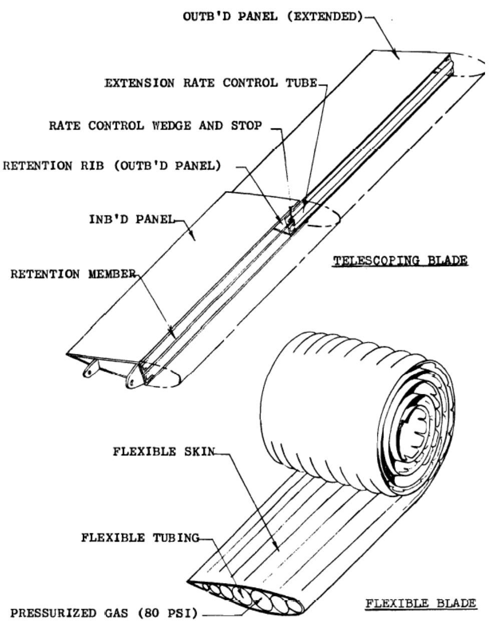
OUTB'D PANEL (EXTENDED)
EXTENSION RATE CONTROL TUBE
RATE CONTROL WEDGE AND STOP
RETENTION RIB (OUTB'D PANEL)
INB'D PANEL
RETENTION MEMBER
TELESCOPING BLADE
FLEXIBLE SKIN
FLEXIBLE TUBING
PRESSURIZED GAS (80 PSI)
FLEXIBLE BLADE

Figure 2.10: Telescopic (top) and flexible inflatable (down) blade concepts [12].

Blades' stowage is also a factor that requires attention when designing the system, since it imposes limits to the blade's span and, potentially, to the performance of the rotor for a designated mission. Consequently, researchers at Kaman [12] proposed diverse types of blades including fixed, telescopic and flexible inflatable blades. The two latter types would be preferential to fixed blades whenever stowage would be prioritised over deployment, allowing for packaging into a small volume of space. A telescopic blade, at the top of figure 2.10, is a type of blade in which only one section is fixed, while the others have the capability to be stowed inside the fixed piece and extend themselves when the rotor is deployed. On its side, the inflatable blade, on the lower side of figure 2.10, was expected to present nearly the same torsional stiffness of a typical airfoil, being able to be folded when not inflated for saving space [12].

To conclude, this was a valuable program that confirmed the theorised potential of stored energy rotors for recovery, predicted previously by Bensen [26].

2.3.3 NASA's Wind Tunnel Testing

Likewise, NASA saw this technology as a promising addition to their space program, during the space race era. Charles Libbey and NASA's Recovery Systems Branch [30] conducted tests in the Langley Research Centre regarding its dynamic stability.

Experiments on an Apollo-type capsule in a vertical autorotative descent showed that numerous factors are likely to affect the system's dynamic stability: disk loading, hub inertia (the connector between the blades and the main shaft), blade hinge angle (resultant from flapping, an up and down motion of the blade relatively to the plane normal to the hub axis, that compensates for asymmetry of lift [10]), distance between the blade hinge axis (axis that allows the blade to flap [10]) and the axis of rotation, and vertical location of the centre of gravity. Other parameters that affect stability are the solidity ratio, number of blades, blades' weight, blade incidence angle and payload configuration. By varying some parameters, the experiment assessed the changes on the vehicle's stability.

In figure 2.11, three different configurations are presented, in which the hub inertia was sequentially changed, improving the stability of the model: unstable (left), marginally stable (centre) and stable (right). This methodology allowed for the creation of graphs that assisted on understanding how the alteration of the parameters would affect the stability of the system. Libbey concluded by stating that rotary recovery systems can be made inherently stable [30].

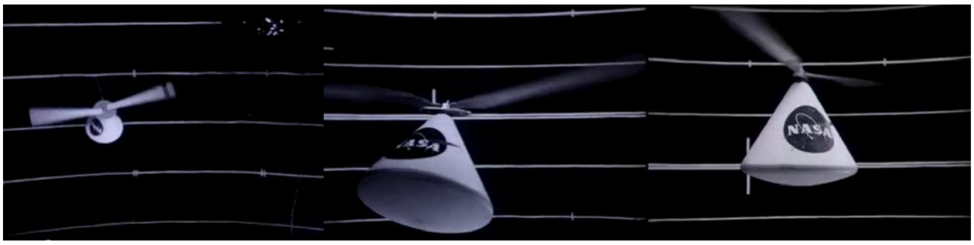

Figure 2.11: Unstable (left), marginally stable (centre) and stable (right) configurations, in which the difference between the corresponding models is the hub inertia [31].

2.3.4 Space Rotor

In 1965, M. Kretz [15, 32] filed a patent for the Space Rotor, a rotor system intended to ensure the re-entry of space vehicles and their further recovery and landing on unprepared landing sites, without the use of any source of power. The rotor would thus be deployed before re-entry and the vehicle would glide almost horizontally during hypersonic flight [32]. It would then autorotate during the subsonic regime.

The Space Rotor was designed to be light, manoeuvrable and fully reusable, having a high capacity to assist on the soft landing of several of space vehicles. In fact, it was expected to perform a final flare manoeuvre for touchdown which would reduce the approach velocity from $20.6\ m/s$ to $1.8\ m/s$, approximately. The main applications of this system would be for the recovery of boosters and manned/unmanned hypersonic gyrogliders, concepts that are observable in figure 2.12. In addition, the Space Rotor represented a constant weight penalty of 11% to 14% of the total landed weight. This was a considerably lower penalty when compared to the conventional means of re-entry and recovery [15].

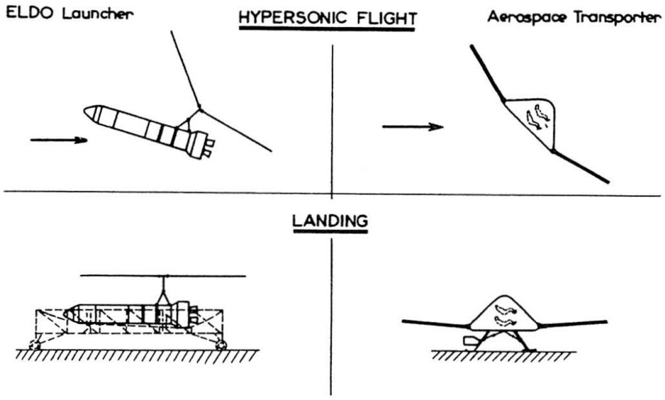

Figure 2.12: Configurations of hypersonic gliders (Space Rotor) proposed [32].

Kretz claimed that the major difficulty of the existent methods at the time was that the stages of re-entry and landing asked for distinct device's characteristics. During landing, large areas are necessary to reduce the velocity, which are irrelevant for re-entry. In addition, the heating felt by the system during re-entry could have disadvantages on the landing. The Space Rotor tried to give an answer to these problems: by varying the angle of the blades in relation to the vehicle, changing the lift and drag forces, trajectory control would be possible during re-entry. Furthermore, it would avoid excessive heating of the blades since it would cause an even distribution of the heat generated at the stagnation point around the blades. Kretz presented several options, types of construction and variations of the Space Rotor [32].

2.3.5 NASA Ames Research Center's Program

Motivated by the *Rotochute*'s studies, NASA's Ames Research Center launched a programme in 1963 for evaluating the utility of this recovery method at high subsonic and supersonic velocities [13].

Ronald Smith and Alan Levin [33] led the program, starting with an analytical analysis of parameters such as range, deceleration and heating for a capsule's re-entry (only Kretz had considered deployment during re-entry [15, 32]). The analysis was based on the Blade Element Theory (BET) and combined both the aerodynamic characteristics of the rotor alone and the rotor plus capsule assembly, also accounting for high blade's pitch angles. Resorting to Newtonian flow concepts, the local forces on the blades were obtained and, with some theoretical calculations, the rotor torque, blade centrifugal moment and aerodynamic moment were obtained. By assuming equilibrium conditions, which require the two latter referred moments to equal each other and the torque to equal $0\ N \cdot m$, it becomes possible to compute the rotor axial, side and normal force coefficients, as well as the rolling and pitching moment of the rotor in relation to the hub [33]. The work was claimed to be a success, with the theoretical and experimental values of the rotor drag in axial flight agreeing for all Mach numbers, except in the transonic regime [33].

An interesting study carried out herein plots the dimensionless tip velocity (ratio between the blade's tip velocity and the free-stream velocity) as a function of the blade pitch angle, for rotor angles of attack of $20°$ and $90°$ (the latter representing an axial flight). The plot is present in figure 2.13. For a low velocity operation (left) in axial flight, between blade pitch angles of $-6°$ (leading edge of the blade facing down) and $9°$, the axial dimensionless tip velocity is multi-valued - there is an unstable operation in this blade pitch angle range. It is also clear that there is a distinction between the stalled and unstalled blade operations, as predicted by Kaman [12, 29]. For supersonic velocities (right) it is shown that, in axial flight (in comparison to angle of attack of $20°$), there are higher rotor velocities and the curve is more sensitive to pitch angle variations - this means that very accurate pitch control is required to avoid the overspeed of the blades. In addition, a value of rotor velocity corresponds to one and only one pitch angle value and consequently these rotor velocities are stable for the whole pitch angle range [33].

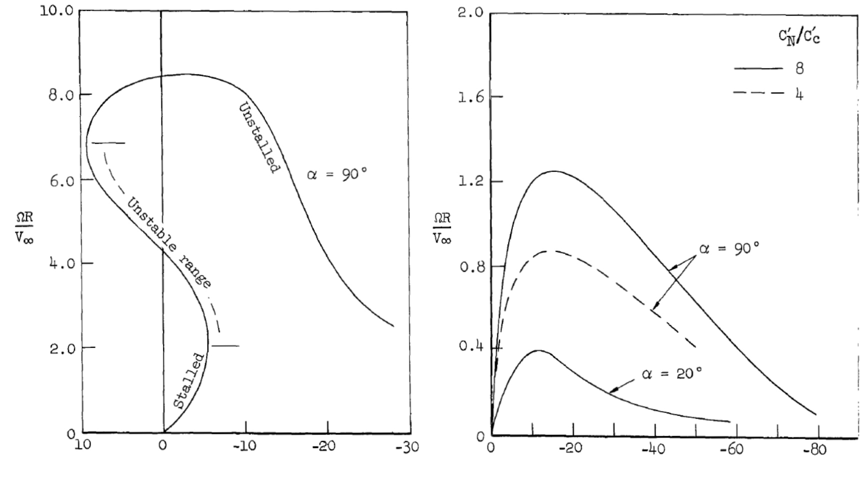

Figure 2.13: Autorotation dimensionless tip velocity ratio with blade pitch angle, for a typical low velocity operation (left) and predicted by theory using Newtonian flow for supersonic velocities (right) [33].

Moreover, Smith and Levin [33] studied the heating of the system, concluding that adding the rotor alleviates the effects of heating. Nevertheless, the maximum rotor blade heating rate was surpassed for a rotor to capsule diameter ratio of 2, forcing the study of higher rotor diameters. Rotor to capsule diameter ratios up to 4 presented major advantages regarding lateral and longitudinal stability, maximum deceleration and heating. Above the diameter ratio of 4, small further gains in the referred factors and the weight and stowage penalties both suggest that the diameter ratio of 4 would be an optimum value.

Despite this, for a glide entry the maximum heating rate and temperature of the blades would still be exceeded. Thus, a study regarding the effects of a delayed deployment was conducted, concluding that the maximum Mach number for the transition between axial and glide flights was 17, even though possible above the Mach number of 8 with heating protections associated. This would bring considerable losses in lateral range, though. Nonetheless, the study confidently claimed that the adding of the rotor would improve the entry performance and operational flexibility [33].

The study led to the outlining of a sequence for the entry vehicle. As observed in figure 2.14, the rotor would be deployed in near axial flight, with a coning angle of the blades of $45°$ to avoid capsule bow shock impingement. As stated, the transition to glide would begin around a Mach number of 17, evolving eventually to a subsonic glide flight with a L/D ratio of 4 [33].

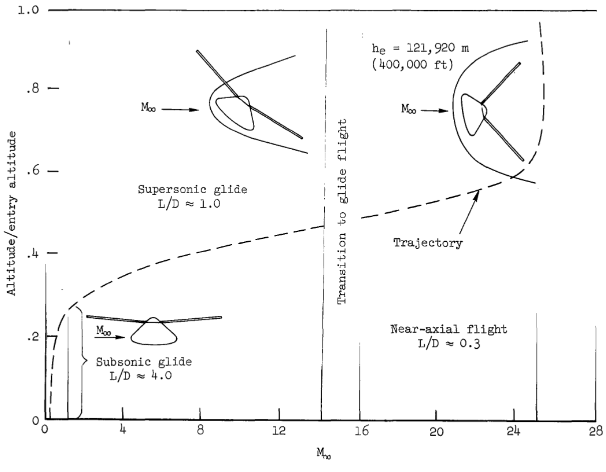

Figure 2.14: Rotor vehicle operating modes proposed by Smith and Levin [33].

The investigation proceeded with several wind tunnel tests for what was named “the unpowered rotor entry vehicle”, with the aim of obtaining experimental data on the aerodynamic characteristics of the system. The tests were conducted for subsonic (Mach numbers of 0.1 to 0.7) [34], transonic (0.91 to 1.11) [35] and supersonic (1.62 to 3.54) [36] velocities, for model angles of attack between $15°$ and $90°$, the latter corresponding to axial flight. These experiments are summarised in a conference paper [37].

The analysed rotor had four blades and two configurations were tested, one with a rotor solidity of 0.2 and a rotor to capsule diameter ratio of 3 and other with a solidity of 0.15 and a diameter ratio of 4 [37], which was the optimum value calculated in the preceding study [33]. The investigation was carried out by remotely varying the blade pitch angle at a constant Mach number and model’s angle of attack. Note that the cyclic and collective pitch were not changed at the same time, being studied separately.

The authors concluded that, accordingly to their predictions [33], the rotor plus capsule assembly had a considerably higher drag coefficient than the capsule alone, which can be up to 5 times higher for axial flight, as seen in figure 2.15 [37]. Apart from this, in the gliding phase and at Mach numbers below 0.7, the rotor provides substantial gains in the maximum L/D ratio which reflects itself in a higher lateral and longitudinal range. At higher Mach numbers, this contribute is slighter [37]. This was predicted on the analytical studies as well [33].

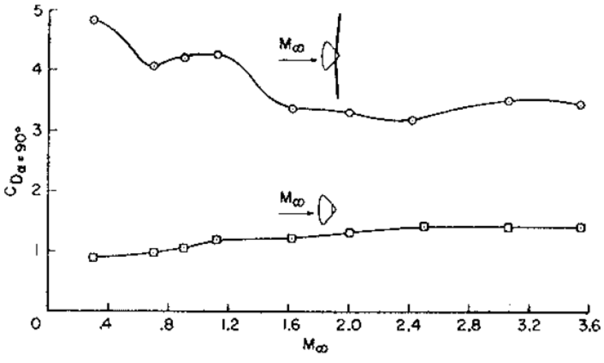

Figure 2.15: Variation of the capsule's drag coefficient with and without the rotor, with Mach number [37].

Moreover, like in the theoretical studies, the stability of the rotor in autorotative equilibrium as a function of the pitch angle and Mach number was studied, since at low forward velocities the system can become unstable. The instability was observed for Mach numbers equal or lower than 0.2, since for a single blade pitch angle there were several correspondent rotor tip velocities. However, for Mach numbers equal or higher than 0.3 it became stable at all pitch angles and model's angles of attack [37].

Regarding the equilibrium rotor drag coefficient, an interesting finding indicated that it is directly proportional to the rotor solidity, validating the observations of Ham [28] and Kaman [12, 29].

With respect to the measured moments, it was also seen that, at supersonic velocities, the addition of flaps to the capsule combined with cyclic pitch control would trim the vehicle and reduce the high pitching moments generated, with almost no reflection on the L/D ratio [37].

Furthermore, the researchers discussed the uncertainty associated with the estimation of the rotor's weight, because it is dependent on many design and conceptual factors. Eventually, they went into an agreement with the previous referred studies for a plausible value of the rotor's weight between 10 and 15% of the whole system, with the potential to be reduced even further [13, 37].

In a final note, the authors adjudge that the results gathered for the operating characteristics of a rotor entry vehicle appear to make the system suitable for the recovery of space vehicles [37].

While performing the research work for this document, the author could not help but notice the amount of confidence that all the referenced testimonies shared in this recovery method and how advantageous it appeared to be in comparison to the conventional options. However, it was intriguing to see that none of the studies ever had full-scale tests and that many research works were discontinued without an apparent justification. The same concern was revealed by Hagen [2] who, following private conversations with C. Libbey [30], revealed that in that period the studies were more focused on finding a direct alternative to parachutes rather than a fully controllable flight - active control systems were discouraged, since they would lead to a higher degree of complexity that was not time affordable [2].

2.3.6 Rotary Rocket's *Roton*

After a long period without advances and with the space industry shifting towards commercialisation, a company named Rotary Rocket was established in 1996 with the goal of providing safe, reliable, flexible and low-cost access to space, ultimately delivering communications and other commercial satellites to Low Earth Orbit (LEO). The company presented the *Roton* - a fully reusable, Single-Stage-To-Orbit (SSTO) vehicle - to achieve the stated objective. Gary Hudson [4] and Sarigul-Klijn et al. [38] presented and provided details on this innovative space vehicle, its mission overview and development program, mentioning a future flight test program.

The *Roton* had a conical shape with a reference cargo capacity of $3175\ kg$ [38]. Controlled by a crew of two pilots, it would take-off like a conventional rocket and deliver its cargo in orbit. Prior to re-entry, the recovery system, composed by a rotor with four blades folded down alongside the vehicle, would be deployed. During the hypersonic and supersonic flight, the spacecraft's base would be responsible for the majority of the drag, while the rotor would be stalled, though contributing for the vehicle's stabilisation [4]. At subsonic velocities and around $8.5\ km$ of altitude, it would enter the autorotation phase and the vehicle would be capable of gliding, permitting a controlled approach to the landing site [38]. Then, blade tip thrusters installed on the blades would induce a powered landing and consequently a soft touchdown [38] - something that had already been discussed by Kaman, referring that it could even reduce the required rotor size [12]. The *Roton* would then go through maintenance in order to be ready for a new flight in the range of one to two days. Moreover, the *Roton* would possess the distinctive capability of intact abortion of the mission, being able either to complete the flight or to return to the ground intact [4].

As part of the flight test program, Rotary Rocket built a full-sized vehicle which intended to test autorotation, approach and landing with a flight altitude of $2.4\ km$ [38]. Citing Diaz-Silva et al. [31], the vehicle had a rotor radius of $8.5\ m$ and was successfully tested three times, despite the high control difficulty. Then, a simulator that predicted its static and dynamic stability characteristics was built to gather more data. More than seventy five experienced test pilots flew the simulator and all declared that the vehicle was so difficult to fly that control would be eventually lost during its operation - stability demanded improvements [31]. According to Hagen [2], factors such as the *Roton* being a SSTO vehicle and the rotor being operated in the hypersonic regime were extremely ambitious, representing clear technological obstacles. Eventually, the Rotary Rocket Company closed its doors.

2.3.7 Recent Concepts

In the early two thousand's, NASA Ames resumed the studying of this method, applying it to planetary exploration. Young et al. [39] investigated the system's operation on Mars, something challenging due to a low-density atmosphere in which the vehicle would operate under low Reynolds numbers and compressible flow. By testing the rotor (seen in figure 2.16) in Mars' conditions, the researchers were able to replicate the planet's environment and analyse parameters of the rotor such as thrust and power. Despite requiring optimisation on the aerodynamical and structural parts, this preliminary test suggested that the rotor was competent to achieve the goals required for the mission [39].

On the other side, a concept for decelerating a Venus exploration probe was also proposed, since Venus' high density favours the use of the technology and the mission itself would require active landing control. However, control and hazard avoidance systems still demanded further development [40].

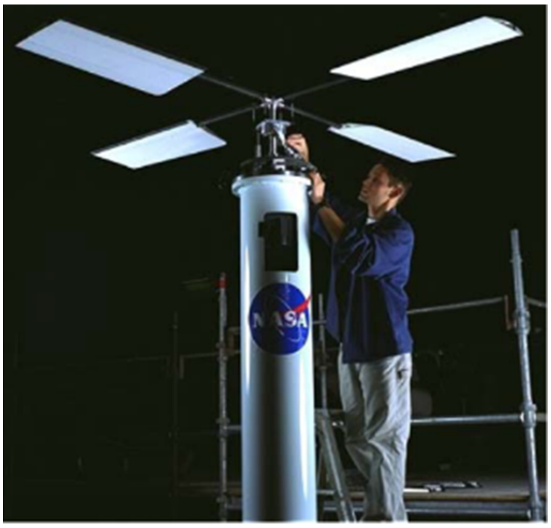

Figure 2.16: Proof of concept for the Mars rotor developed by NASA Ames [39].

In 2005, Jeffrey Hagen [2] discussed the use of a rotor system during the final descent and landing of a Crew Exploration Vehicle (CEV), in this case an Apollo type capsule. Contradicting some of the works cited on this document, Hagen stated that the rotor should not be exposed during re-entry, since this would require a high level of development and new technology. The author defended that, since the rotor system would be replacing the parachute, it should only be deployed in the same conditions of the latter - at subsonic velocities and stratospheric altitude [2].

During re-entry, the telescopic blades would be positioned along the side of the capsule. At subsonic velocities, deployment would be regulated resorting to braking cables, which would avoid the overloading of the blades (figure 2.17(a)). Hereafter, the centrifugal force resulting from increasing rotation velocities would cause the telescopic blades to fully unfold (figure 2.17(b)). Apart from this, blade tip thrusters would extend the hover time and provide additional landing safety and control, and the capsule would be equipped with a parachute for emergencies. The rotor would have a diameter of $12.9\ m$ and represent around 13% of the gross weight, in order to decelerate the $4.42\ m$ diameter capsule [2].

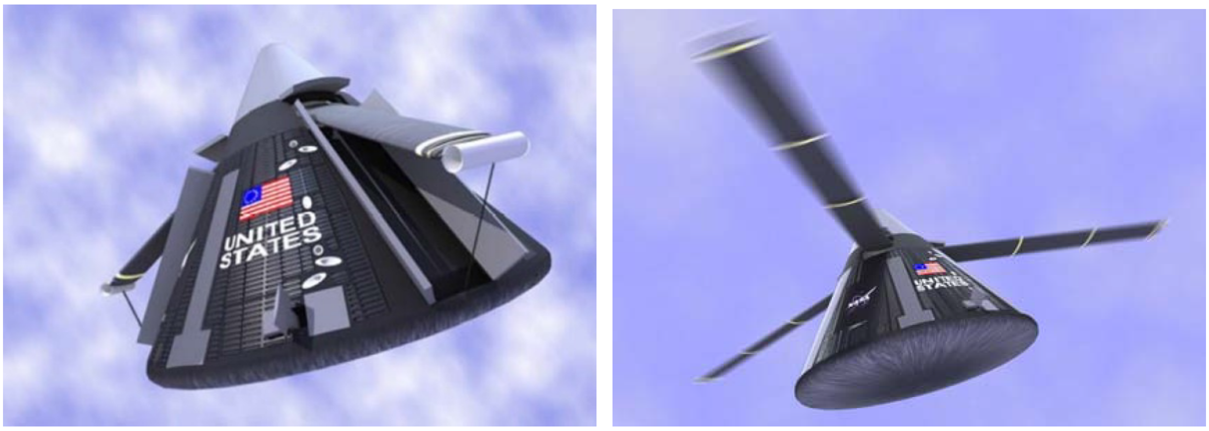

(a) Rotor under deployment.

(b) Capsule in an autorotation descent.

Figure 2.17: Capsule with rotor proposed by Hagen [2].

Nonetheless, Hagen noted that many developments were still necessary for this method, yet promising, to be reliable, for instance: the initial rotor spin up and unfolding of the blades due to vehicle stability; the extension of the telescopic blades under load; avoiding the vehicle torque resultant from the rotor's rotation; application of the tip thrusters; active guidance to an undecided landing location and flight path control; improvements on the landing flare manoeuvre, especially regarding its timing [2].

Eventually, a small radio-controlled model capsule with the rotor mounted was tested by a NASA's team, including Hagen, in 2012, with a drop test at approximately $146\ m$. The collective pitch angle of the rotor was successfully controlled and deceleration and a safe landing were verified [41].

In 2007, a rotative wing system named the *Autobody* was designed, analysed and tested by researchers of the University of Maryland [42]. The *Autobody* was an autonomous autorotative system with the objective of safely delivering a payload dropped from an aircraft. It had a total mass of $2.27\ kg$, a four bladed rotor with a diameter of $1.22\ m$, and an objective steady state descent velocity of $4.57\ m/s$, in axial flight. The system was not equipped with active control systems, meaning that the rotor would transit passively to a steady autorotation regime. For this transition to occur and to minimise of the rate of descent, the pitch angle of the blades would have to be passively increased with the increase of the rotor angular velocity, what would be accomplished through the application of a negative blade hinge angle [42].

The work covered theoretical calculations, to predict the autorotative behaviour, and its validation with wind tunnel and drop tests in full-scale prototypes. The wind tunnel tests showed good correlation with the theory. Finally, the drop tests were of great success, since the terminal velocity of the system and rotor RPM revealed concordance with the theory, with the maximum error being of 22.2%. Eventually, the system even managed to achieve a terminal velocity of $4.11\ m/s$, which was lower than the target [42].

Starting in 2008, the European Space Agency (ESA), GMV, the University of Bologna and the European Aeronautic Defence and Space Company Astrium (EADS Astrium) [43–46] explored the feasibility of the AutoRotation in Martian Descent And Landing (ARMADA) project, consisting of an Entry, Descent and Landing System (EDLS) for Mars' exploration. Citing Peters et al. [44], ARMADA consisted on a rotor mounted on a Viking-like aeroshell and its goal was to safely decelerate and land a payload with a mass between $2\ kg$ and $200\ kg$ in Mars with a landing velocity between $10\ m/s$ and $20\ m/s$ and a close proximity to the predefined landing site. At re-entry, in the supersonic regime, an aeroshell would be deployed and the rotor partially deployed. Then, the aeroshell would be ejected, followed by the start of the spinning of the blades due to the change in pitch angle, causing its autorotative operation. Once in the subsonic regime, the telescopic blades would be fully deployed due to centrifugal forces, decelerating the capsule with the autorotative rotor. The sequence would come to an end with a flare manoeuvre for touchdown [45].

Cadenas et al. [43] discussed several rotor (single rotor at the top, single rotor at the bottom, dual rotor side by side, co-axial dual rotor, multiple rotor) and blade (telescopic, inflatable, foldable, flexible) designs. As for the rotor, the authors agreed that the simplicity, reliability, light weight and extensive knowledge behind the single rotor at the top configuration made it evidently the safest option. Regarding the blades, the telescopic were the selected ones.

Peters et al. [44] and Modenini et al. [45] made an overview of the ARMADA project, presenting a model's wind tunnel testing and a software program that evaluated the autorotation's performance. The rotor's partial and full deployment in the supersonic, transonic and subsonic regimes, and the behaviour of drag, lift and rotor angular velocity were analysed in a wind tunnel. Such tests proved the feasibility of the system, with the partial deployment at transonic velocities and the full deployment at subsonic velocities [45]. The rotor appeared to have a normal behaviour up to a Mach number of 2, with the drag coefficient being similar to the one of a parachute [45]. Under subsonic velocities, the results corroborated the ones obtained by Smith and Levin [34] on their experimental studies.

The differences between stalled and unstalled blade's operation was also a matter of study, concluding that the rotor drag coefficient varies substantially between these regimes, even though the rotor can operate in both. Nonetheless, it was stated that the unstalled mode is more efficient and thus the rotor should operate in it [45, 46]. Moreover, it was referred that in the subsonic regime, for negative blade pitch angles, lower absolute values lead to a stalled rotor. However, if an unstalled flow is established, the lowest absolute collective pitch angle corresponds to the highest axial dimensionless tip velocity and the most efficient operation [44].

Around the same time, EADS Astrium [3] was also exploring the feasibility of the system for an effective controlled descent and landing of a probe in Mars, as an alternative to the powered soft-landing and parachute landing. For this mission, the rotor would be deployed at a Mach number of 2 and an altitude of $10\ km$, with a targeted landing velocity between 10 and $20\ m/s$. In this study some considerations were presented, one of which related to the effects of wind, which was observed to decrease the landing velocity in some cases. On top of that, and considering its easy stowage and low mass, an inflatable rotor was tested in a wind tunnel, with its deployment being successful [3].

Finally, Steiner and Young [14] discussed its application on atmospheric research probes on Titan, the biggest moon of Saturn. The authors claimed that the system would be able to generate power for its sensors and research components by attaching a generator to the free-spinning rotor, and that controlling the rate of descent would be an asset for atmospheric research, an application previously stated in chapter 1.

Academically, students from the University of Würzburg [47–49] worked in project Daedalus, with the goal of testing rotative wings in atmospheric research probes, or *SpaceSeeds*. A simplified first iteration without pitch control was recovered following a descent from $80\ km$, showing some stability problems and a terminal velocity of $25\ m/s$, but satisfying parameter correlation with the predictions [47]. A second iteration, already with pitch control, was developed and tested in wind tunnel, showing good performance and control robustness [48, 49]. This design will undergo flight tests in early 2023 [49].

2.4 Comparison of Recovery Methods

Taking into account the literature review held not only on the rotative wings recovery system, but also on the remaining methods discussed in section 2.2, a qualitative comparison between them should be made. This comparison, seen in table 2.1, considers the most important characteristics that a recovery system should have, and is based on comparisons made by some of the referred authors [2, 3, 14]. The parachute recovery is used as a reference, with all its characteristics having a value of 0. The plus and minus symbols translate into better or worse than the baseline, respectively, for a specific characteristic or capability [14].

Table 2.1: Comparison between the main existent recovery methods and rotative wings.

Characteristic	Methods				
	Parachute	None	Controlled Vertical Landing	Spaceplanes	Rotative Wings
Cost	0	+	-	-	-
Weight	0	+	-	-	-
Manoeuvrability	0	0	+	+	+
Controlled gliding	0	0	0	+	+
Smooth/safe landing	0	-	+	+	+
Mission Flexibility	0	-	0	0	+
Landing accuracy	0	-	+	+	+
Reusability	0	-	+	+	+
Range of applications	0	-	-	-	+
Successfully studied/tested	0	-	+	+	-
Total	0	-4	$+2$	$+3$	$+4$

As observed in the table, rotative wings appear to be more advantageous than the other methods. While rotative wings, controlled vertical landing and spaceplanes share many capabilities such as manoeuvrability, ability to perform a low velocity and accurate landing and reusability, rotative wings present distinctive characteristics that make it stand out: the flexibility of the mission regarding variations or eventual emergency abort situations, and the range of applications in which it can be utilised.

Regarding the cost and weight, the three main techniques are disadvantageous when compared to the parachute, since an increase in capability is associated with higher costs and system's weight. Furthermore, if one compares quantitatively such technologies as for its cost and weight, there is a good possibility that the rotative wings method can be beneficial in comparison to the controlled vertical landing and spaceplanes, taking into account the low weight penalties predicted by the literature. However, such assumption would have to be further studied.

Chapter 3

Methods

In this chapter, the methods utilised in order to perform the proposed work will be carefully described.

In section 3.1 the autorotation phenomenon and the aerodynamic theory associated with it will be explained, resorting to analytical theories. Such theory was the base to a computational model that simulates the recovery of a rocket's first stage using rotative wings. Thus, the model will be extensively explained in section 3.2, including the general functioning of the algorithm, problems found and their solutions, and assumptions made. It will also address the model's verification, by analysing an example and comparing it to the literature studies. Furthermore, a mesh study will be conducted.

Finally, a general description of a genetic algorithm is present in section 3.3, since an optimisation will be conducted further on this work to obtain an optimum design of the recovery system.

3.1 Autorotation Aerodynamic Analysis in Axial Flight

As stated in chapter 1, autorotation is a self-sustained phenomenon used to safely recover helicopters in the event of a failure that does not permit it to fly in its normal operation, more frequently an engine failure. It is, then, an emergency state in which the vehicle's rotor remains on rotating and provides thrust, allowing the pilot to reduce the descent's velocity until a safe touchdown velocity.

This phenomenon can be put into simple terms by the conservation of energy. During the descent, the vehicle gives up potential energy (altitude) and the relative vertical descent velocity causes an upward airflow in the plane of the rotor, consequently providing it with kinetic energy [9]. Eventually, steady state conditions are achieved, meaning that the thrust induced by the rotor equals the weight of the vehicle, the rotor torque becomes equal to $0\ N \cdot m$ and the vehicle reaches a terminal velocity [11].

The aerodynamics of this phenomenon will then be carefully explained, assuming a fully vertical descent (axial flight), which represents the simplest case. For this analysis, the Blade Element Theory (BET) will be used. The BET treats each infinitesimal blade section as a 2-D airfoil that produces sectional aerodynamic forces and moments [9]. Thus, by performing an integration of such sectional forces (or moments) across the length of the blade and averaging the result for a rotor revolution, one can obtain the resulting forces (or moments), allowing for the performance analysis of the rotor to be conducted. The BET is demonstrated by Professor G. Leishman [9], and this section is based on such analysis.

Figure 3.1 is a scheme of the airflow, aerodynamic forces and angles in an infinitesimal blade section (a 2-D airfoil) of the rotor, in axial flight. The coordinate system is centred on the centre of rotation of the blade (near its root), which means that the positive x-axis is directed to the tip of the blade.

Since the vehicle is in a fully vertical descent, the resultant velocity relative to the rotor blades, at any blade section and at a radial distance x from the axis, can be separated into two components: a vertical component $\vec{U}_P$ and a horizontal component $\vec{U}_T$ [9]. The vertical component is given by

$$\vec{U}_P = (V_c - v_i)\vec{e}_y = U_P\vec{e}_y \tag{3.1}$$

where $\vec{V}_c$ is the velocity vector of the airflow relative to the vehicle, which is caused by the air being forced up through the rotor (positive on the y-axis), thus equivalent to its descent velocity, and $\vec{v}_i$ is the axial induced velocity (negative on the y-axis), which will be explained later on, both in m/s. These velocities are assumed to be uniform along the blade.

On the other hand, the horizontal component (parallel to the rotor and negative on the z-axis) at a particular blade section results from the blades rotative motion and is equal to

$$\vec{U}_T = \vec{\omega} \times \vec{x} = -\omega x\vec{e}_z = -U_T\vec{e}_z \tag{3.2}$$

according to [9], in which $\vec{\omega}$ is the angular velocity vector of the rotor in rad/s and $\vec{x}$ is the x-coordinate vector of the section in m, with $0 \leq |\vec{x}| \leq R$, in which R is the radius of the blade, as observed in figure 3.2. The blade root cut out, r_0, represented in figure 3.2, which is the distance between the rotational axis of the rotor and the blade's root, will not be considered in this work.

Understandably, the resultant velocity at one blade element is the sum of the two velocity vectors:

$$\vec{U} = U_P\vec{e}_y - U_T\vec{e}_z \tag{3.3}$$

and its magnitude is

$$\|\vec{U}\| = \sqrt{\|\vec{U}_P\|^2 + \|\vec{U}_T\|^2} \tag{3.4}$$

The angle between $\vec{U}$ and the reference plane of the rotor is called induced angle of attack (or relative inflow angle) and is given in degrees, from [9], by

$$\phi = \tan^{-1}\left(\frac{\|\vec{U}_P\|}{\|\vec{U}_T\|}\right) \tag{3.5}$$

In addition, two other angles are of extreme importance. The pitch angle of the blades, θ, is the angle at which the rotor blades are set with respect to the plane of rotation, and for this study will be assumed to be constant and equal through the blade (collective pitch). In figure 3.1, this angle is represented as being positive (airfoil leading edge pointing up) but, in an autorotative descent, it should have a negative value for the airfoil to generate the required forces, as will be explain further on this document. Finally, the angle of attack of the airfoil, which is the angle between $\vec{U}$ and the chord line of the airfoil, is

$$\alpha = \phi + \theta \tag{3.6}$$

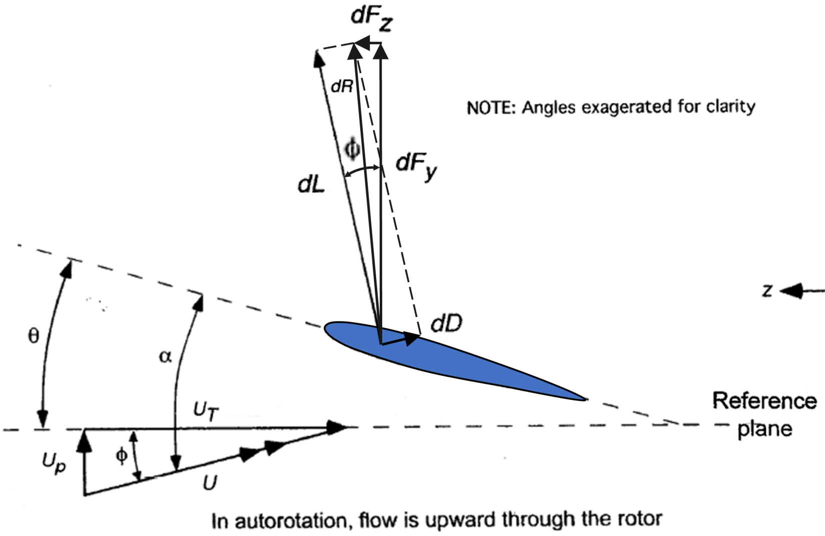
dF_z
dR
NOTE: Angles exagerated for clarity
y
ϕ
dF_y
dL
z
x
θ
α
dD
U_T
Reference plane
U_p
ϕ
U
In autorotation, flow is upward through the rotor

Figure 3.1: Side view of a blade element in autorotation, in axial flight, according to the BET. Adapted from [9].

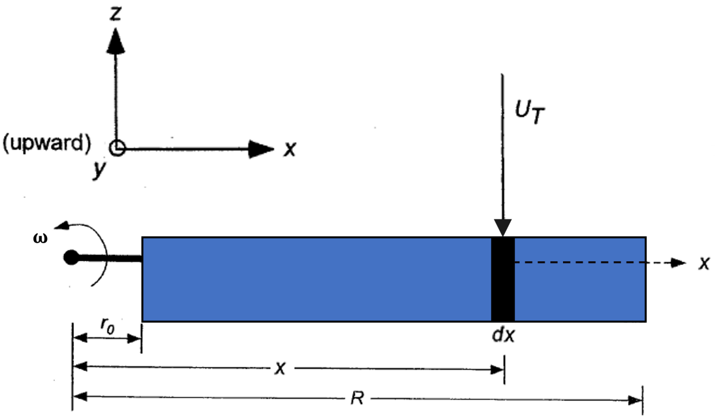
z
(upward)
y
x
U_T
ω
x
r_0
dx
x
R

Figure 3.2: Top view of the blade in autorotation, in axial flight. Adapted from [9].

From simple flight aerodynamics, one knows that the resultant wind velocity on the airfoil will create lift, L, which is normal to the airflow direction, and drag, D, which is parallel. Therefore, for each blade element, such aerodynamic forces are, in N,

$$\|d\vec{L}\| = \frac{1}{2}\rho\|\vec{U}\|^2 cC_l dx = \frac{1}{2}\rho\|\vec{U}\|^2 C_l dA \tag{3.7}$$

$$\|d\vec{D}\| = \frac{1}{2}\rho\|\vec{U}\|^2 cC_d dx = \frac{1}{2}\rho\|\vec{U}\|^2 C_d dA \tag{3.8}$$

where C_l and C_d are the lift and drag coefficients, respectively, ρ is the density of the air in kg/m^3, dx is the length of each blade element, in m, and c is the local blade chord of the blade, also in m [9]. In this work, for simplicity, the blades are assumed to have a rectangular shape. Such consideration means that c is constant through the blade's span and the infinitesimal area of a section is given by $dA = dx \cdot c$.

As seen in figure 3.1, the sum of $d\vec{L}$ and $d\vec{D}$ is a resultant force vector $d\vec{F}_{res}$ that can be decomposed into its vertical and horizontal components. The vertical component, perpendicular to the rotor disk plane, is the infinitesimal force $d\vec{F}_y$, which will provide an upwards force, allowing for a deceleration of the vehicle's descendant motion. On the other hand, the horizontal component $d\vec{F}_z$, parallel to the rotor disk plane, will provide the blades with rotary motion. Considering the trigonometric relations between $d\vec{L}$, $d\vec{D}$ and ϕ, observable in figure 3.1 [9], one gets:

$$d\vec{F}_y = \Big(\|d\vec{L}\| \cos\phi + \|d\vec{D}\| \sin\phi\Big)\vec{e}_y = dF_y\vec{e}_y \tag{3.9}$$

$$d\vec{F}_z = \Big(\|d\vec{L}\| \sin\phi - \|d\vec{D}\| \cos\phi\Big)\vec{e}_z = dF_z\vec{e}_z \tag{3.10}$$

Moreover, the contributions of such forces for the rotor's infinitesimal thrust, $d\vec{T}$, in N, and torque, $d\vec{Q}$, in $N \cdot m$, according to [9], are

$$d\vec{T} = N_b dF_y \vec{e}_y = dT\vec{e}_y \tag{3.11}$$

$$d\vec{Q} = N_b(d\vec{F}_z \times \vec{x}) = N_b dF_z x\vec{e}_y = dQ\vec{e}_y \tag{3.12}$$

where N_b is the number of blades of the rotor. It should be noted that the latter expressions are valid only for axial flight, since the aerodynamic environment is assumed to be axisymmetric, which means that it is considered uniform in all the points of the rotor [9].

Finally, dT and dQ can be integrated across the whole span of the blades to obtain, respectively, the total thrust, T, and torque, Q:

$$\begin{aligned} T = \int_{Root}^{Tip} dT = \int_{Root}^{Tip} N_b dF_y = N_b \int_{Root}^{Tip} (dL\cos\phi + dD\sin\phi) \\ = N_b \int_0^R \frac{1}{2}\rho U^2 c\,(C_l\cos\phi + C_d\sin\phi)\,dx \end{aligned} \tag{3.13}$$

$$\begin{aligned} Q = \int_{Root}^{Tip} dQ = \int_{Root}^{Tip} N_b dF_z x = N_b \int_{Root}^{Tip} (dL\sin\phi - dD\cos\phi)x \\ = N_b \int_0^R \frac{1}{2}\rho U^2 c\,(C_l\sin\phi - C_d\cos\phi)\,x dx \end{aligned} \tag{3.14}$$

The expressions above are of considerable difficulty of resolution, given to the fact that at each blade element U_T is different - remember that $\|\vec{U}_T\| = \omega x$, which means that this velocity changes with the x-coordinate of the section considered, increasing from $0\ m/s$ at $x = 0\ m$ (root) until its maximum value at $x = R$ (tip). Consequently, this means that both $\vec{U}$ and ϕ will vary across the blade, what causes the variation of α, C_l and C_d. For this reason, all the referred parameters strongly depend on the x-coordinate, making the analytical calculation of the rotor's T and Q challenging.

In addition, the fact that α varies along the blade brings other implications to the rotor. As known from basic aerodynamics, variations of α are also related to variations of C_l and C_d: as α increases to a certain extent, both C_l and C_d increase. However, when α surpasses the critical angle of attack (value of α corresponding to the highest C_l value), α_{crit}, the airfoil stalls due to the separation of the boundary layer from the airfoil, resulting in a loss of L [50, 51]. Considering specifically the nearest section to the root of the blade, for example, where U_T is null, one can easily understand that the α of the section will be very high, perhaps close to $90°$, depending on θ. Therefore, this section will likely be stalled.

According to what was stated previously, the condition for a steady autorotative descent requires $\|d\vec{Q}\|$ to be constant and approximately equal to $0\ N \cdot m$, that is

$$\|d\vec{Q}\| \approx 0\ N \cdot m \Leftrightarrow (\|d\vec{L}\| \sin\phi - \|d\vec{D}\| \cos\phi)x \approx 0\ N \cdot m \tag{3.15}$$

Since C_l and C_d are different across the blade's span, one can comprehend that the steady autorotative condition of equation 3.15 will not be verified for each blade section. In fact, it is only respected at most at two radial sections of the blade [9]. Since between each section both $d\vec{T}$ and $d\vec{Q}$ will vary, certain stations of the rotor will absorb power from the airflow, while others will dissipate it [9]. Nevertheless, this phenomenon results in the sum of the several $d\vec{Q}$'s, expressly the net torque at the rotor shaft, to be approximately equal to zero (i.e., $\int \|d\vec{Q}\| \approx 0\ N \cdot m$), complying with the steady autorotative condition. To sum up, equilibrium is obtained when the accelerating Q due to the blade's lift equals the decelerating Q caused by the blade's drag, in the plane of rotation [28].

The stated phenomenon will then form either two or three different zones in the rotor disk: the driven region, the driving region and, possibly, the stall region. The zones are showed in figures 3.3 and 3.4. Moreover, figure 3.4 explains in a schematic manner the reasons behind the behaviour of the rotor.

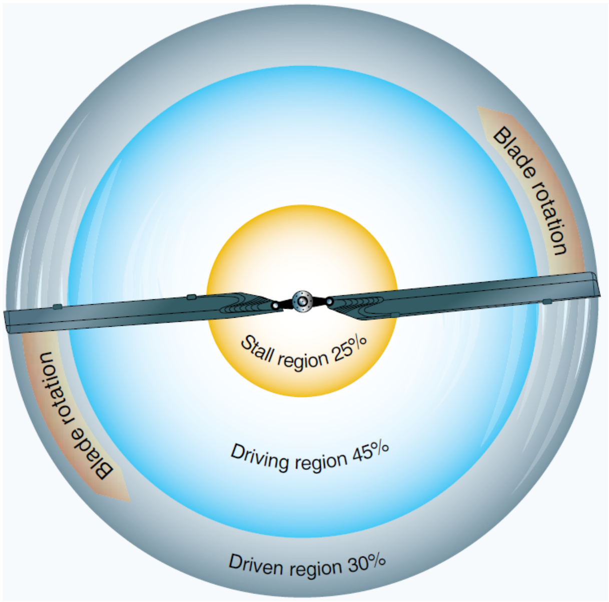

Figure 3.3: Blade regions during an axial autorotative descent [10].

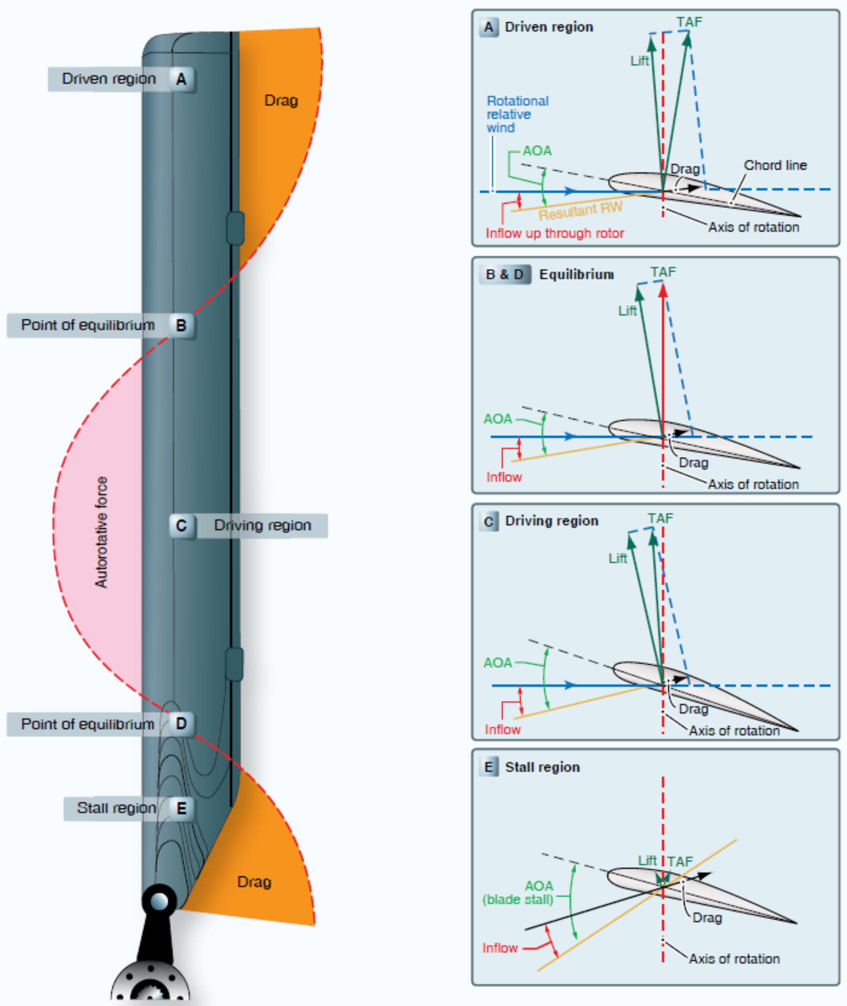
Driven region A
Drag
Point of equilibrium B
Autorotative force
C Driving region
Point of equilibrium D
Stall region E
Drag
A Driven region
TAF
Lift
Rotational relative wind
AOA
Drag
Chord line
Resultant RW
Inflow up through rotor
Axis of rotation
B & D Equilibrium
TAF
Lift
AOA
Inflow
Drag
Axis of rotation
C Driving region
TAF
Lift
AOA
Inflow
Drag
Axis of rotation
E Stall region
Lift
TAF
AOA (blade stall)
Drag
Inflow
Axis of rotation

Figure 3.4: Blade regions and respective aerodynamic forces, for an axial autorotative descent [10].

The different regions will now be approached and analysed separately. The driven region, represented in figure 3.4 by the letter A, is located near the tip of the blade and accounts for about 30% of the blade's radius [10]. Being located closer to the tip, the value of U_T on this zone is at its highest, resulting in a low ϕ and, consequently, a low α (remember that $\alpha = \phi + \theta$). Thus, as seen in the image, the horizontal component of the lift force can not overcome the profile drag, meaning that the horizontal component of the resulting force has an opposite direction to the rotating direction of the blades, decelerating its rotation - the driven region dissipates energy. However, this resulting force also produces T.

Points B and D are two equilibrium points, one located between the driving and driven regions and other between the driven and the stall regions, respectively. In these points, $d\vec{F}_{res}$ only has a vertical component, meaning that it is aligned with the y-axis (see figure 3.1) [10]. Hence the resulting force only produces T and not Q ($dQ = 0\ N \cdot m$), being an equilibrium section.

The region represented by the letter C is the driving region. In this region, U_T is smaller than in region A, which results in higher α's. As observed in figure 3.4, the horizontal component of the lift overcomes the profile drag, producing the necessary force to keep the blades turning. Thus, this blade region absorbs power from the airstream to the rotor, accelerating the rotation of the blades. It consists of about 25 to 70% of the blade's radius [10].

Finally, near the root there is the stall region (letter E), which consists of the remaining 25% of the blade [10]. As one approaches the centre of the rotor, U_T decreases and consequently α increases, becoming higher than α_{crit}. Thus, the airfoil is stalled and drag is produced in this region, decelerating the blades. However, the contribution of this region is not substantial, neither for T nor for Q.

By controlling the size of the regions, the Q and therefore the ω of the rotor can be controlled. This is achieved by varying θ, which significantly affects the aerodynamic forces and moments [34]. Concluding, for achieving a constant ω, θ must be adjusted to a point in which the accelerating moment provoked by the driving region equals the decelerating moment caused by the driven and stall regions. In addition, autorotation is generally a stable equilibrium phenomenon since, when the ω of the rotor increases, ϕ will decrease, which means that the driving region will shrink. This will cause a lower acceleration of the blades, which in turn increases ϕ, causing the driving region to grow, and so on. Therefore, the rotor's ω will adjust itself to maintain a null net Q [9]. Moreover, and as previously referred, θ should be negative (leading edge of the blade pointing down). As seen in figure 3.5, if this angle is negative, the blade's resultant force F_{res} will more likely have its horizontal component pointed towards the leading edge of the blade, inducing its acceleration. On the contrary, a positive angle can result in the blade's deceleration or, even if it provokes acceleration, it will never be as high as in the case of a negative θ.

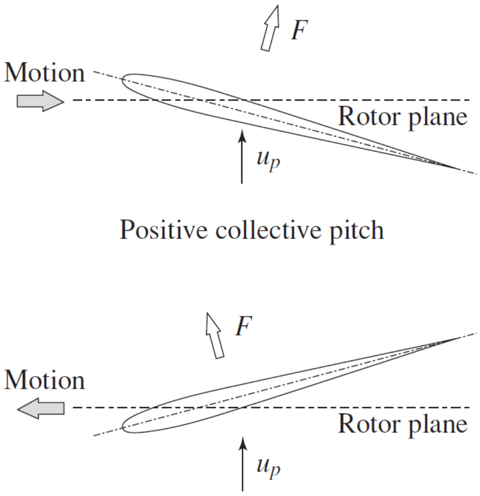

Figure 3.5: Effect of the blade's θ on the resultant force F_{res} and, consequently, on Q. Adapted from [42].

3.2 Computational Model

With the objective of exploring the feasibility of the rotative wings recovery method, a simulation model of a rocket's first stage recovery was developed in MATLAB®. The model's foundations are based on a simple model developed by Amato et al. [52], from the Worcester Polytechnic Institute. The referred model was part of a project for the design, analysis, assembly and testing of a high-powered model rocket for the partial fulfillment of the requirements for the degree of bachelor science in aerospace engineering. In such project, rotative wings were selected as an alternative to parachute recovery and had its feasibility studied for the recovery of the model rocket's nose cone and payload bay. Figure 3.6 shows the CAD (Computer-Aided Design) model of the recovery system developed by the students [52].

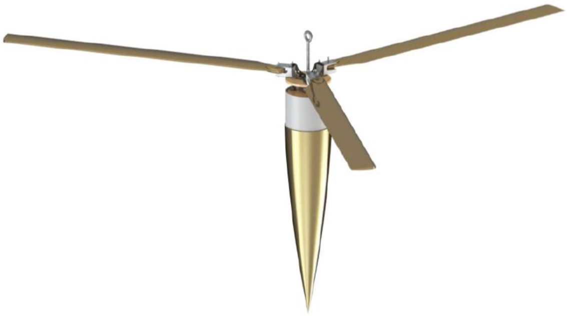

Figure 3.6: CAD model of the autorotation recovery system developed by the students [52].

The student's model and results are available on the respective report [52]. The model simulates the axial descent of the payload with rotative wings. As observed by the students, the simplistic model developed, in combination with the design constraints of the autorotation system, handed results that did not meet the terminal velocity requirements for the recovery's success. Eventually, it was concluded that such recovery method would not be suitable for such a small-scale and light payload [52]. Nevertheless, this model was a useful starting point for the work of this master's thesis, though being extremely simplified and requiring many improvements.

The MATLAB® model developed was then initially a reproduction of the student's model, in order to analyse it and understand what enhancements should be made to bring it as closest to reality as possible. The model developed, along with the improvements made on the original code, will now be explained throughout this section.

The model conceived for this master's thesis is based both on kinematic equations and on the BET. Figure 3.7 displays the coordinate system of the rocket's body (first stage plus rotor), with the x and z-axis being parallel to the Earth and to the rotor plane.

An important approximation worth noticing is that the body's y-axis is assumed to be oriented normally to the Earth's surface at any time, even in the beginning of the simulation. It should be equally noted that, in axial flight, the body only has motion on the y-axis, since the forces that induce it possess such orientation, and no movement is considered on the x and z-axis. Finally, the assumption is made that the forces contributing to the body's motion are applied on its centre of mass and no moments are to be produced, as a distinct approach would highly increase the complexity of this work and would require a further investigation that would go beyond the scope of the proof-of-concept conducted herein. In this manner, the T provided by the rotor will be assumed to be applied on the body's centre of mass, for instance. However, the rotor's Q will induce no direct motion to the first stage, neglecting any moment that it can create on the body, and for that reason it is assumed to only have an effect on the rotor itself.

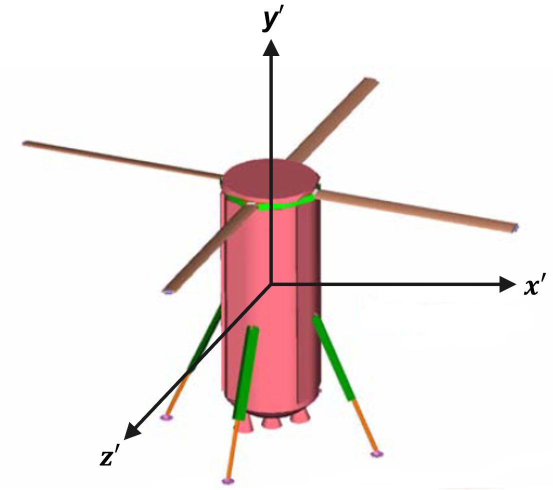

Figure 3.7: Coordinate system of the first stage's body. Adapted from [2].

The flight begins with an axial freefall during a specified period of time, t_{deploy}, until the rotor's deployment. The body initiates the descent at a specific height (vertical distance between the vehicle and the soil, in m), h_0, with no vertical velocity, $v_{v_0} = 0\ m/s$ (velocity of the airflow in relation to the body, which is equivalent to its descent velocity), and an initial acceleration that is equal to the gravitational acceleration, $a_{v_0} = -g$. The freefall is meant to simulate the first stage's descent after its separation from the rocket, as well as to induce a non-null initial vertical velocity at the moment of the rotor's deployment.

When the rotor is deployed its initial angular velocity, ω_0, and angular acceleration, a_{ang_0}, are also assumed as null. Furthermore, several other initial variables regarding the rocket and rotor's design are required. The initial variables are then:

Kinematic conditions

- Freefall initial height, h_0, in m;
- Freefall initial vertical velocity, $v_{v_0} = 0\ m/s$;
- Freefall initial vertical acceleration, $a_{v_0} = -g$, in m/s^2;
- Time until the deployment of the rotor (or time of freefall), t_{deploy}, in s;
- Rotor's angular velocity at deployment, $\omega_0 = 0\ rad/s$;
- Rotor's angular acceleration at deployment, $a_{ang_0} = 0\ rad/s^2$.

Rocket's first stage design parameters

- Length of the first stage, Lt_{stage}, in m;
- Diameter of the first stage, Dm_{stage}, in m;
- Mass of the first stage, m_{stage}, in kg.

Recovery system design parameters

- Number of blades, N_b;
- Radius of the blades, R, in m;
- Chord of the blades, c, in m;
- Collective pitch angle of the blades, θ, in degrees;

In addition, other rotor's design parameters are calculated with the initial variables. The rotor's solidity, σ, and disk loading, DL in kg/m^2, which were presented in chapter 2, are respectively given by

$$\sigma = \frac{N_b A_b}{A_{disk}} = \frac{N_b R c}{\pi R^2} = \frac{N_b c}{\pi R} \tag{3.16}$$

$$DL = \frac{m}{A_{disk}} = \frac{m}{\pi R^2} \tag{3.17}$$

in which A_b is the area of a blade in m^2, A_{disk} is the area of the rotor's disk also in m^2, and $m = m_{stage} + m_{recovery}$ is the total mass of the system.

To estimate the mass of the recovery system, $m_{recovery}$, the ARMADA project researchers [44] (see subsection 2.3.7) held a dimensional analysis of current rotors and established a simple model based on a power law, which is:

$$m_{recovery} = m_{rotor} + m_{control} = 0.4 N_b R^{2.6} + 2.75 R^{1.8} \tag{3.18}$$

where m_{rotor} is the rotor's mass (assumed to depend on N_b) and $m_{control}$ is the control system's mass, in kg. The control system is used, for instance, to vary θ in case of a flare manoeuvre. Since R has an exponent, the mass will suffer higher variations as R increases, which is quite pessimistic since it is overpredicted, namely when assessing the recovery of a light model-rocket. However, it was the best and more simplistic manner to predict the mass variation with R, taking into account that neither assuming a constant mass for different R values, or assuming a mass range (estimations for 10% to 15% of the gross mass referred in section 2.3) would be realistic and allow for the analysis of R alteration.

The initial freefall is based on kinematic motion equations and computed through an iterative process, which allows for the calculation of the successive heights, h, vertical velocity vector, $\vec{v}_v$, and acceleration vector, $\vec{a}_v$, of the body during the drop. Note that $\vec{v}_v$ is equivalent to $\vec{V}_c$ (see equation 3.1), even though $\vec{v}_v$ is represented on the first stage's coordinate system, while $\vec{V}_c$ is on the rotor's one.

As stated above, a_{v_0} is merely the gravitational acceleration, g, which has a negative direction on the body's y-axis of figure 3.7, and depends on the system's h, according to the law of universal gravitation,

$$\vec{g} = -G \frac{m_{Earth}}{(R_{Earth} + h)^2} \vec{e}_{y'} = -g \vec{e}_{y'} \tag{3.19}$$

in which $G = 6.674 \cdot 10^{-11}\ Nm^2/kg^2$ is the gravitational constant and $m_{Earth} = 5.972 \cdot 10^{24}\ kg$ and $R_{Earth} = 6.371 \cdot 10^6\ m$ are the mass and radius of the Earth, respectively.

As observed, g decreases with h, and such variation is accounted by the model during all the descent, since g is constantly updated for each h. This variation was not accounted in the original model developed by the students [52], nor was the drag provoked by the first stage's body. As the vehicle descends, a_v is also influenced by the vertical drag force of the first stage, $\vec{D}_{stage}$, becoming

$$\vec{a}_v = \left(\frac{D_{stage}}{m} - g\right)\vec{e}_{y'} = a_v\vec{e}_{y'} \tag{3.20}$$

where $\vec{D}_{stage}$ and $\vec{g}$ have opposite directions. For simplicity in the computation of the body's drag, the first stage is assumed to be a cylinder with length Lt_{stage} and diameter Dm_{stage}, so that

$$\vec{D}_{stage} = \left(\frac{1}{2}\rho C_{d_{stage}} \left\|\vec{v}_v\right\| A_{base}\right)\vec{e}_{y'} \tag{3.21}$$

in which $C_{d_{stage}}$ is the cylinder's axial drag coefficient and A_{base} is the reference area, in this case the area of the cylinder's base, $A_{base} = \pi(Dm_{stage}/2)^2$, in m^2.

For obtaining $C_{d_{stage}}$, experimental values of CFD (Computational Fluid Dynamics) simulations conducted by researchers were employed [53]. The researchers studied the variation of this coefficient on a cylinder under axial airflow (normal to the cylinder's base) with its aspect ratio, $AR = (Lt/Dm)_{stage}$. With data adapted from the cited research, a curve of $C_{d_{stage}}$ as a function of AR is generated, enabling the extraction of the $C_{d_{stage}}$ value, as seen in figure 3.8. The curve is a smoothing spline created through the MATLAB® fit function, which produces a curve that follows the input data points and fits the remaining points. Since $C_{d_{stage}}$ depends only on two fixed variables, it is constant throughout the simulation.

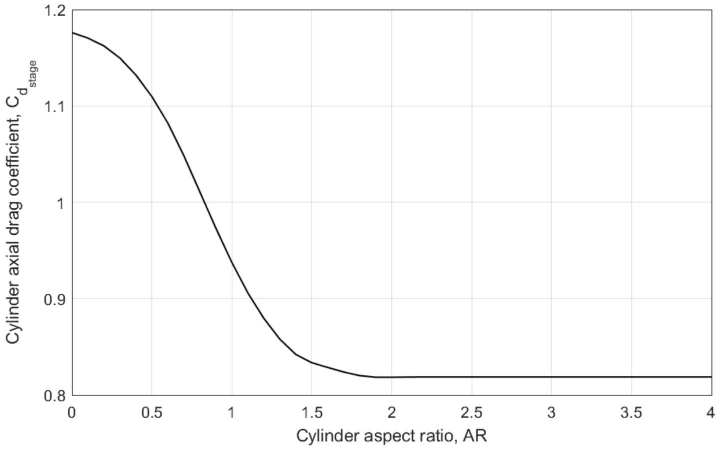

Figure 3.8: $C_{d_{stage}}$ of the first stage as a function of its $AR = (Lt/Dm)_{stage}$. Data collected from [53].

From equation 3.21, it is seen that ρ is required for the computation of $\vec{D}_{stage}$ as well. The atmospheric parameters of air density, ρ, and temperature, Tp (in K), vary with altitude and should therefore be computed for each h. This was achieved by resorting to empirical data provided by the NRLMSIS 2.0 atmospheric model [54], which contains data for altitudes up to $1000\ km$. The data is inputted into the model, that creates a curve fit function for both ρ and Tp with h, which can be observed in figures 3.9(a) and 3.9(b), respectively. The original model did not account for such variation [52], which is of extreme importance when considering high altitudes, especially because ρ decreases immensely with h, being more than 10^9 times lower at $200\ km$ in comparison to its value on the Earth's surface.

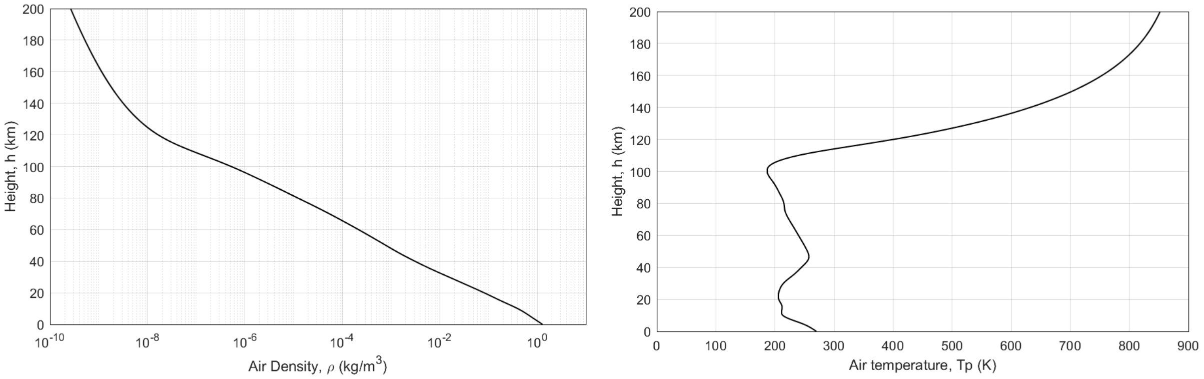

(a) ρ variation with h.

(b) Tp variation with h

Figure 3.9: Atmospheric parameters variation with h. Data extracted from NRLMSIS 2.0 [54].

Finally, with $\vec{a}_v$ it becomes possible to compute $\vec{v}_v$ and consequently h for the next iteration, resorting to the equations of motion

$$\vec{v}_v = \left(v_{v_0} - a_v dt\right) \vec{e}_{y'} \tag{3.22}$$

and

$$h = h_0 - \|\vec{v}_v\|\, dt + \frac{1}{2}\|\vec{a}_v\|\, dt^2 \tag{3.23}$$

in which v_{v_0} and h_0 are the initial vertical velocity and height, respectively, at the beginning of each iteration, being constantly updated for the following one, and dt is the time step of the simulation, in s. The time of the simulation, t, in s, is continuously updated as well:

$$t = t_0 + dt \tag{3.24}$$

When $t = t_{deploy}$, the rotor is deployed and the BET aerodynamic equations are used to calculate the forces applied in the rotor and the consequent forces on the body of the first stage, which induce its deceleration. As an approximation, the rotor is assumed to be instantly deployed, meaning that its deployment was not modelled, as such addition would add an increased level of complexity that would not be of great significance for the results. Following the deployment, the model enters an iterative process until the body touches the ground, i.e., until $h = 0\ m$.

Immediately after the rotor's deployment, the airflow induces the generation of forces on the blades. However, it was seen in section 3.1 that such forces are distinct along the blade. For this reason, the model considers the blade as having $n_{sections} = R/dx$ sections, each with a length dx, and for each section calculates the infinitesimal forces on it, to obtain the total forces on the rotor. Following the BET, with $\vec{U}_P$ (equation 3.1), $\vec{U}_T$ (equation 3.2) and θ it is possible to calculate $\|\vec{U}\|$, ϕ and α using equations 3.4, 3.5 and 3.6, respectively (consult appendix A). The following step is to compute $\|d\vec{L}\|$ and $\|d\vec{D}\|$

through equations 3.7 and 3.8, respectively. Such calculation involves the values of C_l and C_d, which in turn will depend on α and on the Reynolds number, Re [51]. The Re at each blade element is equal to

$$Re = \frac{\rho \|\vec{U}\| c}{\mu} \tag{3.25}$$

where μ is the dynamic viscosity of the air in $kg/(m \cdot s)$, which is continually updated throughout the simulation as well, given by the Sutherland's Law:

$$\mu = 1.716 \cdot 10^{-5} \left(\frac{Tp}{273}\right)^{3/2} \frac{384}{Tp + 111} \tag{3.26}$$

To compute the values of C_l and C_d, the model requires plots of both variables as a function of α, for each Re. For this, the first step was to decide the airfoil of the blades. In accordance with the original model, the chosen airfoil was NACA 0012 [52], mainly because it is commonly used in helicopters and, more importantly, has been widely studied, giving a certain degree of confidence on its performance.

As in the original model [52], the approach for obtaining the C_l and C_d plots was to conduct simulations in the aerodynamic software XFLR5®. After selecting the NACA 0012 airfoil in the software, simulations were run on the 2D airfoil for the following Re values: $1,000$ to $10,000$, with an increment of $1,000$; $10,000$ to $100,000$, with an increment of $10,000$; $100,000$ to $1,000,000$, with an increment of $100,000$; and $1,000,000$ to $20,000,000$, with an increment of $1,000,000$. For each of the referred Re, plots of C_l and C_d were computed for α's from $-5°$ up to $30°$. This is a higher range than the one selected by the students [52].

Nonetheless, as stated in section 3.1, the sections near the blade's root have much higher α's, some being close to $90°$. This fact raised a difficulty, since XFLR5® predicts with good reliability the aerodynamic flow until α_{crit}, but it fails to compute trustworthy coefficient values after the separation of the boundary layer [55].

In the original model [52], the solving of this problem was rather inaccurate. Firstly, the data from the XFLR5® software was inputted into MATLAB® for α's up to $25°$. Secondly, the Re at each blade element was rounded to match the closest Re containing the aerodynamic data and curve fit functions of the coefficients as a function of α were generated. Then, for the current function, α_{crit} would be calculated by its defining condition $dC_l/d\alpha = 0$ and, if the blade's section α was higher than α_{crit}, the model would create new functions with specific data for stalled conditions. The stalled data is presented in figure 3.10, and no reference was given regarding its origin [52].

Following a literature investigation regarding the experimental aerodynamic behaviour of a NACA 0012 airfoil for high α's [56–58], it was concluded that the stalled values utilised by the students were quite incorrect. The C_l curve, computed as a quadratic function [52] (see figure 3.10), is close to reality, although its maximum value was highly overestimated. As for the C_d, it was not only underestimated over all the range of α's, but its variation was considered as being linear [52], which is also incorrect.

Another wrong approximation was that these stall data were considered to be equal for all Re's [52]. The cited studies of wind tunnel experiments for high α's demonstrate that the aerodynamic coefficients maintain its high dependence on Re even at $\alpha > \alpha_{crit}$, becoming eventually independent of Re above a certain α [56–58]. Thus, the stalled data should be treated for each Re value.

In addition, the stalled data inputted in the original model only considers values starting at $\alpha \approx 19^\circ$, as seen in figure 3.10 [52]. Nevertheless, α_{crit} commonly falls below such value. Moreover, the fit function will follow its curve for values below 19°, so the coefficients' values computed in this range were also fully wrong - the real aerodynamic behaviour is utterly different. After the airfoil enters the stalled operation, associated with the separation of the boundary layer and consequent loss of lift and increase of drag, there is a post-stall region. In such region, the increase of α will induce a recovery of lift, while the drag keeps on increasing [56–58]. This means that, since the original model considers a change of function when in stalled conditions, at α's corresponding to the separation of the boundary layer or at α's related to the beginning of recovery, the coefficients' curves with α do not consider the phenomena referred. Consequently, the original model [52] is far from reality and improvements had to be performed.

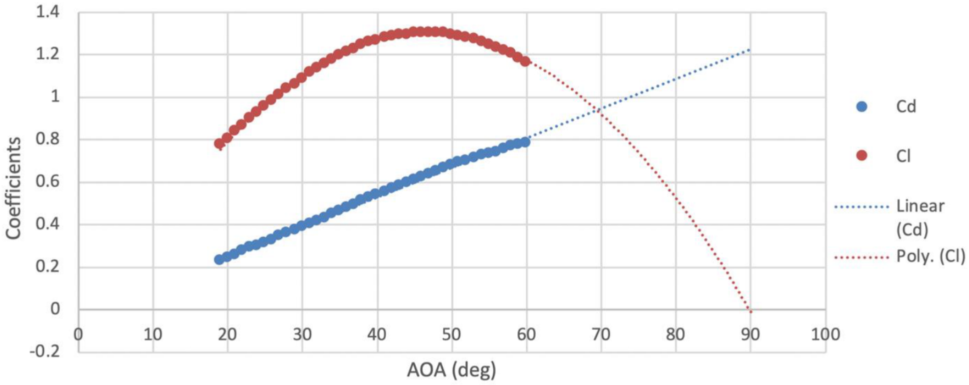

Figure 3.10: C_l and C_d stall data as a function of α used in the original model. The C_l function (red) was computed as a quadratic function and the C_d function (blue) was considered to be a linear function [52].

Considering the flaws described above, a different approach was considered for this master's thesis, with the objective of making sure that the aerodynamic data was reliable.

Firstly, data for α up to 30° were taken from XFLR5® for the Re range referred above. However, as stated before, XFLR5® does not perform ideally for stalled conditions. Consequently, wind tunnel experimental data at high α's were considered for $Re = 150,000$ (from Rainbird et al. [58]). Considering the data provided by XFLR5® and by the wind tunnel experiments [56, 57] it is clear that, above a certain α, the coefficients become independent of Re, as previously discussed. Thus, it is acceptable to use experimental values measured for a single Re. For the Re range between $1,000$ and $900,000$, that value of α is approximately 19.29°, while for the remaining Re's it is approximately 29.29°. The decision was then made that the XFLR5® and experimental data should be concatenated in one single data file, without the necessity to compute α_{crit} and update the C_l and C_d functions in the case of a stalled operation. This approach is simpler and more correct, allowing for a "continuous" function.

Despite this, the coefficients are still highly depend on Re between α_{crit} and the referred angles. This created a new problem since the experimental data acquired for a single Re value does not comply with such dependency.

In addition, considering only the XFLR5® or only the experimental data in this range would create discontinuities on the curves, since the data from the two sources do not match perfectly, understandably. Thus, if only the experimental data was considered after α_{crit}, there would be a great discontinuity immediately after α_{crit}. On the other side, if only the XFLR5® values were to be used for the referred range, a discontinuity would also exist at the angles of $19.29°$ or $29.29°$, depending on Re.

The solution was to consider both data for this range, with a weighting being made. Until α_{crit}, the XFLR5® data is used without considering the experimental data - the computational data has a weight of 100%. Between α_{crit} and the α of $19.29°$ or $29.29°$, depending on Re, the weight of the XFLR5® data is progressively decreased with increasing α, while the experimental data's weight is increased. Finally, at the referred angles and onward, the experimental data has a weight of 100%. This solution was found to be the best way to create a trustworthy database of C_l and C_d for a vast Re range, with smooth curves that depend on Re and consider α's up to $90°$.

It is worth noticing that the author is aware that the most reliable database would consist only of experimental data for the whole α range. However, no experimental data was found for the amount of Re values considered by the model. Since Re varies considerably around the blade, priority was given to acquiring data for a large number of Re's, only possible through computational simulations.

As a clarification, figure 3.11 depicts the C_l and C_d variation with α for $Re = 250,000$: until $\alpha_{crit} \approx 12°$, computational data is used; between α_{crit} and $\alpha = 19.29°$, a combination of both computational and empiric data is considered; finally, above $\alpha = 19.29°$, only experimental data is present. By comparing figure 3.11 with figure 3.10 for the values above $\alpha_{crit} \approx 12°$, one can clearly notice the differences between the curves and the values of the coefficients. Unlike the original model [52], the selected approach considers the phases of loss of lift and the beginning of its recovery, being more trustworthy.

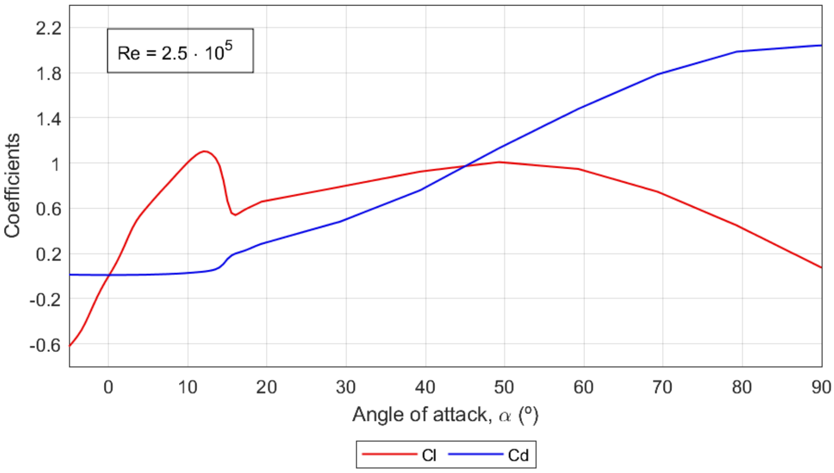

Figure 3.11: C_l (red) and C_d (blue) as a function of α for $Re = 2.5 \cdot 10^5$, for the selected approach.

With the Re of the blade's section, the C_l and C_d curve fit functions are then created and, with the input of α, the coefficients are obtained. Subsequently, $\|d\vec{L}\|$ and $\|d\vec{D}\|$ are computed with equations 3.7 and 3.8, respectively, and using the blade element's ϕ, the $d\vec{F}_y$ and $d\vec{F}_z$ forces are also obtained through equations 3.9 and 3.10. Finally, the rotor $d\vec{T}$ and $d\vec{Q}$ are calculated from equations 3.11 and 3.12.

The process described above is computed iteratively throughout the span of the blades. After the blades are analysed, the rotor's $\vec{T}$ and $\vec{Q}$ are obtained. Even though such calculation, present in equations 3.13 and 3.14, requires an integration of the infinitesimal forces across the blade, an approximation was made and the model calculates $\vec{T}$ and $\vec{Q}$ by summing the contributions of each blade element:

$$\vec{T} = \sum_{j=1}^{n_{\text{sections}}} d\vec{T}_j \tag{3.27}$$

$$\vec{Q} = \sum_{j=1}^{n_{\text{sections}}} d\vec{Q}_j \tag{3.28}$$

As $\vec{T}$ contributes to the body's deceleration, the next iteration's $\vec{a}_v$ is, then

$$\vec{a}_v = \left[\left(\frac{T + D_{stage}}{m}\right) - g\right] \vec{e}_{y'} \tag{3.29}$$

and, with the new $\vec{a}_v$, $\vec{v}_v$ and h for the next iteration are also calculated resorting to equations 3.22 and 3.23, respectively. Note that both v_{v_0} and h_0 are updated for the next iteration as well by receiving the most recent computed values of $\vec{v}_v$ and h. Additionally, the new h allows for the calculation of g, ρ and Tp of the next iteration. The whole process is displayed in a flowchart in appendix A.

In the same manner, kinematics of rotational motion is used to calculate the next iteration's angular acceleration vector, $\vec{a}_{ang}$, and $\vec{\omega}$, on the blade's coordinate system. Thus, one gets

$$\vec{a}_{ang} = \frac{Q}{I_{rotor}} \vec{e}_y \tag{3.30}$$

$$\vec{\omega} = (\omega_0 + a_{ang} dt)\, \vec{e}_y \tag{3.31}$$

where I_{rotor} is the rotor's moment of inertia, in $kg \cdot m^2$.

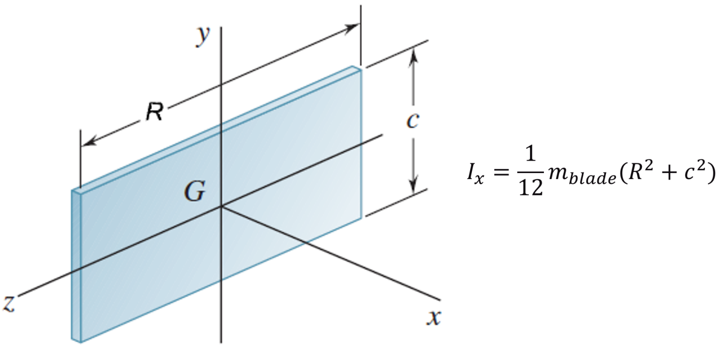

Figure 3.12: Moment of inertia, I, for a thin rectangular plate with respect to the x-axis, used for the calculation of I_{blade}. Adapted from [59].

To calculate I_{rotor}, it is assumed that the rotor is only composed by the blades and that these can be approximated as thin rectangular plates, observable in figure 3.12, since the blades are rectangular. The parameter m_{blade} observed in the figure refers to the mass of one blade, assuming that $m_{blade} = m_{rotor}/N_b$, which means that $I_{rotor} = N_b I_{blade}$.

Such approximation was made considering that I_{rotor} would not deviate considerably from the real value and it would not be time affordable to perform a CAD model of the rotor merely for calculating this variable, when there are tabulated values for the I of simpler bodies [59].

Resorting to the parallel axis theorem to shift the plate's edge to the centre of rotation [59], one has

$$I_{rotor} = N_b I_{blade} = N_b \left(\frac{1}{12} m_{blade} \left(R^2 + c^2\right) + m_{blade} \left(\frac{R}{2}\right)^2 \right) = \frac{1}{12} m_{rotor} \left(4R^2 + c^2\right) \tag{3.32}$$

From here on, for simplicity, the vector variables will not be represented as vectors but as scalars, but the reader should be aware of their nature as well as their orientation on the coordinate systems of figures 3.1 and 3.2, when it comes to the blade, and of figure 3.7, when it comes to the first stage's body.

After the calculations for the following iteration, other parameters for the rotor's performance analysis are computed. The rotor drag coefficient, C_{d_R}, is a dimensionless measurement of T [9] and is given by

$$C_{d_R} = \frac{T}{\frac{1}{2} \rho {U_P}^2 A_{disk}} \tag{3.33}$$

and the axial advance ratio, λ_{axial}, is the ratio between the vertical component of the airflow velocity in the rotor, U_P, and the tip velocity, V_{tip} [9], equal to

$$\lambda_{axial} = \frac{U_P}{V_{tip}} = \frac{U_P}{\omega R} \tag{3.34}$$

Furthermore, the Mach number at the blade's tip is calculated from

$$M_{tip} = \frac{V_{tip}}{c_{sound}} \tag{3.35}$$

where c_{sound} is the velocity of sound in air, in m/s, given by

$$c_{sound} = \sqrt{\gamma R T p} \tag{3.36}$$

where γ = 1.4 is the air heat capacity ratio and $R = 287\ J/(kg \cdot K)$ is the air specific gas constant [51], which are assumed to be constant. The air is assumed to be a perfect gas, so only dependent on Tp [51] and thus also updated throughout the simulation.

These variables were not considered in the original model [52], since the analysis made by the students was not as thorough, focusing only on the terminal v_v and not on the rotor's performance.

Following these calculations, the time of the simulation is incremented and the described process restarts, until $h = 0\ m$. All the parameters liable to analysis are stored in vectors for further analysis.

3.2.1 Axial Induced Velocity in Axial Flight

As observed in equation 3.1, U_P depends not only on V_c but also on the axial induced velocity, v_i. This velocity is used to compute the inflow through the rotor (negative on the y-axis of figure 3.1, meaning that it flows downwards through the rotor) and represents an important component that should be taken into account in models involving rotors, since it alters the vertical velocity of the airflow on the blades. Such parameter was not considered in the original model [52].

It is assumed that v_i is uniform through the rotor (axisymmetric). To obtain it, the momentum theory (considers the control volume of the rotor and its wake and applies conservation laws through quasi-one-dimensional integral formulas to study the rotor's performance [9]) in axial flight is put into practice and the velocity in a state of hover, v_h, must be considered [9]. In hover, T is equal to the weight of the body [9], $T = W = mg$, and v_h, on the coordinate system of figure 3.1, is given by

$$v_h = \sqrt{\frac{T}{2\rho A_{disk}}} = \sqrt{\frac{W}{2\rho A_{disk}}} = \sqrt{\frac{mg}{2\rho\pi R^2}} \tag{3.37}$$

For an axial descent ($V_c > 0$), the rotor has two different operating modes, depending on V_c, in which v_i presents distinct behaviours, as observed in figure 3.13 [9]. Note that the y-axis considered in this figure has the opposite direction of the y-axis of the rotor selected in this document, which means that in the figure V_c/v_h has negative values for a descent and v_i/v_h is positive.

On this document's coordinate system, for $V_c > 2v_h$, the rotor operates in the windmill brake state, in which the slipstream is well-defined and the momentum theory can be applied [9]. On the contrary, for $0 \leq V_c \leq 2v_h$, the rotor is in the vortex ring state and the momentum theory is invalid [9]. The vortex ring state is a state of highly unstable flow with regions of both upward and downward airflow, being prejudicial for the rotor's performance [9]. Considering the latter state would not be favourable for the confidence of the results, since it is related to airflow's unsteadiness and turbulence caused by tip vortexes [9], which would not be predicted due to its complexity. For this reason, the model considers only the windmill brake state and avoids the vortex ring state, breaking if $0 \leq V_c \leq 2v_h$.

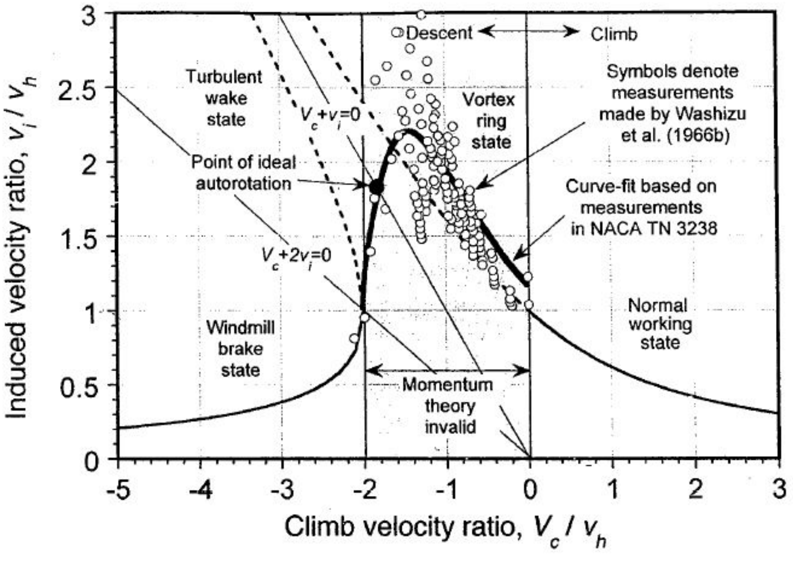

Figure 3.13: Induced velocity ratio, v_i/v_h, as a function of the climb velocity ratio, V_c/v_h, in which the windmill brake state and the vortex ring state zones are observable [9].

Thus, considering the windmill brake state ($V_c > 2v_h$) the momentum theory leads to v_i, which is

$$v_i = v_h\left(\frac{V_c}{2v_h} - \sqrt{\left(\frac{V_c}{2v_h}\right)^2 - 1}\right) \tag{3.38}$$

However, if for some exception it becomes necessary to consider the vortex ring state, it is possible to resort to empirical data in order to define the v_i curve of figure 3.13 [9], and v_i is given by

$$v_i = v_h\left(1 + 1.125\left(\frac{V_c}{v_h}\right) - 1.372\left(\frac{V_c}{v_h}\right)^2 + 1.718\left(\frac{V_c}{v_h}\right)^3 - 0.655\left(\frac{V_c}{v_h}\right)^4\right) \tag{3.39}$$

Nonetheless, the above expression fails to consider, of course, the aerodynamic instabilities of this state, and should only be utilised if strictly necessary.

As seen on equations 3.38 and 3.39, the calculation of v_i requires the value of V_c for the current iteration. Nevertheless, as described in the previous subsection, V_c is obtained through the forces in the rotor, which in turn depend on U_P, that depends on v_i. Such difficulty was resolved by implementing one more iterative process, interior to the iterative process that terminates when $h = 0\ m$, and exterior to the iterative process that runs through the infinitesimal sections of the blade.

Thus, in such method, the process described in the previous subsections is continuously repeated for the same h. Utilising the value of v_i, which is $v_i = 0\ m/s$ in the first iteration (when the rotor is deployed), U_P is calculated and with it the remaining parameters, until reaching the calculation of the next time step's kinematic variables. At this point, a new v_v is obtained, v_h is calculated through equation 3.37 and the model guarantees that the rotor is operating in the windmill brake state. If such statement is true, v_i is computed using equation 3.38. A new value of U_P is computed with equation 3.1 and stored in a vector. Then, the whole process restarts for the new U_P and U_T (since ω varied as well), and so on (always for the same h). The iterations proceed until the calculated U_P converges, with a convergence criterion of 10^{-4}, which is low enough for the convergence to be reliable. This means that, if the difference between U_P of the current convergence iteration and U_P of the previous one is less than 10^{-4}, the convergence process ceases, and all the parameters are once again calculated for the most recent U_P and U_T. The h for the next iteration is obtained and the model proceeds for the next time step (consult appendix A).

The addition of v_i to the model improves its reliability, bringing it closer to reality by considering an important part of the airflow through the rotor. Nevertheless, the model can be run with or without v_i, because this converging cycle results in the repetition of the calculations for the same h until reaching convergence, which means that the simulation's computational time increases dramatically. When running the model without v_i, it is simply assumed that $v_i = 0\ m/s$ and consequently that $U_P = V_c$, and the cycle for U_P's convergence is not necessary. Appendix B discusses the impact of v_i on the simulations.

3.2.2 Model Verification

Before getting into details about the studies conducted on the model, its validation and verification should be held to ensure its reliability. The verification process proved to be more challenging than expected at first glance. The best approach would be, perceptibly, to compare the results with data from the literature, or experimental results. However, unfortunately, it was not possible to perform quantitative comparisons with the results present in the literature studies of chapter 2, for several reasons.

In the first place, the vast majority of the referenced studies does not possess sufficient information to enable its reproduction, regarding problem constants - namely the kinematic parameters h_{deploy} and $v_{v_{deploy}}$ or rocket and rotor design variables such as m_{stage}, $m_{recovery}$, c or I_{rotor}. Secondly, some works are either too broad, not offering enough detail about the studies conducted, or too specific, focusing on complex details that are beyond the scope of this proof of concept. Thus, a reference that studies the system's performance throughout the whole descent, by addressing the forces, accelerations, velocities and height variations with time, such as the one developed in this work, was not found.

In addition, the studies that could potentially be subjects of comparison have certain particularities that were not included in the model. For instance, in [42], the authors consider blade hinge and coning angles, which are intended to passively control the θ of the blades. It was discussed in section 2.3 that θ provokes major differences on the system. Since that in this work's model θ is constant, it becomes impossible to compare it quantitatively with the results in [42]. Likewise, the ARMADA project's predictions in [44] present some interesting plots for comparison. However, some variables like the payload's dimensions and blade's c were absent and, more significantly, the simulation described was intended for a Mars landing, being rather different than a landing taking place on Earth. As for the Kaman *Rotochute* results presented in [29], the terminal v_v expected for the system is the only disclosed data. Moreover, the latter study assumes deploy at supersonic velocities, the effects of which were not accounted for in the computational model developed. These particularities, among others, provoke quite a difference in the results, making it difficult to quantitatively compare them with this work.

The solution found was to take an approach that is more focused on the behaviour of the physical variables of the problem, and to provide as many qualitative comparisons with the literature as possible, allowing then to perform the model's verification. To do this, a simulation was run considering a rocket that will be described further on this document (see section 4.1 for more details). The values of the selected rotor design and simulation defining parameters can be seen in tables 3.1 and 3.2, respectively.

Table 3.1: Rotor's design parameters for the verification of the model.

N_b	$R\,[m]$	$c\,[m]$	$\theta\,[^\circ]$	σ
3	1	0.17	-10	0.162

Table 3.2: Parameters of the simulation for the verification of the model.

$dx\,[m]$	$dt\,[s]$	v_i convergence criteria
0.01	0.01	10^{-4}

The design parameters chosen are illustrative and do not guarantee a good performance of the system, since that is not the focus of this part of the work. On the other side, the selection of the model containing v_i, and of $dx = 0.01\ m$ and $dt = 0.01\ s$ is made to achieve results as realistic as possible.

The objective behind this study is to offer an analysis of the simulation, justifying and assisting with the comprehension of the general performance of the system and, particularly, of the rotor. By carefully examining its behaviour and with the knowledge of the physical principles behind it, it is possible to carry out the verification of the model, based on whether it performs accordingly to what is expected. Moreover, this study is complemented with qualitative comparisons with some of the literature data, that can assure the model's verification.

The plots of h, v_v, a_v, g force (a_v/g), ω and a_{ang} with t can be seen in figures 3.14(a), 3.14(b), 3.14(c), 3.14(d), 3.14(e) and 3.14(f), respectively.

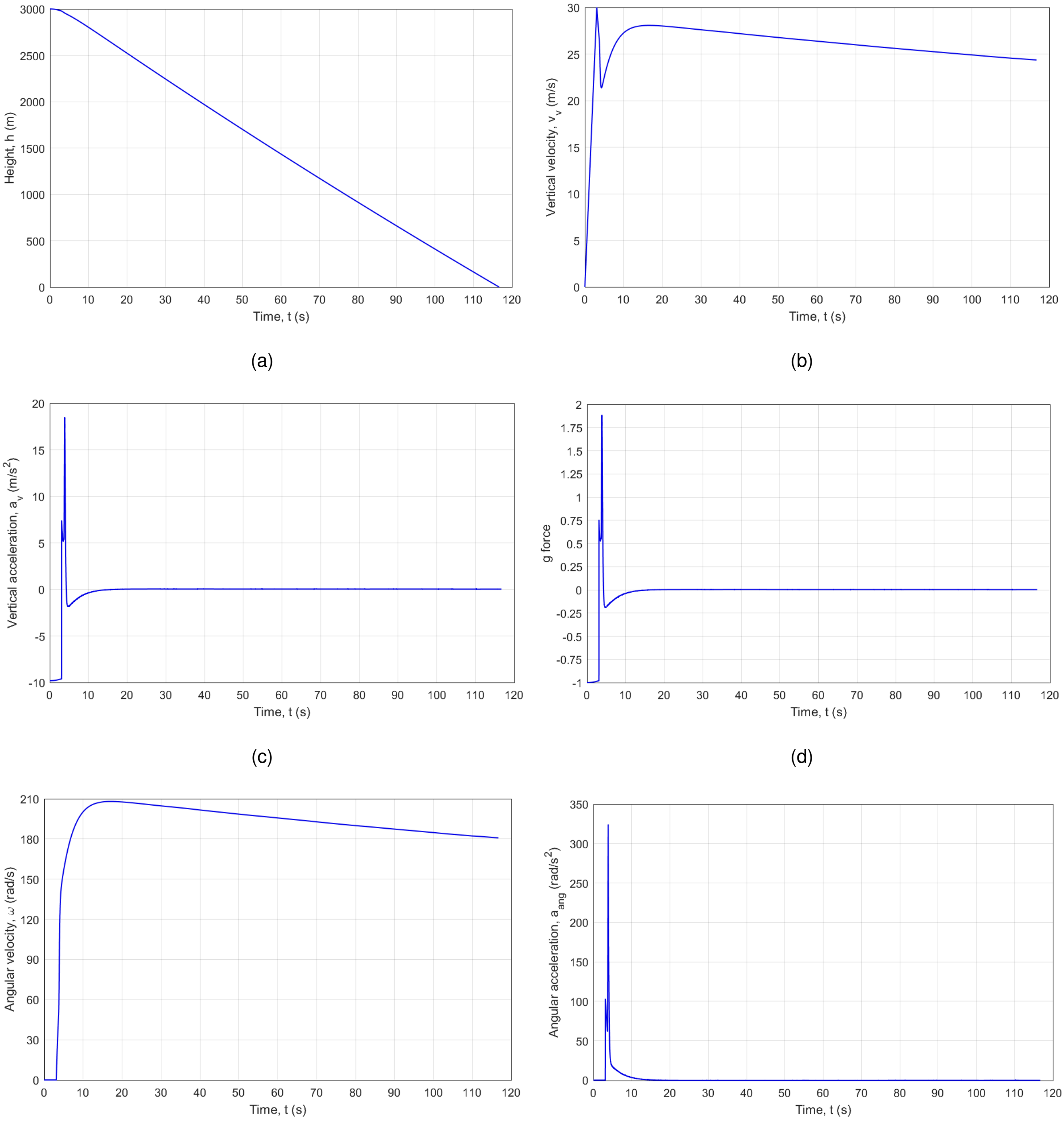

(a) (b) (c) (d) (e) (f)

Figure 3.14: Evolution of h (a), v_v (b), a_v (c), g force (d), ω (e) and a_{ang} (f) with t for the verification of the model.

As will be described further on this document, the rocket initiates its descent at $h_0 = 3,000\ m$ without the rotor being deployed, for $t_{deploy} = 3.09\ s$. During the freefall, the only forces acting on the rocket are the gravitational force, which for such a short descent does not vary significantly, and the body's drag. The effect of the latter force becomes clear by analysing the plot of a_v for the freefall, since it increases slightly with t (becomes less negative). Following the freefall drop, the rocket has a v_v of $v_v = v_{v_{deploy}} \approx 30\ m/s$.

As soon as the rocket is deployed at $t_{deploy} = 3.09\ s$, the a_v plot shows a peak of $a_v \approx 7.36\ m/s^2$ (g force of approximately $0.75\ g$'s) that decelerates the descent. Such peak is explained for the mere appearance of the rotor (remember that the deployment process was not modelled), since the blades act similarly to flat plate drag surfaces, which means that they are fully stalled. The a_v value immediately starts decreasing, tending towards a null value that ensures equilibrium conditions, while v_v decreases. In the same manner, a_{ang} presents a similar tendency that raises ω, explained by the beginning of the rotation of the rotor when subjected to the freestream.

However, around $t = 3.70\ s$, a new acceleration raise is observed, which later origins a second acceleration peak of $a_v \approx 18.47\ m/s^2$ (approximately $1.88\ g$'s). A second (and greater) peak also occurs for a_{ang}. Thus, v_v decreases substantially and, oppositely, ω increases. Figures 3.15(a) and 3.15(b) display with more detail this phenomenon, with the black vertical line highlighting its beginning. Such acceleration peaks are justified by the fact that the rotor transitioned from being fully stalled to being only partially stalled. The previous plots of v_v and ω show a higher variation from this point on, as well.

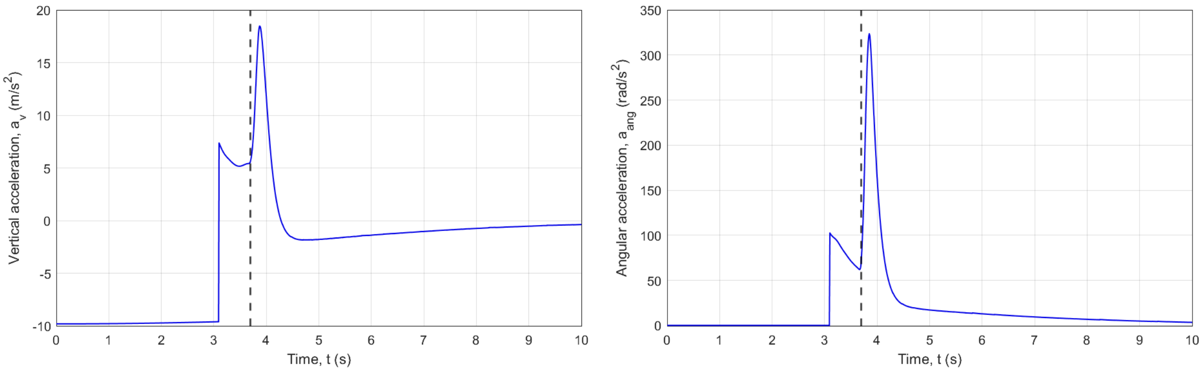

(a)

(b)

Figure 3.15: Evolution of a_v (a) and a_{ang} (b) with t, with the second acceleration peak highlighted.

To understand this transition that deeply influences the system's behaviour, it is necessary to look with detail into what happens in the rotor at this point. As explained in section 3.1, U_T increases as one moves from the blade's root to its tip, and consequently α decreases. In addition, it is known that a fully stalled blade implies that $\alpha > \alpha_{crit}$ for all blade sections. Figure 3.16 shows the α distribution along the blade's nondimensional spanwise coordinate (on the x-axis of figure 3.2), x/R, at three different times for comparison: at $t = 3.41\ s$ (before the second acceleration peak), at $t = 3.87\ s$ (at the point of maximum acceleration) and at $t = 116.69\ s$ (at the end of the simulation). On the root, all curves have $\alpha = 80°$, since $\phi = 90°$ ($U_T = 0\ m/s$) and $\theta = -10°$. As anticipated by the theory, as x/R increases,

α becomes smaller. However, it becomes clear that at $t = 3.41\ s$, before the second acceleration peak appears, the blade is fully stalled, since the minimum α achieved is $\alpha = 31.6°$, which is higher than α_{crit} for the whole blade. On the contrary, at $t = 3.87\ s$ and $t = 116.69\ s$ the blade is partially stalled, which is confirmed by the fact that $\alpha < \alpha_{crit}$ in the majority of the blade's sections. Moreover, it is seen that at $t = 3.87\ s$ the blade possesses more stalled regions than at $t = 116.69\ s$. In fact, for $t = 116.69\ s$ and at $x/R = 0.3$, one has $\alpha \approx 13.1°$, which is lower than $\alpha_{crit} \approx 13.5°$. From this point onwards, the blade is no longer stalled, meaning that 70% of the blade is unstalled at the moment of touchdown. For qualitative comparison, a graph of the same sort is present in [19], which confirms the correct behaviour of the model.

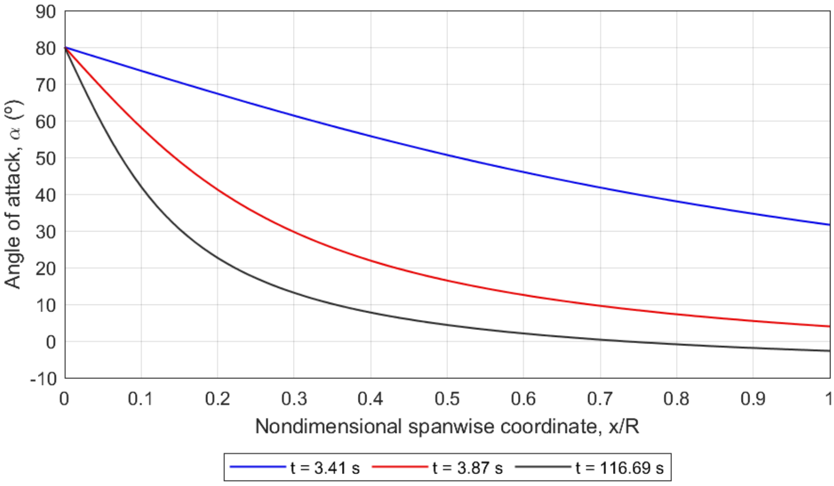

Figure 3.16: Spanwise distribution of the α of a blade's element for $t = 3.41\ s$, $t = 3.87\ s$ and $t = 116.69\ s$.

This variation of the α's distribution can be easily explained. Just after the rotor's deploy, U_P is high and U_T is low, which results in great α's. Nonetheless, as the rotor decelerates the system by acting as a flat drag plate, U_P decreases and U_T increases, and the α's become lower across the blade. The blade evolves by becoming less stalled and, at some point, the number of sections that are unstalled will generate enough forces so that, as a consequence, the blade becomes even less stalled, and so on.

Accordingly, λ_{axial} (see equation 3.34) starts by being infinite and becomes smaller with time, during the first deceleration stage. When U_P becomes smaller than V_{tip} (which is equal to U_T at $x/R = 1$), i.e. when $\lambda_{axial} < 1$ the value of C_{d_R} (equation 3.33) commences to raise slightly, denoting a raise in the T produced by the rotor - this represents the beginning of the transition. This relation is also mentioned in the Kaman *Rotochute*'s analytical studies [12, 29], which is referred in section 2.3. The authors assumed the full transition between stalled and partially stalled blades to occur at $\lambda_{axial} = 0.5$ [12, 29], since below this value C_{d_R} starts to increase more rapidly with decreasing λ_{axial}, denoting an efficient operation (see figure 2.7 for clarity). Figure 3.17 displays the plot of C_{d_R} as a function of λ_{axial} obtained in the computational simulation, indicating a clear transition between the stalled and partially stalled (efficient) operations. As seen, for high values of λ_{axial}, C_{d_R} is nearly constant and low. For $0.5 < \lambda_{axial} < 1$, a slight increase of C_{d_R} is perceptible with the reduction of λ_{axial} and, for $\lambda_{axial} < 0.5$, the C_{d_R} value increases substantially, reaching eventually a maximum point. This is, thus, an additional way to confirm the rotor's operational transition. Moreover, this plot shows the same behaviour and tendency of the one in figure 2.7 [12, 29], and they can then be compared qualitatively.

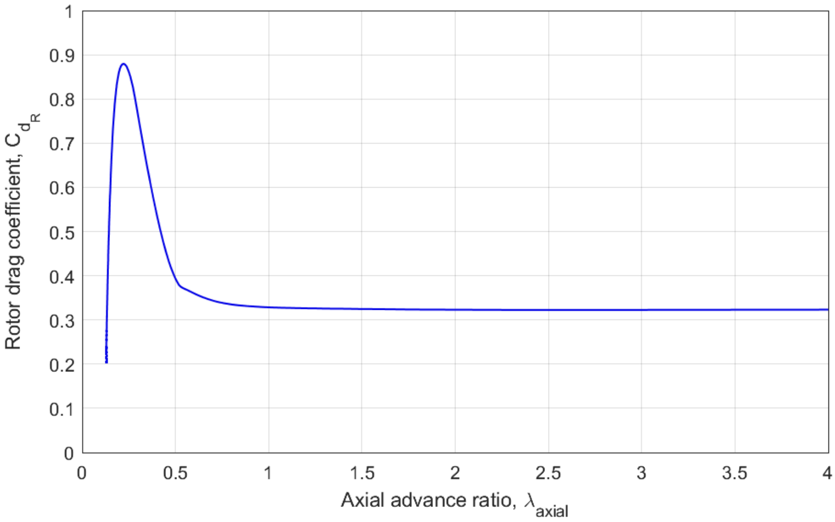

Figure 3.17: C_{d_R} variation with λ_{axial}, indicating a clear transition between the state of full stalled blades and partially stalled blades, noticeable by the sudden increase of C_{d_R}.

To confirm that this is, in fact, the point at which the rotor becomes more efficient, the evolution of C_{d_R} and λ_{axial} with t were investigated and are depicted in figure 3.18. As observed, C_{d_R} begins by having a low value of $C_{d_R} \approx 0.33$, while λ_{axial} starts by being enormous due to the low ω and decreases rapidly with its increase. At $t = 3.50\ s$, when a_v starts increasing once again, $\lambda_{axial} \approx 0.73$. At $t = 3.70\ s$, which coincides with the moment in which bigger variations of a_v begin to occur, $\lambda_{axial} \approx 0.51$. When λ_{axial} becomes lower than 0.5, as observed in the plots and as explained earlier, the raise of C_{d_R} becomes steeper. This moment is highlighted in the plots through a black line and represents the moment in which the blades become partially stalled, proving this phenomenon. Subsequently, the value of C_{d_R} eventually reaches a maximum of $C_{d_R} \approx 0.88$, and decreases afterwards until an equilibrium and approximately constant value of $C_{d_R} \approx 0.2$, while λ_{axial} stabilises at $\lambda_{axial} \approx 0.128$.

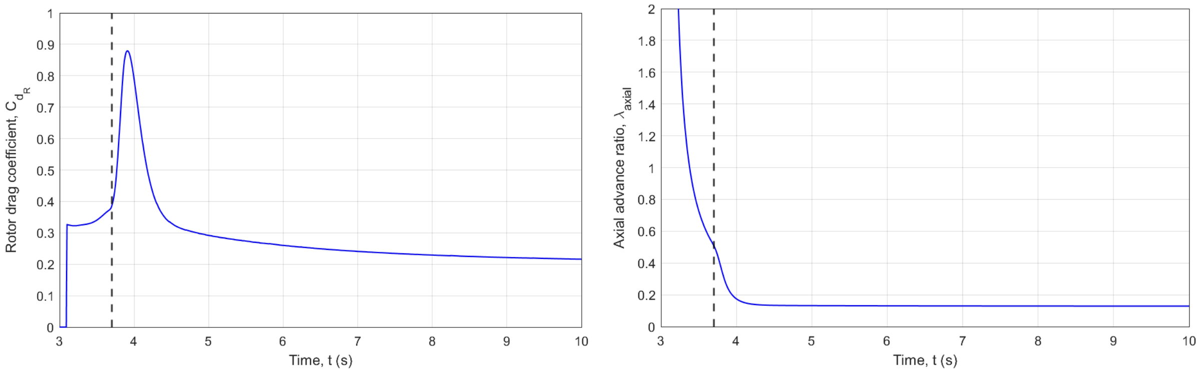

(a)

(b)

Figure 3.18: C_{d_R} (a) and λ_{axial} (b) evolution with t for the verification of the model.

From the definition of stall, one knows that an unstalled blade (or in this case, partially stalled) will generate greater forces, meaning higher efficiency when compared to a fully stalled one. Moreover, such transition results in greater T and Q, which consequently origin higher a_v and a_{ang}, decelerating the body and accelerating the rotor's rotation, respectively. Since T and Q are proportional to a_v and a_{ang}, respectively, it is expected that their plots behave accordingly, what is verified by the model. Figures 3.19(a) and 3.19(b) show, respectively, the evolution of T and Q of the rotor with t and can be compared with figures 3.15(a) and 3.15(b) as for its behaviour.

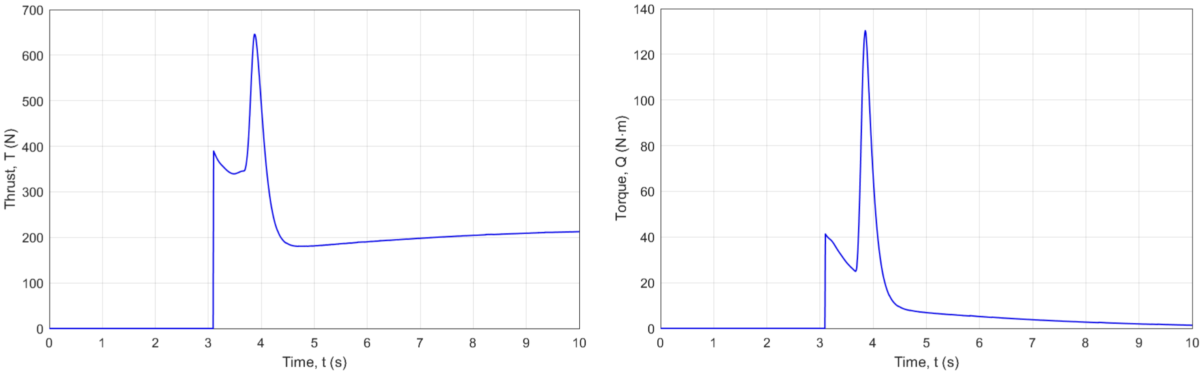

(a)

(b)

Figure 3.19: Evolution of T (a) and Q (b) with t for the verification of the model.

Following the second peak of accelerations, the system evolves to an equilibrium state, or autorotation. As predicted by theory (see section 3.1), an autorotative descent is characterised by $Q \approx 0$ and $T \approx W$, imposing then that $a_{ang} \approx 0$ and $a_v \approx 0$. Thus, the plots of a_{ang}, a_v and Q begin approaching 0, and T approaches a constant value which is approximately equal to W. It should be noted, though, that after the second peak of acceleration, a_v is negative for some seconds before reaching equilibrium (see figures 3.14(c) and 3.15(a)). This particularity is related to the θ selected since it is far from being an efficient choice. It will be seen later that it is possible to resolve this problem by changing θ.

The state of autorotation should, nevertheless, be studied in detail by inspecting the forces and moments along the blade. Figure 3.20 displays the spanwise distribution of dQ in the last moment of the simulation and thus in equilibrium. By looking into the plot of dQ, one is capable of identifying the rotor's different zones described previously in section 3.1.

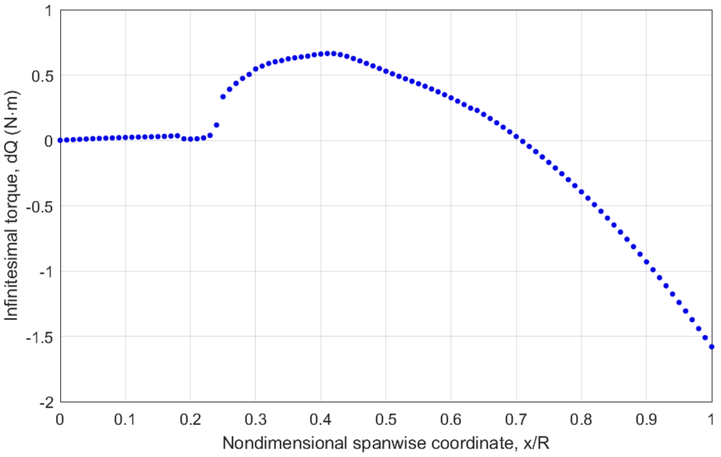

Figure 3.20: Spanwise distribution of the dQ of a blade's section in autorotation (equilibrium).

Until approximately $x/R = 0.23$, for 23% of the blade, there is no major change in the value of dQ, which remains in the order of $10^{-2}\ N \cdot m$. Thus, this is the stall zone. It is, however, positive, causing an acceleration of the rotor, contrarily to what was stated in section 3.1. The difference lies in the θ used in the simulation, since in the previous zone's description θ was considered to be positive. Nevertheless, due to the small values of dQ observed and their low contribution to the rotor's kinematics, the stall zone is considered to constitute around 23% of the rotor. In section 3.1 this zone was predicted to be 25% of the rotor [10], but such percentage is liable to change depending on θ. In addition, between $x/R = 0.24$ and $x/R = 0.70$ (47% of the blade), dQ increases substantially and then decreases again, having a maximum at $x/R = 0.42$. Since dQ is positive, this zone is the driving region, being responsible for the rotor's acceleration by absorbing power from the airstream to the rotor. This zone was predicted to be 25% to 70% of the rotor [10]. Finally, dQ becomes negative and keeps on decreasing for the rest of the blade's span. This remaining 30% of the rotor, as referred in section 3.1, belongs to the driven region, provoking a deceleration of the blades due to power dissipation. In this specific verification example, there is one and only one equilibrium point, between $x/R = 0.70$ and $x/R = 0.71$, and in which $dQ = 0\ N \cdot m$. By summing the contributions of each blade section and considering N_b, one gets $Q \approx -0.094\ N \cdot m$, which is close to the theoretical null value expected.

Accordingly, figure 3.21 depicts the spanwise distribution of dT in equilibrium conditions. As anticipated, the stall region does not produce a considerable amount of lift when compared to the other zones. In the driving zone a raise of dT is observed, and a maximum of $dT = 5.44\ N$ is recorded at $x/R = 0.42$. Still in the driving region, dT decreases and around the beginning of the driven region its value becomes negative, decreasing until the tip. At the end of the simulation, $W \approx 225.38\ N$, and a sum of the dT contributions gives a terminal $T \approx 221.74\ N$, representing an error of 1.6%.

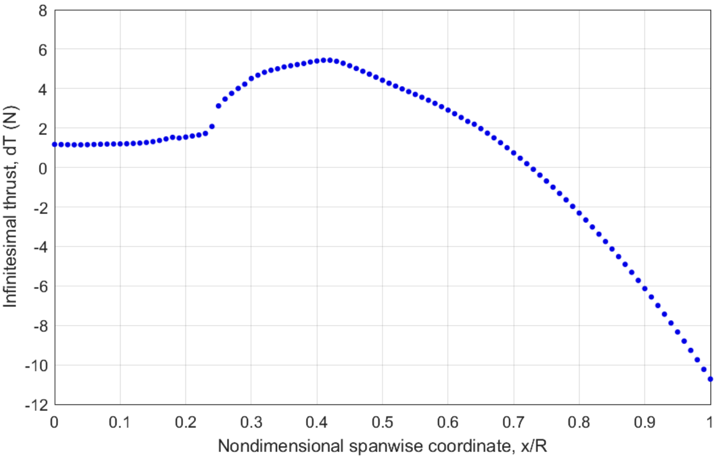

Figure 3.21: Spanwise distribution of the dT of a blade's section in autorotation (equilibrium).

It should be clarified that in figures 3.20 and 3.21, dQ and dT, respectively, are presented as points. However, they do not exactly correspond to a single point, but to a whole blade section of $dx = 0.01\ m$. Apart from that, from equations 3.11 and 3.12 it is seen that these values consider N_b, referring to the rotor and not exclusively to one blade.

It is important to note that the behaviour of dQ and dT can be compared with plots present in [19], which qualitatively confirm the functioning of the model. The values have different orders of magnitude simply because the rotor analysed in [19] was smaller than the one considered in this work.

With regard to the final values of Q and T, both present an acceptable proximity to the ones predicted by theory, although Q should be equal to $0\ N \cdot m$ and T should have the same value as W. The differences observed are the result of a number of factors.

First, as stated in section 3.2, variables such as ρ, Tp, μ and g vary with h and therefore with every dt of the simulation, provoking changes in the computation of the rotor's forces and never assuring that their values are completely constant with t. In fact, if the same simulation is run assuming these variables as being constant (for instance, $\rho = 1.225\ kg/m^3$, $Tp = 288.15\ K$ and $g = 9.81\ m/s^2$), the final force parameters are $T \approx 220.85\ N$ (error of 1.9%) and $Q \approx 5.68 \cdot 10^{-13}\ N \cdot m$, which for Q is much closer to the expected than the actual value observed. As for T, even though the error increased, it is reported that $a_v = -1.67 \cdot 10^{-13}\ m/s^2$, in comparison to the $a_v = 3.15 \cdot 10^{-2}\ m/s^2$ obtained in the actual simulation. Moreover, the usage of a limited amount of Re's, as well as the lack of experimental resources for the C_l and C_d plots with α, also contribute to these numerical errors. Additionally, even though the model already considers many features that bring it closer to the reality, there are still many unconsidered aspects, such as centrifugal forces, vortexes and losses in the blade's tip. Finally, $\theta = -10°$ is not the most efficient selection, as previously referred, and it will be seen further on that by increasing θ, these errors decrease and become even more negligible.

The stated issue results in v_v and ω not being exactly constant during the equilibrium operation, with both variables decreasing with t. These parameters' terminal values will not be addressed since this part of the work is more focused on the confirmation of the behaviour of the system rather than on obtaining a low terminal v_v.

The verification part of the work, with the assumptions adopted, is assumed to be a success, since the system performs accordingly to what is predicted by the theory, and even though it was not possible to compare it directly with literature studies, it is confirmed that the performance of the model follows the behaviour described by some of those studies. The model successfully results in the deceleration of the system, as well as in an approximate steady state autorotative descent, with the performance of the blade behaving close to what is seen empirically in autorotation. It should be also stated that, despite what was explained before regarding the impossibility of quantitatively comparing the performance of the system with the studies of [29] and [42], near terminal v_v's to the ones described in such studies were obtained by using the computational model, with the data available from the studies. This proves that the model is capable of achieving v_v's close to the ones reported and thus of provoking an adequate deceleration of the rocket's body, for roughly the same conditions.

3.2.3 Mesh Study

Another fundamental part of the model's analysis is a mesh study. The two mesh parameters of the model are the length of a blade element, dx, and the simulation's time step, dt.

It goes without saying that the lower these values are, the more trustworthy the simulation is. However, it is also noticeable that lower values of dx and dt translate into a higher computational time. For instance, if one was to assume a value of $dx = 0.01\ m$ instead of $dx = 0.1\ m$ with a blade of $R = 1\ m$, the computational time would increase roughly by 10 times, since the blade would be composed by 100 sections instead of 10 ($n_{sections} = R/dx$). This can result in a large computational time, which increases even further if one considers a blade with a greater R. Hence, a compromise must be made to balance the accuracy of results and the computational time of the simulations.

The mesh study consists in running the same simulation that was lastly described but varying the mesh parameters separately. Table 3.3 displays the mesh values utilised for this study. As observed, the dx analysis is conducted by dividing the $R = 1\ m$ blade into 100, 50, 20, 10, 5 and 2 sections, with $dt = 0.01\ s$. As for the dt variation study, the length of a blade element is kept at $dx = 0.1\ m$.

Table 3.3: Values of dx and dt selected to perform the mesh study.

Parameter	Values
$dx\ [m]$	$0.01; 0.02; 0.05; 0.1; 0.2; 0.5$
$dt\ [s]$	$0.001; 0.01; 0.05; 0.1$

It is significant to note two particularities in the dt study simulations. During the conception of the model, specifically the version that contains v_i, some problems were found regarding the convergence operation. At first, v_i starts by converging after 10 iterations, approximately, moving then to converging only in 2 or 3 iterations after some time steps. Nevertheless, whenever considerable variations occur, such as an acceleration peak that provokes large parameter variations over just a few numbers of time steps, the convergence is no longer attainable. The solution for this problem is to "refine" the mesh, by reducing dt. Therefore, even during an acceleration peak, a lower dt means lower parameter variations for each dt, enabling the convergence of v_i. From this conclusion, it is a requirement defined by the operation of the model that, whenever v_i is used in the simulation, a time step of $dt = 0.01\ s$ or lower should be used. For this reason, and since the current mesh study is intended to study several dt values, the model with v_i is not used for this specific study. Nonetheless, it is used for the dx variation study.

Besides this problem, it was observed that the model itself, even without considering v_i and its convergence process, is quite sensitive to big dt's before equilibrium is obtained, for the same reason pointed above. Thus, a maximum value of $dt = 0.1\ s$ was established. Above this value, the model is unable to properly proceed with its calculations, computing values that are not physically plausible.

Length of a blade's element, dx

Figure 3.22 displays the evolution of v_v, a_v, ω and a_{ang} with time for the referred dx values. It becomes clear that, the greater dx is, the more the values of the variables move away from each other – while the curves of $dx = 0.01\ m$ and $dx = 0.02\ m$ are even difficult to distinguish in the figure, the plot for $dx = 0.5\ m$ is completely detached from all the others. Another conclusion that can be taken from analysing the plots is that a higher dx tends to overpredict a_v which consequently results in a lower v_v, and to underpredict a_{ang} which gives a lower ω.

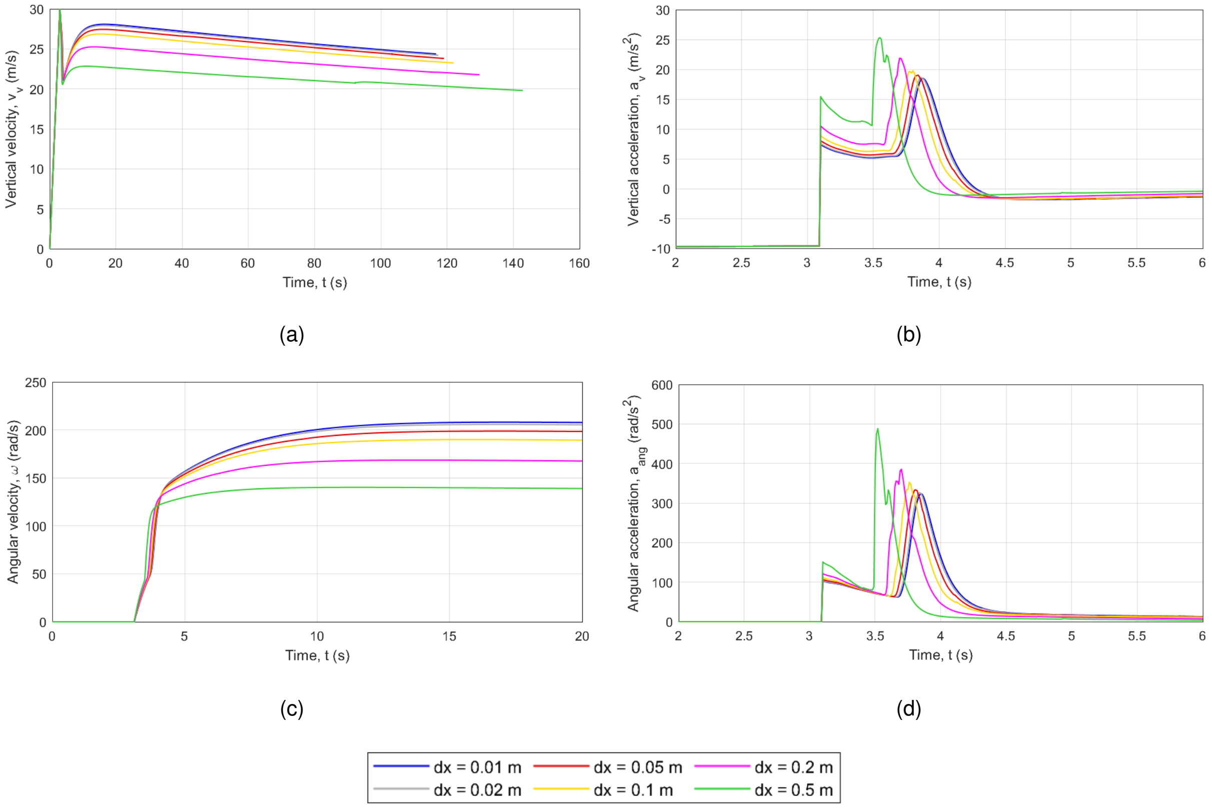

(a)

(b)

(c)

(d)

Figure 3.22: Evolutions of v_v (a), a_v (b), ω (c) and a_{ang} (d) with time for the different dx's studied.

A proper value of dx would be small enough not to jeopardise the results, but high enough not to compromise the computational time. Thus, it is necessary to address the change on the final values of the represented variables, for the several dx's tested. Considering that $dx = 0.01\ m$ is the most refined mesh and then the most reliable one, it is used as a reference for comparison.

Table 3.4 gives information about the terminal values of v_v, a_v and a_{ang} for the considered dx's and its comparison with the reference value. As observed, for v_v, until $dx = 0.1\ m$ the error remains below 5%, which is reasonable. As for a_v and a_{ang}, the errors propagate more, but by looking at the small values obtained, the differences are not very significant, with $dx = 0.1\ m$ presenting errors of 8.15% and 12.13%, respectively. Above $dx = 0.1\ m$, the errors become more significant. Thus, a maximum value of $dx = 0.1\ m$ is selected for this case, since it offers a satisfying performance of the system, without affecting the computational time excessively.

Table 3.4: Values and errors obtained for the final values of v_v, a_v and a_{ang} in the dx mesh study.

dx $[m]$	v_v $[m/s]$		a_v $[m/s^2]$		a_{ang} $[rad/s^2]$	
	Value	Error [%]	Value	Error [%]	Value	Error [%]
0.01	24.357	-	0.032	-	-0.233	-
0.02	24.198	0.65	0.030	6.21	-0.215	7.67
0.05	23.796	2.30	0.031	2.46	-0.223	4.30
0.1	23.235	4.61	0.029	8.15	-0.205	12.13
0.2	21.758	10.67	0.026	18.79	-0.171	26.60
0.5	19.789	18.76	0.021	32.92	-0.130	44.28

Time step, dt

As for dt, the studied values presented such small differences between each other that it is not possible to observe them graphically. Table 3.5 demonstrates such observations, with $dt = 0.001\ s$ being the reference time step. Remember that a maximum of $dt = 0.1\ s$ is a requirement. As observed, the relative errors computed are extremely low, which means that the usage of $dt = 0.1\ s$ is viable. It is important to note, however, than when using a model that considers v_i, a value of $dt = 0.01\ s$ or lower is required, as referred before.

Table 3.5: Values and errors obtained for the final values of v_v, a_v and a_{ang} in the dt mesh study.

dt $[s]$	v_v $[m/s]$		a_v $[m/s^2]$		a_{ang} $[rad/s^2]$	
	Value	Error [%]	Value	Error [%]	Value	Error [%]
0.001	21.959	-	0.026	-	-0.192	-
0.01	21.959	$1.89 \cdot 10^{-4}$	0.026	$2.72 \cdot 10^{-3}$	-0.192	$2.88 \cdot 10^{-3}$
0.05	21.958	$4.70 \cdot 10^{-3}$	0.026	$1.15 \cdot 10^{-2}$	-0.192	$1.31 \cdot 10^{-2}$
0.1	21.958	$5.26 \cdot 10^{-3}$	0.026	$2.38 \cdot 10^{-3}$	-0.192	$3.16 \cdot 10^{-3}$

3.3 Genetic Optimisation

Being a model that simulates the operation of descent and recovery of the first stage of a rocket, the developed computational model also possesses the capability of integrating an optimisation algorithm, which allows to analyse different design combinations to find an optimised solution that assures the best performance of the system.

Optimisation is defined by Martins and Ning [60] as the process that finds the best possible solution by altering variables that can be controlled, frequently subject to constraints. These variables are named design variables and, if possible, should be defined by its lower and upper bounds (bound constraints), which are based on the problem's conditions and physical limits [60]. These variables can take integer or non-integer values, depending on the problem. As for the solution, the objective function is a variable that, by being minimised, determines whether one design is better than other [60].

For this matter, a genetic algorithm (GA) is used. A GA is based on the evolutionary process of natural selection. Briefly, the GA starts with an initial population (several combinations of design variables), each population being composed by chromosomes (a design combination), while a chromosome possesses several genes (a design variable). From natural selection, in a generation (iteration, in a GA), some members of the population that give out better results are more likely to survive and to reproduce, being selected as parents. This is called selection. The parents will then exchange genetic material between chromosomes, generating the offspring for the next generation. This is called crossover. Finally, mutations can also happen in the genetic evolution, with some design variables' values being randomly switched. Following this, and with a newly generated population, with the same number of individuals as the previous one, the whole process restarts, for several generations [60]. Such method guarantees not only the diversity of the population, but also the minimisation of the objective function with successive generations. This means that the best point in the final population approaches an optimal solution.

Chapter 4

Computational Experiments

In this chapter, a real situation will be addressed, in order to better comprehend the performance of the rotary wing recovery system, as well as its feasibility depending on the mission requirements.

The chapter is organised in the following manner: first, the rocket and its initial conditions are described. Secondly, parametric studies and its results and discussion are unfolded to assess the influence of each rotor design variable. Finally, the design optimisation and respective solution are presented, with the demonstration of a flare manoeuvre.

4.1 *Baltasar* Sounding Rocket

The selected scenario is the recovery of the sounding rocket *Baltasar* (see figure 4.1), developed by the Rocket Experiment Division (RED) [61], a team of students from Instituto Superior Técnico, whose goal is the design, building and launch of model-rockets for international university competitions. Throughout its experience, the team has always resorted to parachutes as a means of safely recovering its rockets, using a drogue and a main parachute, with the objective of reaching a touchdown velocity of around $5.95\ m/s$.

Figure 4.1: The sounding rocket *Baltasar*. Image provided by the RED team.

Thus, *Baltasar* represents an interesting opportunity to assess the usage of the rotary wing recovery system as an alternative to the parachute, for two main reasons. First, being a model-rocket that reaches an altitude of about $3,000\ m$ at reasonably low velocities, it is a simple enough problem for a proof of concept. Secondly, *Baltasar* was designed for a specific competition, having certain requirements that must be complied with. Such requirements, such as the apogee at about $3,000\ m$ and the recovery system's deployment at a descent velocity of approximately $30\ m/s$, makes it possible to fix these parameters as initial conditions. The initial conditions considered are available in table 4.1 and were attentively provided by the team.

Table 4.1: Initial fixed conditions for the simulations run for the RED's rocket, *Baltasar*.

m_{stage} $[kg]$	Lt_{stage} $[m]$	Dm_{stage} $[m]$	h_0 $[m]$	t_{deploy} $[s]$
19	3	0.133	$3,000$	3.09

Considering the freefall described in section 3.2, a drop of $t_{deploy} = 3.09\ s$ increases the vertical velocity of the rocket to the required value, $v_{v_{deploy}} \approx 30\ m/s$, at which the deploy of the blades is carried out. At this moment, the system has an altitude of $h_{deploy} \approx 2,976\ m$.

4.2 Parametric Study

Considering what was discussed in section 4.1, fixing the initial conditions of h_0 and $v_{v_{deploy}}$ leaves room to fully focus on studying the recovery system itself, by means of a design parametric study.

On that account, this study involves the analysis of the following design parameters: blade's span, R, rotor's number of blades, N_b, and blade's collective pitch, θ. It consists in investigating how the system's performance varies with the change of each design variable, while the other variables remain constant, with an emphasis on minimising the terminal v_v at touchdown and reaching, eventually, a design that can maximise the system's efficiency. Variations of c are not studied since no references are found in the literature regarding its importance and it is the least likely to provoke major changes.

Table 4.2 shows the simulation parameters of these simulations, in which the v_i model was used. The values of dx and dt are based on the results obtained in the mesh studies of subsection 3.2.3.

Table 4.2: Parameters of the simulation for the parametric study.

dx $[m]$	dt $[s]$	v_i convergence criteria
0.1	0.01	10^{-4}

4.2.1 Variation of R

Regarding variations of R, which are observable in table 4.3, constraints should be imposed. A maximum limit of $R = 3\ m$ ($\sigma \approx 0.054$) is defined taking into account that the rocket's length is $Lt_{stage} = 3\ m$. Obviously, this value is exaggerated and not realistic and is used as a matter of studying not only efficient situations, but also inefficient ones - as known, $m_{recovery}$ has higher variations as R increases, meaning that a too high R value would result in excessive mass additions. Moreover, an extremely small minimum value of $R = 0.4\ m$ ($\sigma \approx 0.406$) is selected as well. The remaining R values are chosen based on commonly used values of σ from the literature [29, 39] (remember from equation 3.16 that σ decreases with increasing R). The correspondent σ values are also present in table 4.3.

Table 4.3: Rotor's design parameters for the R variation study.

N_b	$R\ [m]$	$c\ [m]$	$\theta\ [^\circ]$	σ
3	$0.4; 0.8; 1; 1.1;$ $1.4; 1.6; 2; 3$	0.17	-5	$0.406; 0.203; 0.162; 0.147;$ $0.116; 0.101; 0.081; 0.054$

Figures 4.2 and 4.3 show the variation of v_v and a_v for the several studied R's of the blade. Most of the plots follow the same tendency, showing lower terminal v_v's for higher R's, with big differences between each other, though. The cases of $R = 0.4\ m$ and $R = 3\ m$ are especially different.

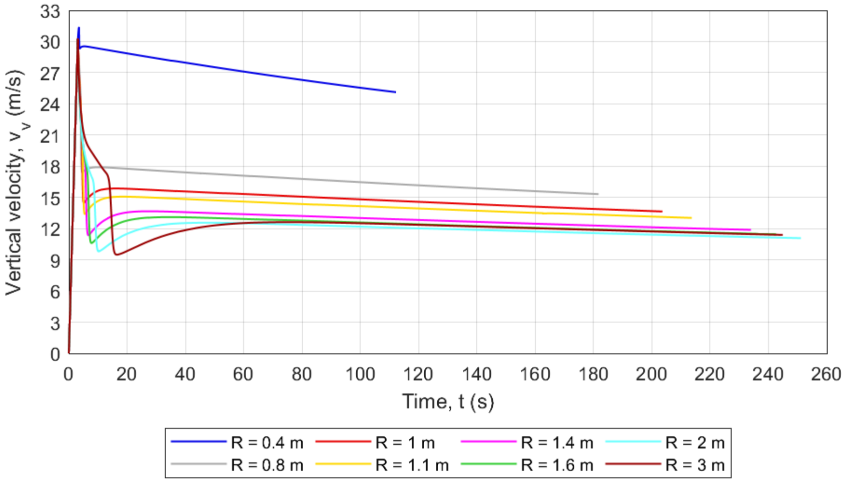

Figure 4.2: Evolution of v_v with t for the several R's studied.

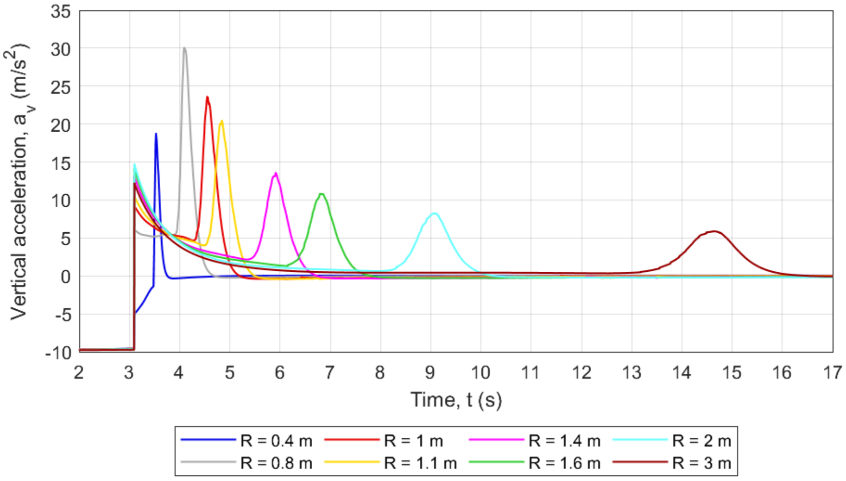

Figure 4.3: Evolution of a_v with t during the first seconds of the simulation, for the several R's studied.

As expected, $R = 0.4\ m$ does not provide an adequate deceleration and the system even increases its v_v during some seconds following the rotor's deploy. As for $R = 3\ m$, the v_v plot of figure 4.2 shows that the terminal v_v is even greater than the one achieved for $R = 2\ m$. These two exceptions are addressed here in order to understand that there are also inefficient R's, and will be commented later.

Considering what was just stated, the following analysis does not refer to the cases of $R = 0.4\ m$ and $R = 3\ m$. By looking at both figures, it becomes clear that the increase of R has several effects on the behaviour of a_v, which reflect in v_v. Firstly, it is observed that the first peak of a_v becomes higher with increasing R (it is difficult to observe such conclusion in figure 4.3 because the plots are on top of one another), since the blade acting as a flat drag plate generates higher T if it has a greater acting area. Secondly and contrarily, it is perceptible that the second peak of a_v becomes smaller with R as for maximum value but, at the same time, also takes place later and happens during a longer period of time. For example, if for $R = 0.8\ m$ there is a maximum of $a_v \approx 30.0\ m/s^2$ and the peak lasts for $0.5\ s$ until reaching a value close to $0\ m/s^2$, for $R = 2\ m$ the maximum is $a_v \approx 8.2\ m/s^2$ but the peak takes around $2\ s$. The fact that the second peak of a_v is "delayed" with increasing R means that a_v is positive for a longer period of time because the transition between fully stalled blades and partially stalled blades is longer. Moreover, and even though the second peak becomes lower, it can be seen through figure 4.2 that this phenomenon results in a greater deceleration and consequently on a lower v_v. Another noticeable fact is that the differences between the final v_v's of the rocket start by being considerable (for example between $R = 0.8\ m$ and $R = 1\ m$), but as R increases such differences become slighter and, at some point, negligible. Thus, the terminal v_v appears to be converging to a certain value as R increases.

By looking with detail at the plot of $R = 0.4\ m$, the first a_v peak is not enough to start the deceleration of the rocket, only doing so when the second peak occurs. In addition, this second peak is lower than the ones on some of the other plots. This proves that this design is not efficient since the blades do not have enough R to generate the required forces.

In the same manner, the first a_v peak for $R = 3\ m$ is not as high as some of the other design's, oppositely to what would be expected, and even though the second peak follows the same behaviour described above, it is not enough to decelerate the system to a lower terminal velocity than the one of $R = 2\ m$. This can be explained by the high $m_{recovery}$ associated with this design, which is approximately 52% of the rocket's gross weight. In fact, the T produced by the blades in this case is much higher than in the $R = 2\ m$ rotor, but the excessive m (total mass) does not allow for an effective deceleration (see equation 3.29). This is also related to the approach chosen for the calculation of $m_{recovery}$ (in equation 3.18), in which this value evolves dramatically with increasing R. By this, it is understood that from a certain R, the performance of the system becomes prejudicial due to the high m, instead of being improved. Concluding, there must be a compromise that balances such situation.

One can resort to the same logic to analyse the plots of ω and a_{ang}, present in figures 4.4 and 4.5, respectively. Figure 4.6 displays the evolution of a_{ang} with more detail. Equation 3.32 implies that I_{rotor} increases with R and m_{rotor}. Thus, from equation 3.30 it is understandable that a higher R will result in a lower a_{ang} and on a smaller variation of ω, even though it is observed that Q increases with R. For this reason, the terminal value of ω is lower with increasing R. It is concluded, then, that a successively higher R allows the system to find its steady state operation at lower ω's, what can be advantageous not to induce blade's overspeeding.

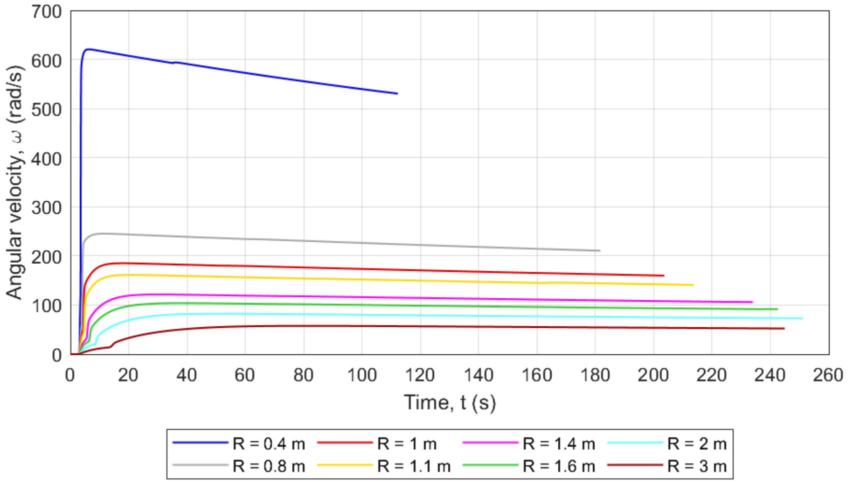

Figure 4.4: Evolution of ω with t for the several R's studied.

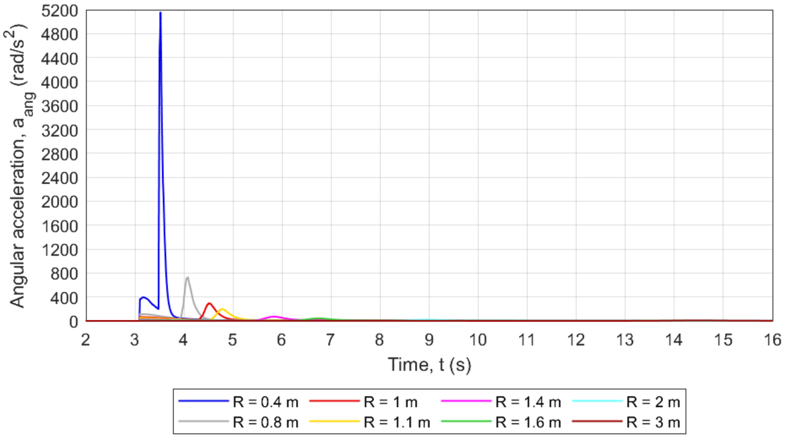

Figure 4.5: Evolution of a_{ang} with t during the first seconds of the simulation, for the several R's studied.

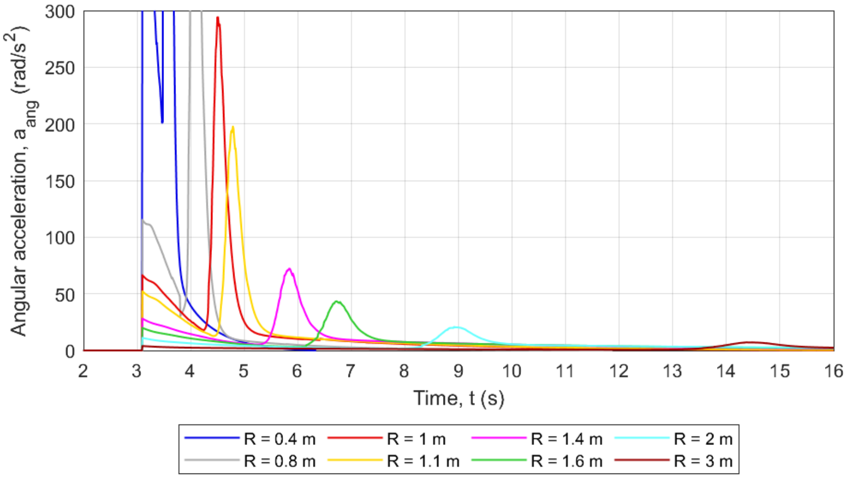

Figure 4.6: More detailed evolution of a_{ang} with t, for the several R's studied.

Regarding the terminal v_v, table 4.4 addresses not only its value but also the percentage decrease from the initial $v_{v_{deploy}} \approx 30\ m/s$. As seen, v_v decreases with R, but the variation between designs becomes progressively smaller. Finally, for $R = 3\ m$ the value increases in relation to $R = 2\ m$. Thus, for this specific case, $R = 1.4\ m$, $R = 1.6\ m$ and $R = 2\ m$ would be the best values. However, due to the proximity between the v_v of such designs, one can focus on minimising $m_{recovery}$ or on the rotor's stowage. For this reason, $R = 1.4\ m$ would prove to be a reasonable choice. Another important conclusion taken from this study is that the problem noted on the verification study, in which Q is not exactly equal to $0\ N \cdot m$ and T to W, tends to become less relevant with the increase of R, in general. This is denoted by a slighter slope on the curves of v_v and ω, constituting a more efficient operation.

Table 4.4: Values of the terminal v_v for each R and its percentage decrease from $v_{v_{deploy}}$.

$R\ [m]$	$v_v\ [m/s]$	Decrease [%]
0.4	25.12	16.7
0.8	15.32	49.2
1	13.65	54.8
1.1	13.03	56.8
1.4	11.88	60.6
1.6	11.46	62.0
2	11.08	63.3
3	11.40	62.2

4.2.2 Variation of N_b

In the same manner, N_b is studied considering the most usual values in the literature and in helicopters in general. The values are in table 4.5. Remember that $m_{recovery}$ is dependent on N_b, so it is interesting to address whether increasing N_b will always favour the performance of the system. Apart from this, it is important to remember from equation 3.16 that σ increases with increasing N_b. Hence, this study can also be considered a σ variation analysis and the σ values studied are present in the table, corresponding approximately to usual values present in the literature [29, 39].

Table 4.5: Rotor's design parameters for the N_b variation study.

N_b	$R\ [m]$	$c\ [m]$	θ [°]	σ
$2; 3; 4; 5$	1	0.17	-5	$0.108; 0.162; 0.197; 0.271$

The variations of v_v and a_v are displayed respectively in figures 4.7 and 4.8 and, as expected, the deceleration provoked by the rotor is greater with a higher N_b – increasing N_b values result in lower

v_v's. Similarly to the previous parametric study, as N_b raises the differences between the terminal v_v's become slighter and this value appears to be converging. While the difference between $N_b = 2$ and $N_b = 3$ is of approximately $1.97\ m/s$, between $N_b = 4$ and $N_b = 5$ such difference drops to roughly $0.60\ m/s$.

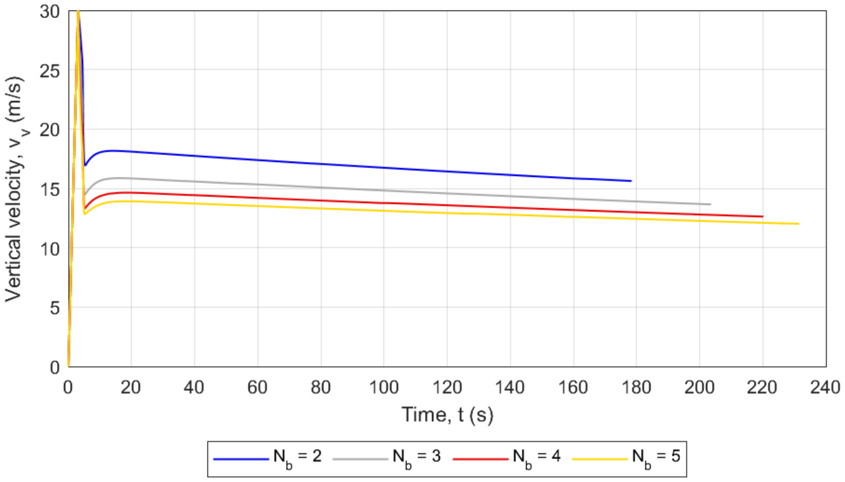

Figure 4.7: Evolution of v_v with t for the several N_b's studied.

As for a_v, figure 4.8 shows that a higher N_b results in a greater first peak, with considerable differences. First of all, more blades will result in a higher area that assists on the fully stalled blades to produce more T, explaining the first peak. Furthermore, it is observed that the second peak of a_v decreases in value and generally takes place later with increasing N_b, just like in the previous study. The only exception is on the second peak of $N_b = 2$, which actually happens after the one of $N_b = 3$. This can be explained by a later convergence of v_i that was observed in such simulation, resulting in less trustworthy results (some small acceleration peaks can be seen on the plot of $N_b = 2$, around $t = 4\ s$). Nevertheless, the substantial differences registered in the first a_v peak are enough for the velocities to be progressively lower with N_b. It should be noted that the rotor's T showed the same behaviour as a_v.

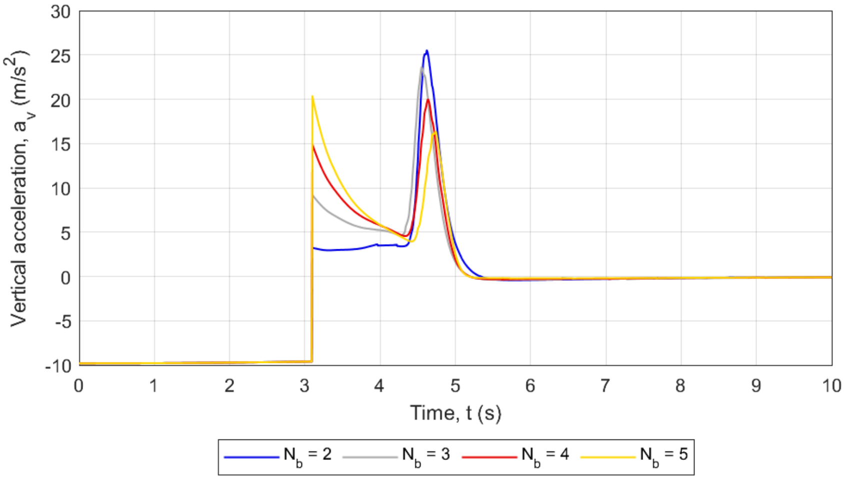

Figure 4.8: Evolution of a_v with t during the first seconds of the simulation, for the several N_b's studied.

This means, then, that in this specific case the weight alterations provoked by adding blades are not prejudicial for the system. In fact, the percentage of $m_{recovery}$ only varies here between 15.7% and 20% of the gross weight. Thus, the deceleration induced by a rotor with more blades compensates the weight penalties. This might not always be the case, though, since for higher N_b's the weight would probably be excessive – just like on the R variation study. Apart from this, if this study were be run with higher values of R, the adding of extra blades could have been proved to be prejudicial.

In addition, the use of a higher N_b brings up other issues, such as the stowage of the blades. Assume that in *Baltasar* the blades, when not yet deployed, rest along the length of the rocket's body, due to the lack of space for storage inside the payload bay. This means that $c \cdot N_b$ must not overcome the perimeter of the rocket's body, $Dm_{stage}\pi \approx 0.53\ m$. Depending on the choice of c, the value of N_b might not assure this condition. For example, in this case $c = 0.17\ m$, so $N_b = 4$ and $N_b = 5$ are unlikely to be feasible in reality. However, the objective of this study is to analyse only the variation of one parameter and understand such variation (even if some values are not realistic), so this issue is neglected for now.

As for ω and a_{ang}, in figures 4.9 and 4.10, respectively, the higher N_b is, the lower is a_{ang} and consequently ω. For $N_b = 2$, the rotor requires a high ω in order to reach a deceleration that is, at least, comparable to the one achieved with $N_b = 5$. The successively lower a_{ang} values are explained by not only an increasing I_{rotor}, but also because the rotor's Q itself decreases with N_b, contrarily to what was seen on the previous parametric study with variations of R. Moreover, it is noticeable that the plots become close to one another with increasing N_b, in the same way as the plots of v_v and a_v.

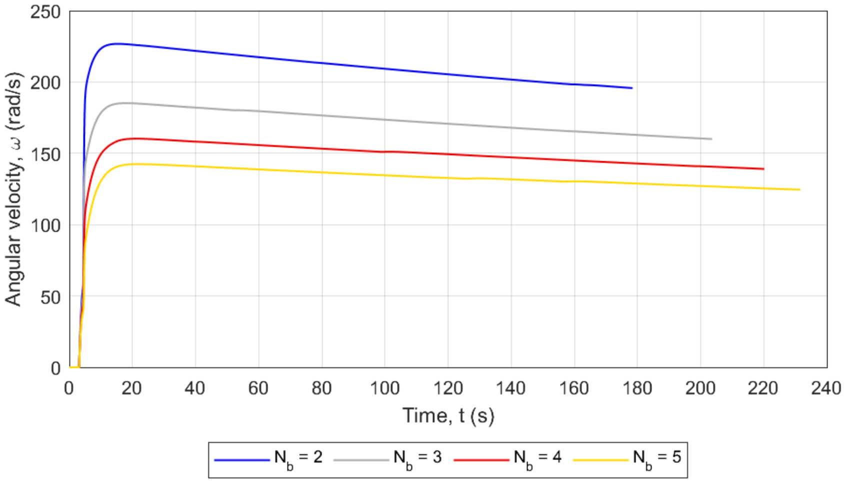

Figure 4.9: Evolution of ω with t for the several N_b's studied.

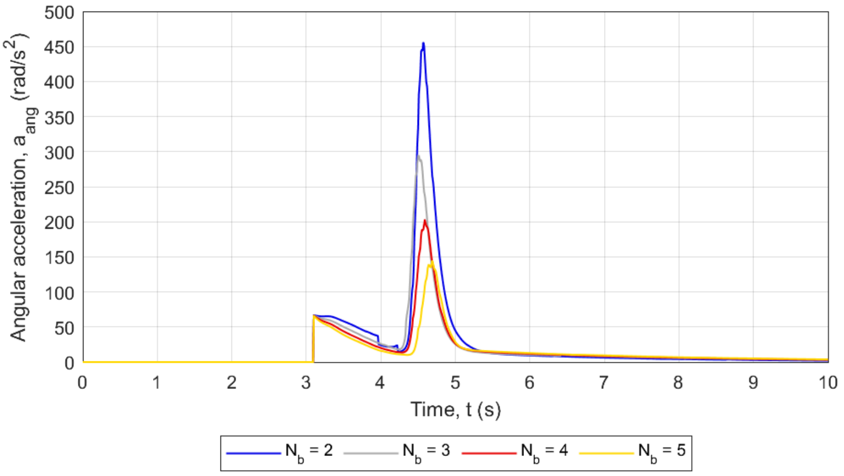

Figure 4.10: Evolution of a_{ang} with t during the first seconds of the simulation, for the several N_b's studied.

It was stated above that an increase of N_b can also be interpreted as an increase of σ. It is important, then, to address how C_{d_R} evolves with λ_{axial} for different values of N_b, or σ. As observed in figure 4.11, N_b (or σ) is nearly proportional to C_{d_R} through the whole figure, contrarily to the predicted by the Kaman *Rotochute* studies (see figure 2.7) [12, 29], in which the proportionality was only stated for the region in which the blades are fully stalled ($\lambda_{axial} > 0.5$). However, it was predicted that the maximum value of C_{d_R} would increase with higher σ, as proved by figure 4.11. By being proportional for most of the plot, this means that, as seen in the figure, the maximum values of C_{d_R} are extremely different for the different simulations, which demonstrates a difference from what was expected from the Kaman studies [12, 29]. Nevertheless, the λ_{axial} for which the maximum C_{d_R} occurs is higher with increasing N_b, something that was predicted on such studies [12, 29].

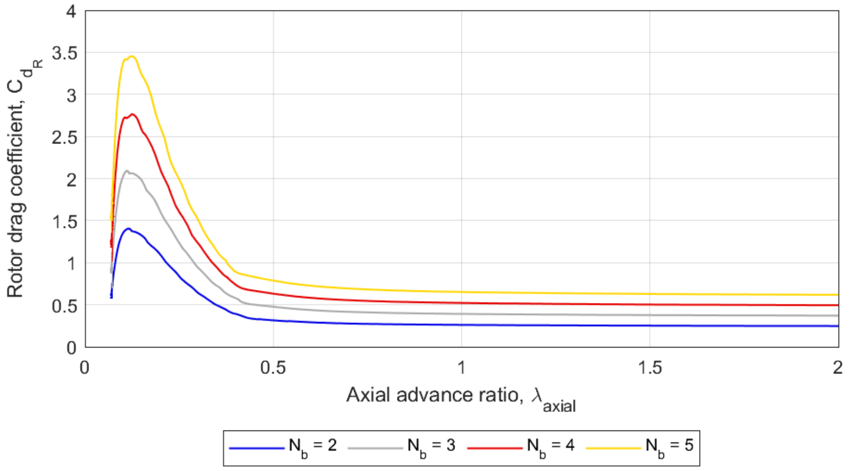

Figure 4.11: C_{d_R} variation with λ_{axial} for the several N_b's studied.

Finally, the values of the terminal v_v are summarised in table 4.6, along with its comparison with $v_{v_{deploy}}$. As seen, the differences become smaller with increasing N_b. Furthermore, a choice that would guarantee a balance between the weight penalty and the system's performance would be, for instance,

$N_b = 3$ or $N_b = 4$, which are the usual selections present in the literature. It should be also stated that the issue of the final values of Q and T tends to become less significant with increasing N_b.

Table 4.6: Values of the terminal v_v for each N_b and its percentage decrease from $v_{v_{deploy}}$.

N_b	v_v $[m/s]$	Decrease [%]
2	15.62	48.1
3	13.65	54.7
4	12.62	58.1
5	12.02	60.1

4.2.3 Variation of θ

Finally, the θ angle variation is studied, since this is one of the parameters that most influences the rotor's performance. Apart from the θ values of table 4.7, other θ's are also considered in order to plot certain graphs, which are addressed further on this document.

Table 4.7: Rotor's design parameters for the θ variation study.

N_b	$R\,[m]$	$c\,[m]$	$\theta\,[^\circ]$	σ
3	1	0.17	$-10; -5; -4; -3; -2.9; -2.8; -2$	0.162

This angle was discussed in chapters 2 and 3 to be the most defining parameter of the performance of an autorotative descent. It was mentioned in section 3.1 that, by changing θ, it is possible to alter α. This varies the direction of the resultant force on the blades and consequently the values of T and Q, what changes the size of the driving, driven and stall regions of the blade (see figures 3.3 and 3.4). Moreover, the control of such angle allows for the autorotative state to be maintained while assuring that the blades will not overspeed, or the opposite.

Figures 4.12 and 4.13 present the evolution of v_v and a_v with t for the several θ's. Note that in this study the behaviour of T is exactly like the one of a_v, since there are no changes on the rotor's dimensions or mass. As discussed before, all the values of θ are negative to induce a rotation of the blades on the right direction. From figure 3.5, one can conclude that a higher θ (less negative) has a higher T and a lower Q in comparison to a lower θ. For this reason, it is observed that the first a_v peak, even though not very different, increases with θ. After this point, the changes start to be plenty.

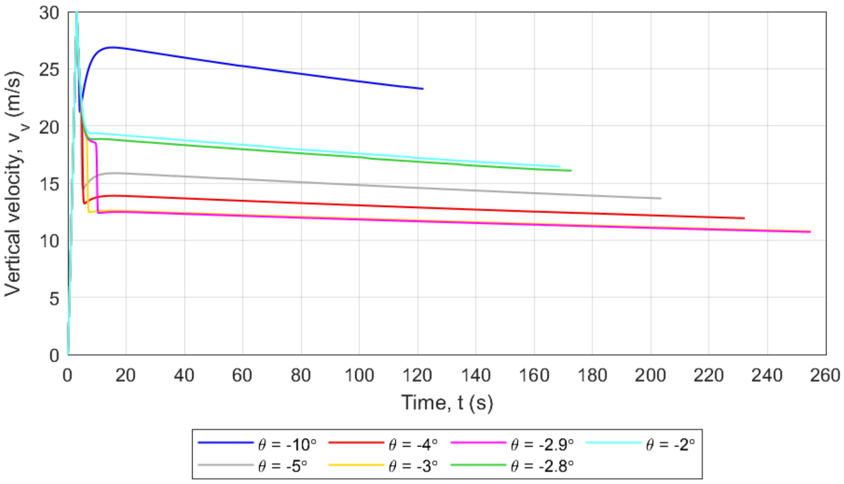

Figure 4.12: Evolution of v_v with t for the several θ's studied.

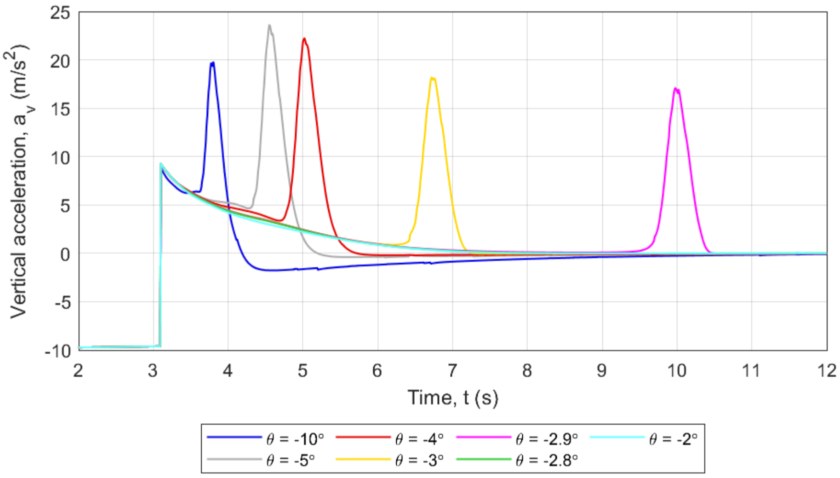

Figure 4.13: Evolution of a_v with t during the first seconds of the simulation, for the several θ's studied.

The case of $\theta = -10°$ was analysed in subsection 3.2.2 and was addressed as being far from efficient. This happens mainly because between the first and second peaks there is a period in which a_v is negative, which adversely increases v_v. The same is observed for $\theta = -5°$, however at a rather smaller magnitude. This proves that as θ increases this problem is solved.

Regarding the second a_v peak, it can be seen that $\theta = -2.8°$ and $\theta = -2°$ do not present one. Even though their first peaks are the highest, the blades are not capable of generating enough Q for ϕ, and consequently α, to decrease significantly, which means that the blades remain fully stalled, never overcoming this state. It is curious, though, to observe that the results obtained with a fully stalled blade for these two cases are actually better than the ones for $\theta = -10°$, regarding the terminal v_v. Another interesting remark is the fact that all the other plots follow approximately the curves of $\theta = -2.8°$ and $\theta = -2°$ while the blades are fully stalled, i.e., before the respective a_v peaks (see figure 4.13). As for the remaining angles, the second peak is generally smaller with an increasing θ (except for $\theta = -10°$) and occurs later, just as seen on the previous parametric studies - this results in a lower terminal v_v.

The evolution of v_v is displayed in figure 4.14 with more detail, for the first seconds of the simulation. It is clearly seen that the plots follow the same curves as the ones for $\theta = -2.8°$ and $\theta = -2°$, successively changing its behaviour and converging to a terminal value, what happens later with the raise of θ. For example, one can observe that the second drop of velocity for $\theta = -2.9°$ takes place approximately $2.5\ s$ later than the one for $\theta = -3°$, and during this time v_v remains approximately constant. This means that the rotor "delays" the transition from fully stalled blades to partially stalled blades.

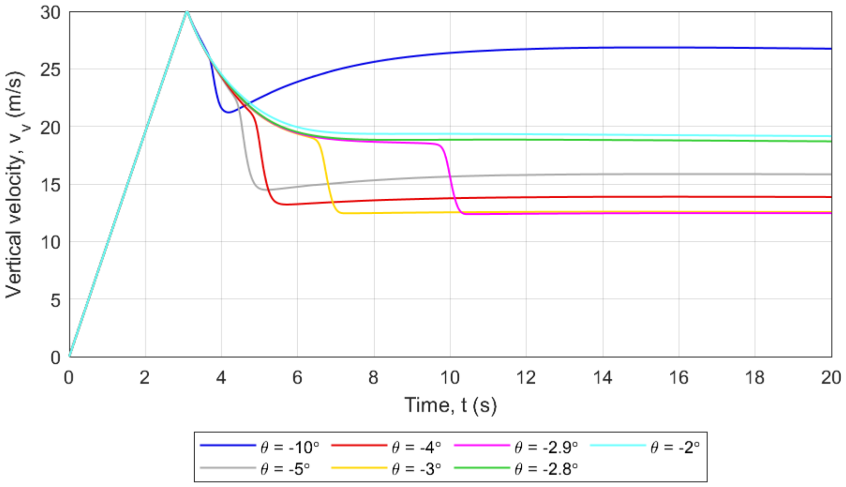

Figure 4.14: Evolution of v_v with t during the first seconds of the simulation, for the several θ's studied.

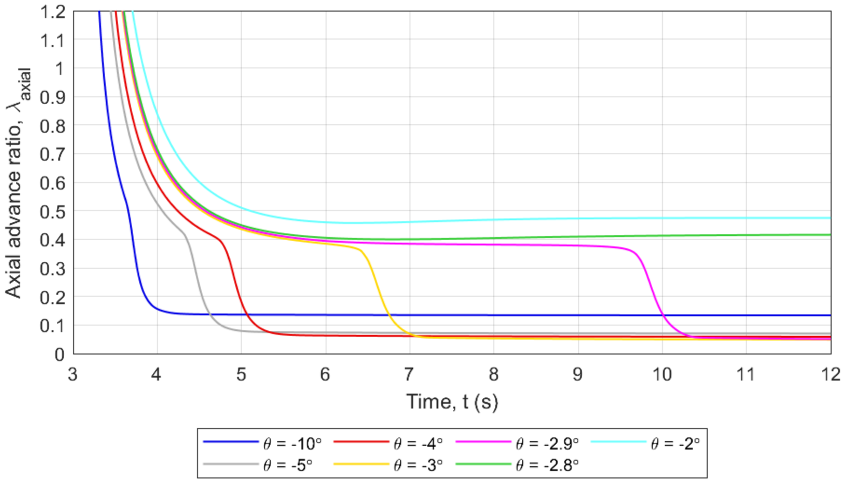

Figure 4.15: Evolution of λ_{axial} with t during the first seconds of the simulation, for the several θ's studied.

As a matter of fact, if the evolution of λ_{axial} with t is addressed closely (figure 4.15), it is observed that this value drops at $\lambda_{axial} \approx 0.4$, point at which the transition occurs and the peaks begin. However, the "delay" is quite clear for $\theta = -3°$ and $\theta = -2.9°$, in which λ_{axial} maintains the constant value of $\lambda_{axial} \approx 0.4$ for some seconds, dropping afterwards.

As for ω and a_{ang}, present respectively in figures 4.16 and 4.17, $\theta = -10°$ has higher first and second peaks of a_{ang} which result in a higher ω, in the first seconds of the simulation. These peaks tend to decrease with increasing θ, since this reduces the generation of Q (which varies in the same manner as a_{ang}, since there are no variations on I_{rotor}), resulting consequently in lower ω's. On the other side, $\theta = -2.8°$ and $\theta = -2°$ present the lowest first peaks and no second peak, what results in low values of ω.

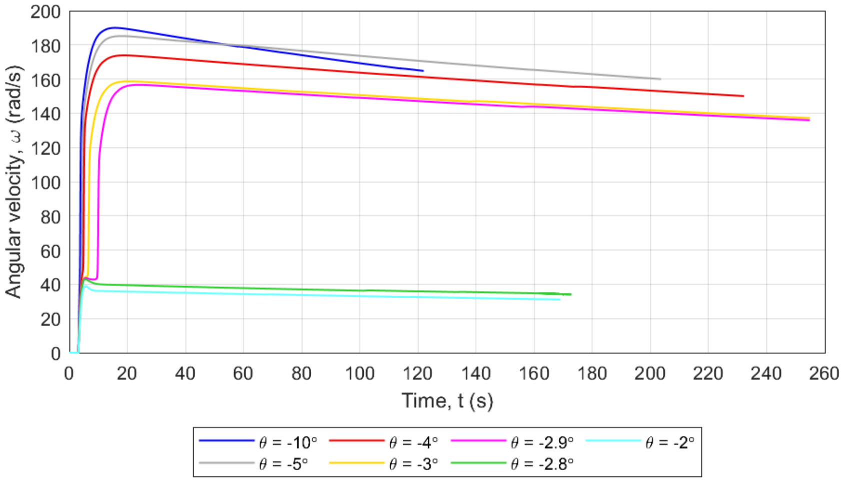

Figure 4.16: Evolution of ω with t for the several θ's studied.

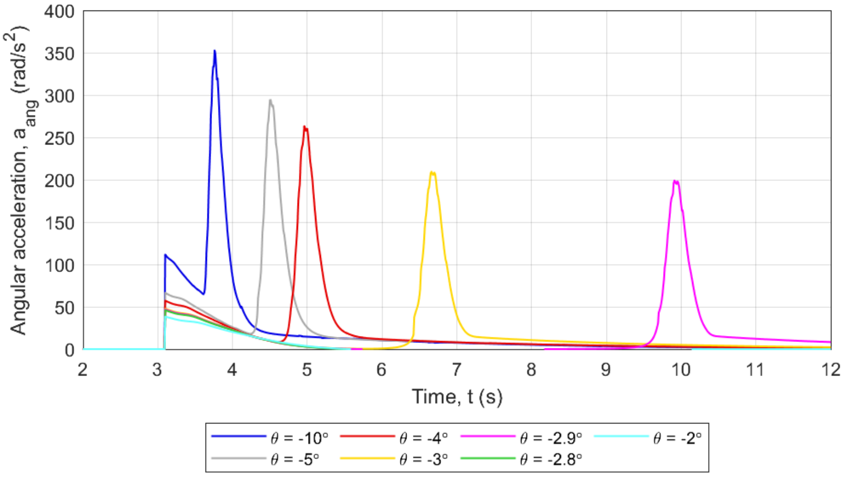

Figure 4.17: Evolution of a_{ang} with t during the first seconds of the simulation, for the several θ's studied.

To better comprehend the changes produced by the variation of θ, an analysis should be made within the blade. Figure 4.18 shows the spanwise distribution of α for $\theta = -10°$, $\theta = -4°$ and $\theta = -2°$, in the end of the respective simulations (equilibrium). The case of $\theta = -10°$ was discussed to result in approximately 30% of the blade being stalled, as seen in subsection 3.2.2. For $\theta = -2°$, the minimum α achieved is $\alpha \approx 23.0°$, which is still higher than α_{crit} for the respective Re number. This allows to conclude that the whole blade is indeed stalled. Finally, for $\theta = -4°$, less than 20% of the blade is stalled, which represents a smaller value than the one for $\theta = -10°$. Thus, it is possible to conclude that a higher θ results in a smaller percentage of the blade being stalled (for efficient θ values that induce a partially stalled operation). In addition, most of the plot has lower α values in comparison to the plot of $\theta = -10°$. For $x/R > 0.8$ this tendency is inverted, but α and consequently C_l become negative (and C_d

increases) for $\theta = -10°$, which is prejudicial, while for $\theta = -4°$ this is not verified. Thus, it is proved that $\theta = -4°$ attains the best performance out of these three values. A likewise plot from the one in figure 4.18 is present in [19], with two different values of θ showing the same behaviour as for their differences. Such plot serves as a qualitative comparison for the confirmation of the model's functioning.

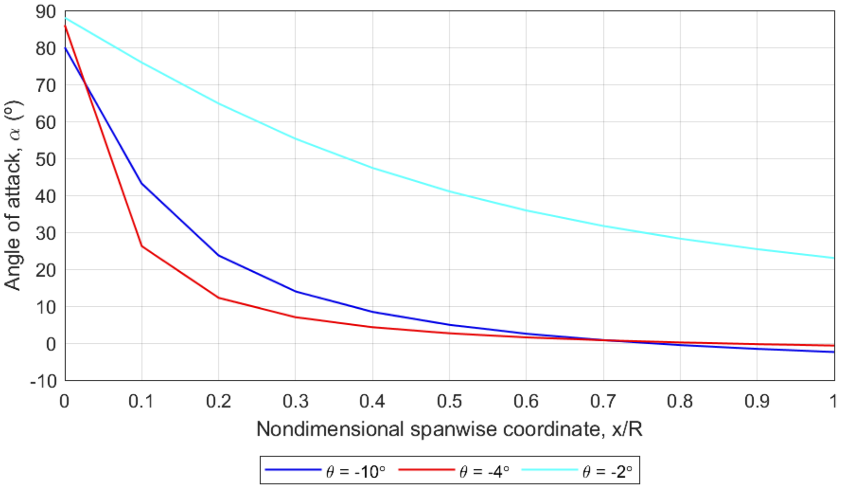

Figure 4.18: Spanwise distribution of the α of a blade's element for $\theta = -10°$, $\theta = -4°$ and $\theta = -2°$.

Apart from this, the parametric study of θ can be used to inquire the variation of the equilibrium dimensionless tip speed, $\Omega^* = 1/\lambda_{axial}$, and equilibrium C_{d_R} with θ. Figures 4.19(a) and 4.19(b), respectively, display such variations. For this specific analysis, other θ's apart from the ones referred above are considered: $-30°$, $-25°$, $-20°$, $-15°$, $-8°$, $-6°$, $-1°$ and $0°$. Note that for these extra values of θ the simulations run did not consider v_i, to avoid an excessive of computational time. Nevertheless, this assumption does not vary considerably the two specific parameters under analysis (consult appendix B for further details), so the values are trustworthy.

The same analysis was made by Smith and Levin [33], which was described on section 2.3 (see the left plot of figure 2.13) and by Modenini et al. [46] and can thus be compared qualitatively. Note that this analysis is only valid for low subsonic velocities. The NASA researchers [33] defined three regions in this graph: unstalled, stalled and unstable, with the unstable region corresponding to the range of θ's in which Ω^* and C_{d_R} are multi-valued. Modenini et al. [46] also stated the same conclusions. Figure 4.19 shows only the fully stalled and partially stalled zones, excluding the unstable operation – this happens because the model only finds one equilibrium Ω^* and C_{d_R} for the correspondent θ. However, the differences between the two stable zones are clear and the behaviour follows the one predicted by the literature. It is evident that the stall region occurs for greater values of θ, in which Ω^* and C_{d_R} present low values and with no substantial variations. On the contrary, for $\theta \leq -2.9°$ the blades are partially stalled, presenting greater values of Ω^* and C_{d_R}. With decreasing θ the values drop rapidly, with C_{d_R} becoming eventually lower in comparison to its values on a fully stalled operation. It is interesting then to notice that the values of the equilibrium C_{d_R} for $\theta = -2.8°$ and $\theta = -2°$ are higher than the one for $\theta = -10°$, serving as an explanation for the better results obtained for $\theta = -2.8°$ and $\theta = -2°$ addressed before.

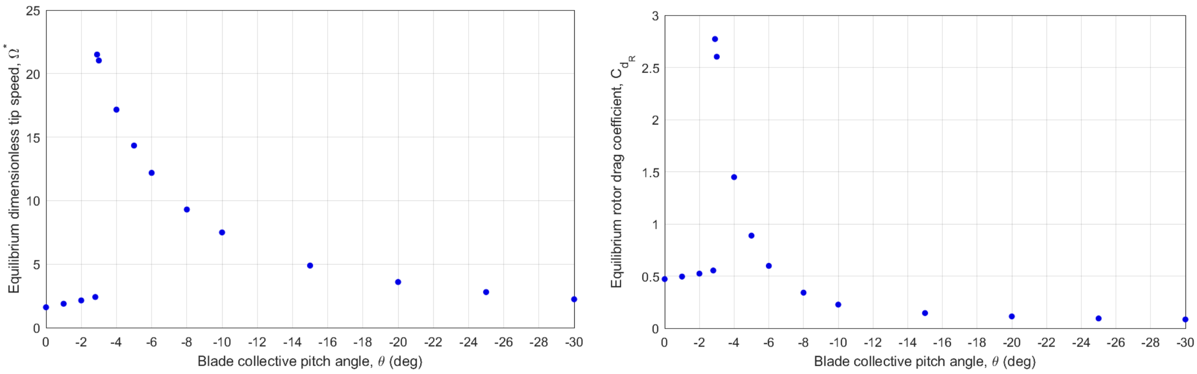

(a)

(b)

Figure 4.19: Variation of the equilibrium Ω^* (a) and C_{d_R} (b) with θ, demonstrating the clear differences between a partially stalled and fully stalled operation.

Finally, it is necessary to understand what is the most efficient θ for this specific design. For what was explained before, in the case of an autorotation operation, the ideal θ is an angle great enough to produce the required T for the deceleration, without being great enough not to disregard the generation of the sufficient Q for the rotor to initiate and maintain its rotational motion.

As referred in section 2.3, Peters et al. [44] assert that the most efficient θ is, from the set of angles that induce an unstalled operation, the highest. Seter et al. [19] state that the ultimate design point is between $\theta = 0°$ and a negative θ for which Ω^* is maximum, which is an equivalent conclusion. This is confirmed by the model, since $\theta = -2.9°$ reveals an unstalled equilibrium and the maximum Ω^* from the θ's analysed (see figure 4.19(a)), whereas $\theta = -2.8°$ was seen to result in a full stall of the blades. For this reason and taking into consideration that $\theta = -2.9°$ demonstrates the best results as for terminal v_v, it can be concluded that the most efficient angle is within the range $-2.9° \leq \theta < -2.8°$.

The terminal values of v_v and its percentage comparison with $v_{v_{deploy}}$ are present in table 4.8, confirming the conclusion stated above. An important data is taken from the table: there is a maximum velocity reduction of 64.4%. This value represents the highest decrease from the three parametric studies conducted herein and proves the importance of θ for the system. The R of the blades or N_b were not changed in this study, and yet a small variation in θ achieved better results than, for instance, the simulations for $R = 2\ m$ or $N_b = 5$. A change in θ does not result in weight penalties or differences on the dimensions of the rotor and can significantly influence the results.

Table 4.8: Values of the terminal v_v for each θ and its percentage decrease from $v_{v_{deploy}}$.

θ [°]	v_v $[m/s]$	Decrease [%]
-10	23.23	22.8
-5	13.65	54.7
-4	11.92	60.4
-3	10.78	64.2
-2.9	10.72	64.4
-2.8	16.08	46.6
-2	16.42	45.4

4.3 Genetic Optimisation

Following the parametric study, it is interesting to address the design that actually performs best - which, in this case, implies achieving the lowest terminal v_v. With this in mind, a GA can be put into practice to find an optimised solution, using the model that considers v_i, $dx = 0.1\ m$ and $dt = 0.01\ s$ for more realistic results.

In a GA the initial population and the number of generations for the optimisation need to be specified. Given the extensive computational time of the model, the GA was set to have a population of 25 individuals over 10 generations.

As described in section 3.3, the design variables, which can take integer or non integer values, and the objective function also need to be defined. Taking into account the parametric study and the results obtained therefrom, the design variables are N_b, R, c and θ (N_b is constrained to only integer values), and the only objective function is v_v, which is intended to be minimised. This means that this is a single-objective optimisation problem. Table 4.9 shows the bound constraints to each of the entry variables, which are based on the results of the parametric study of subsection 4.2.

Table 4.9: Design variables and respective bound constraints for the GA.

N_b	$R\ [m]$	$c\ [m]$	θ [°]
$[3\ ;\ 5]$	$[1\ ;\ 3]$	$[0.05\ ;\ 0.20]$	$[-5\ ;\ 0]$

Apart from these constrains, others were added to ensure that the model does not consider unintended situations, such as: c being unrealistically high and the blades having contact with each other (also dependent on N_b); the vortex ring state (see subsection 3.2.1); the blade's tip reaching Mach numbers of $M_{tip} > 0.9$ [3]. In these occasions, the GA discards the respective design.

As stated, the optimisation is comprised by a population of 25 individuals over the course of 10 generations. However, by selecting the model with v_i and low values of dx and dt, computational time was compromised. Unfortunately, even with powerful computational means, the optimisation would take roughly 10 to 15 days to run and unforeseen events occurred, which did not allow the optimisation to be concluded in two occasions. Nonetheless, one of these optimisations reached the ninth generation and it is believed that the terminal v_v would not be much more minimised.

The results of the optimisation can be observed in figure 4.20, with the minimum (best) and mean values of v_v obtained for each generation. As displayed, the minimum v_v decreases or remains constant with each generation, with the ninth generation giving a minimum of $v_v \approx 8.24\ m/s$. As for each generation's mean v_v, its tendency is also to decrease, though with some exceptions, and a lowest approximate value of $10.15\ m/s$ is seen for the ninth generation. This shows a good tendency since the mean value is, in most cases, approaching the minimum v_v as the generations progress.

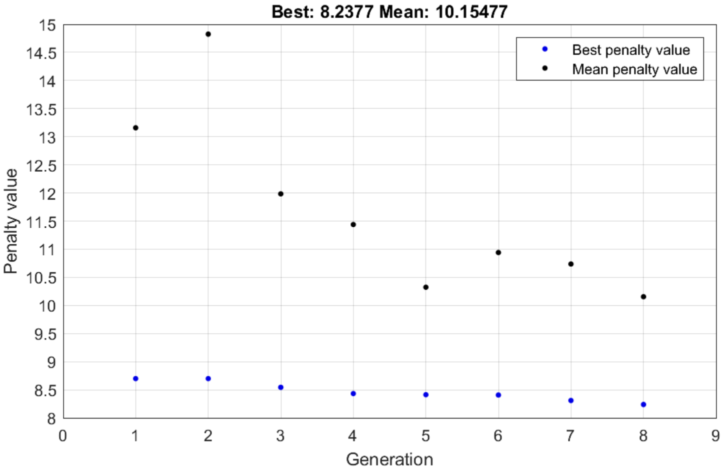

Figure 4.20: Minimum and mean values of v_v for each generation.

The design variables that produced the optimised solution are seen in table 4.10. The computed values present four decimal digits since this represents an academical solution. Nevertheless, in the case of R and c, this solution could be implemented until the millimetre if the manufacturing method was precise enough.

As indicated by the parametric study results of subsection 4.2, the $R = 1.9213\ m$ obtained is close to the best values referred, and in the same way $\theta = 2.8123°$ is in the previously stated range of $-2.9° \leq \theta < -2.8°$. This proves that the parametric studies held were not only successful, but also useful. Furthermore, $c = 0.0926\ m$ assures that the blades are not in contact with each other.

Table 4.10: Design variables that resulted in the optimised solution.

N_b	$R\,[m]$	$c\,[m]$	$\theta\,[°]$
4	1.9213	0.0926	-2.8123

Note that, as explained in section 3.3, the solution of a GA might not be the optimum one, approaching it as generations pass. Nonetheless, figure 4.20 confirms that v_v did not vary considerably with passing generations, and it is likely that the remaining two generations would not be of considerable improvements.

4.4 Optimised Solution

Considering then the values of table 4.10, a simulation was run to address the GA's solution. Figures 4.21, 4.22, 4.23, 4.24 and 4.25 display the variations of h, v_v, a_v, ω and a_{ang} with t, respectively.

The descent lasts for $t = 186.42\ s$ and, as expected, two acceleration peaks are observed. As for a_v, a first peak with a maximum of $a_v \approx 6.89\ m/s^2$ (approximately $0.70\ g$'s) is depicted, while a_{ang} has a maximum of $a_{ang} \approx 4.59\ rad/s^2$. Following the first peak, the model enters a state of equilibrium in which both accelerations are approximately null, with some variations due to previously justified reasons (see subsection 3.2.2).

As evidenced by the parametric analysis conducted, the time interval between the two acceleration peaks increases mainly with increasing R and as θ becomes more efficient. This "delay" was seen to be characteristic of designs that provided lower terminal v_v's. Such factor explains the interval of roughly 160 s ascertained between the two peaks. Thus, it is possible to conclude that, in fact, the optimised solution "delays" substantially the transition of the blades from fully stalled to partially stalled. During this period, the near-equilibrium state is maintained, though with a decrease of both v_v and ω, because of the already stated reasons.

Furthermore, the second acceleration peak results in maximum values of $a_v \approx 6.94\ m/s^2$ (approximately $0.71\ g$'s) and $a_{ang} \approx 13.86\ rad/s^2$. This results in a decrease of v_v until reaching the terminal value of $v_v \approx 8.24\ m/s$, and an increase of ω, which has a value of $\omega \approx 70.31\ rad/s$ when the model touches the ground. The recovery system is then able to reduce v_v by approximately 72.7%, which demonstrates its promising deceleration capabilities. Apart from this, the terminal ω corresponds to $M_{tip} = 0.41$, which is the maximum M_{tip} obtained, complying with the constraints of the problem.

Even though this solution leads to the minimum v_v obtained, it is seen that both the maximum a_v values at the peaks are quite low, close to $0.7\ g$'s. This can be justified by the low $DL \approx 3.16\ kg/m^2$ observed.

It is also evident that, since the second peak of acceleration occurs so late, there is not enough time for the system to reach an equilibrium state again - this becomes clear by looking at figure 4.25.

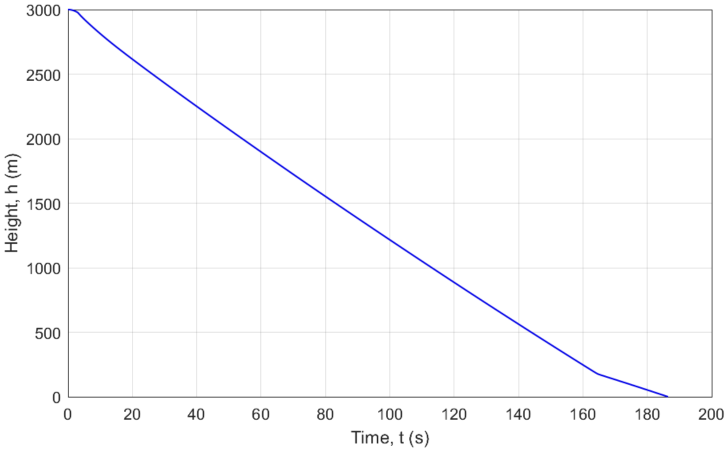

Figure 4.21: Evolution of h with t for the GA solution.

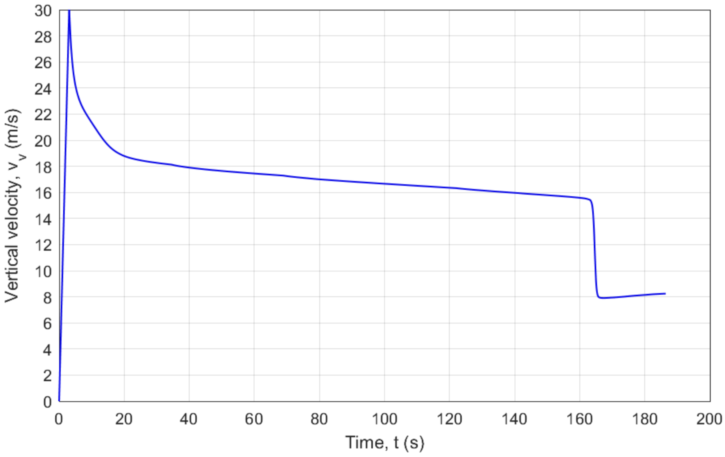

Figure 4.22: Evolution of v_v with t for the GA solution.

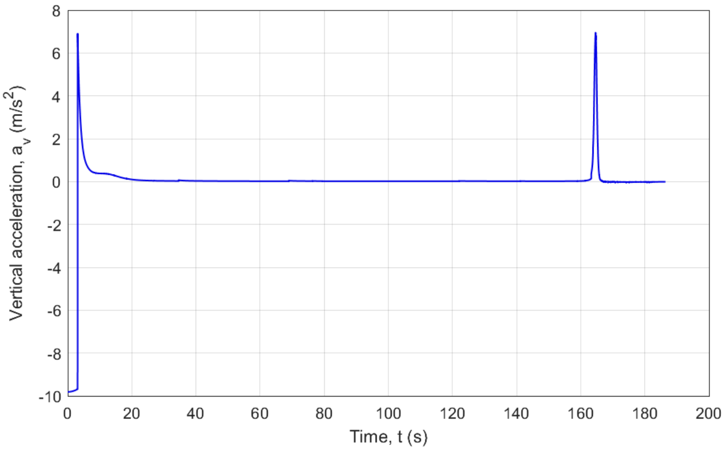

Figure 4.23: Evolution of a_v with t for the GA solution.

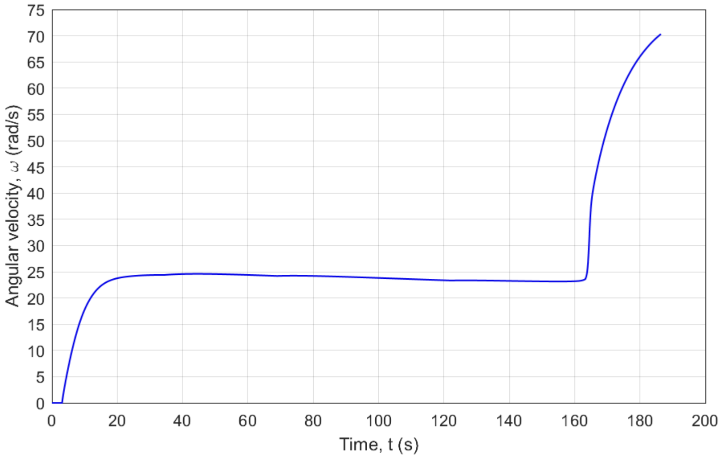

Figure 4.24: Evolution of ω with t for the GA solution.

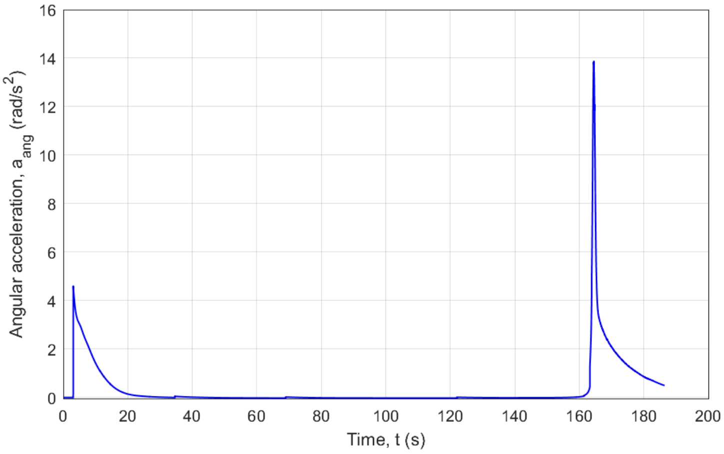

Figure 4.25: Evolution of a_{ang} with t for the GA solution.

For the reason referred above, it is not possible to address the terminal values of the rotor T and Q in order to compare them with the expected equilibrium values. However, during the near-equilibrium state between the acceleration peaks, T presents relative errors of only approximately 0.30% to 0.35% in comparison to W, and Q possesses close to zero values.

The curves of these two parameters are seen in figures 4.26(a) and 4.26(b), respectively. It is also conceivable to assess the maximum values obtained, which are $T \approx 613.35\ N$ and $Q \approx 149.16\ N \cdot m$.

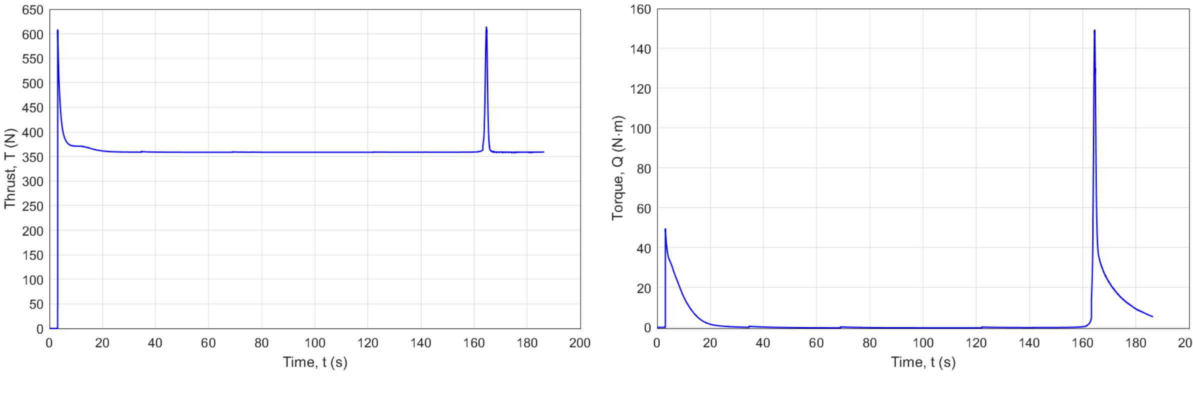

(a) (b)

Figure 4.26: Evolution of T (a) and Q (b) with t for the GA solution.

Regarding the spanwise distribution of dQ in the last moment of the simulation, observable in figure 4.27, it also does not represent an equilibrium state, for the same reasons referred above. However, it is relevant to state that the stall region in this moment is only of approximately 16% of the blade, denoting a great improvement in comparison to what was observed in figure 3.20, during the model's verification.

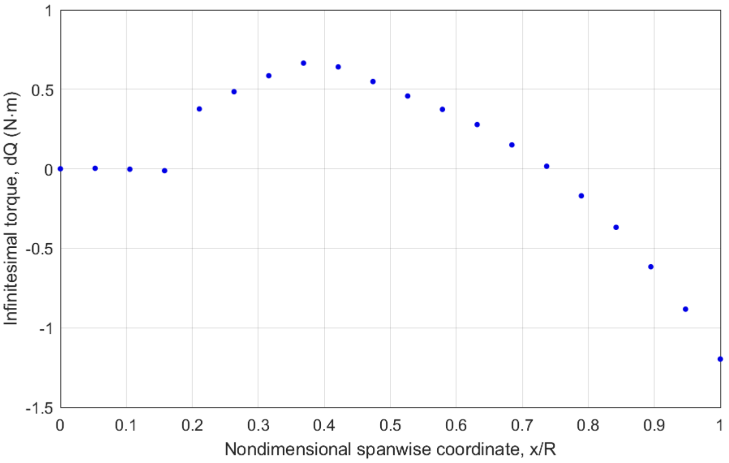

Figure 4.27: Spanwise distribution of the dQ of a blade's section in the last moment of the simulation.

Finally, the rotor C_{d_R} and λ_{axial} are subject to analysis and the correspondent plot is present in figure 4.28. First of all, it is interesting to note that the blade's operational transition, denoted by an increase on the C_{d_R}'s variation steepness, starts occurring around $\lambda_{axial} \approx 0.33$, a lower value than the ones observed until this point (see subsections 3.2.2, 4.2.2 and 4.2.3). This might indicate that a more effective and efficient design results in a lower transition λ_{axial}, something that can be confirmed by analysing figures 4.11 and 4.15, with this in mind.

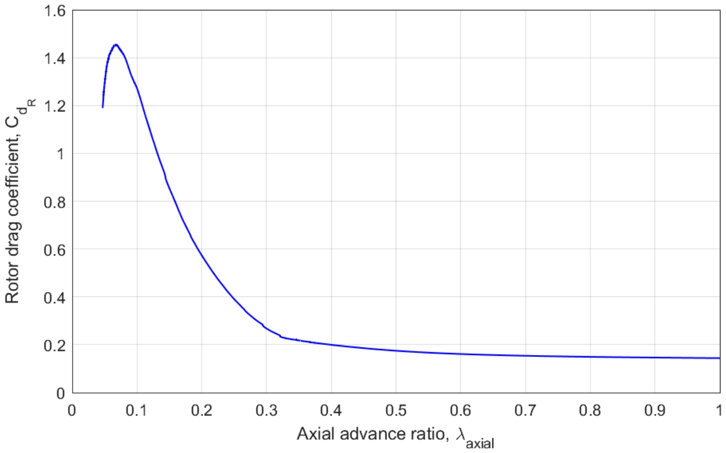

Figure 4.28: Evolution of C_{d_R} with λ_{axial} for the GA solution.

In addition, this value of $\lambda_{axial} \approx 0.33$ is also held approximately constant during the period between the two acceleration peaks and helps comprehending the reason behind the late blade's operational transition. When this value drops, C_{d_R} increases immensely, reaching a maximum value of $C_{d_R} \approx 1.45$. At last, and in the end of the simulation (not in equilibrium, though), $C_{d_R} \approx 1.19$, which is in fact a lower value than the expected C_d of the parachute designed by RED.

As for the terminal v_v objective, $v_v \approx 8.24\ m/s$ does not fulfill the design goal of $v_v = 5.95\ m/s$. Nonetheless, it must be stated that, in this optimised solution, $m_{recovery}$ is 48.15% of the gross weight, which, taking into account the literature studies cited, is highly overestimated from equation 3.18. It is also important to note that *Baltasar*'s terminal velocity in flight, decelerated by parachutes, was measured to be $v_v \approx 7\ m/s$, not achieving the goal as well.

4.4.1 Collective Flare Manoeuvre

A final study can be made in order to both solve the latter problem and demonstrate the ability of performing a collective flare manoeuvre to further reduce the v_v at touchdown.

As previously stated, the collective flare manoeuvre is put into practice by collectively changing θ to induce blade's stall, acting as flat drag plates and producing a higher deceleration at touchdown [12]. Thus, this study consists in running the model with the optimised solution, increasing θ close to the ground.

Since in this case v_v (or V_c, on the rotor's coordinate system) is anticipated to decrease to near zero values, it is expected that the windmill state condition $V_c > 2v_h$ will not be complied with, meaning that the rotor will operate in the vortex ring state. Even though the momentum theory is invalid for the vortex ring state, as described in subsection 3.2.1, this fact was neglected, since this study has merely the purpose of demonstrating the collective flare capabilities. By doing so, the unsteady and turbulent effects of the vortex ring state are ignored and, when $0 \leq V_c \leq 2v_h$, v_i is computed by resorting to equation 3.39.

This study is conducted using the optimised solution presented in subsection 4.4 with the difference that, when $h < 20\ m$, θ is varied to $\theta = 0°$.

The plots of v_v and a_v for the last seconds of the simulation are displayed in figures 4.29 and 4.30, respectively, underlining the differences of resorting to the flare manoeuvre. Understandably, the plots are coincident until $t = 184\ s$, time at which the flare manoeuvre is carried out. At this point, a_v registers a peak with a maximum of $a_v \approx 22.03\ m/s^2$ (approximately 2.24 g's) that decreases v_v to a touchdown value of $v_v \approx 3.89\ m/s$. This value is below the objective of $v_v = 5.95\ m/s$, representing a v_v decrease of 87.1% in comparison to $v_{v_{deploy}}$, and a decrease of 52.8% with regard to the terminal v_v without applying this manoeuvre. Thus, the mission would be successful regarding the terminal v_v requirement.

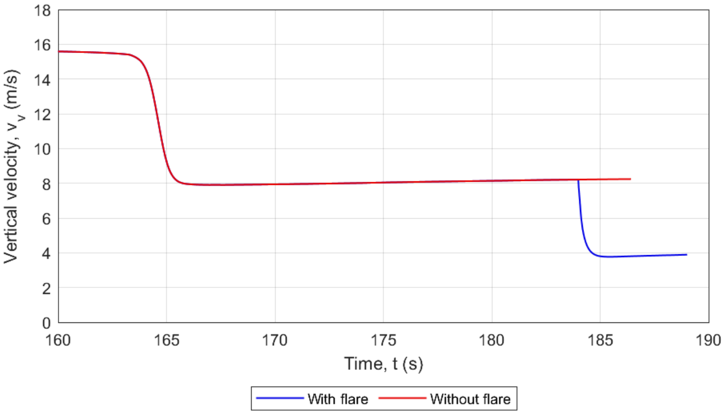

Figure 4.29: Evolution of v_v with t for the last seconds of the simulation, highlighting the effect of performing a collective flare manoeuvre.

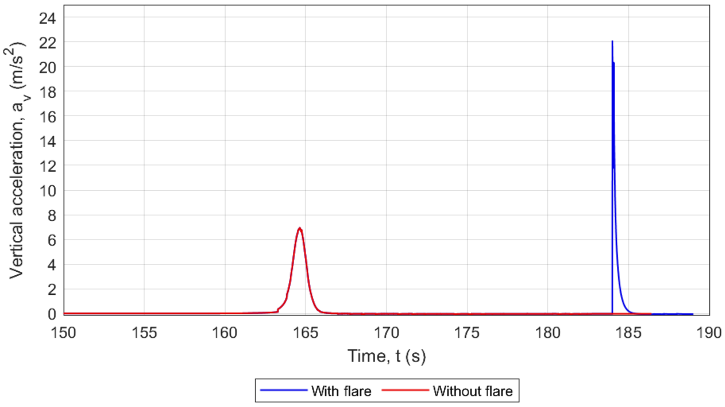

Figure 4.30: Evolution of a_v with t for the last seconds of the simulation, highlighting the effect of performing a collective flare manoeuvre.

Chapter 5

Conclusions

5.1 Achievements

In this work, the feasibility of the application of rotative wings for the recovery of spacecraft was investigated, assessing its potential in comparison to the most common recovery methods.

The work started with an extensive bibliographic study and review. In this part, autorotation studies, advances in spacecraft recovery methods over the years and, more importantly, studies on rotative wings applied to spacecraft recovery were addressed. This resulted in the conception of a compendium, which proved useful for the subsequent parts of the work.

To carry out the proposed viability analysis, a computational model that simulates the full descent of a rocket's first stage with a self-rotating rotor was developed. The model was mainly based on the BET for autorotation and on kinematics. It also contained experimental data in order to perform certain calculations and bring it closer to reality. The model was successfully verified, being confirmed to have the same behaviour of an autorotating rotor through comparisons with literature studies, though without quantitative comparisons.

A parametric study regarding the rotor's design parameters was held, leading to the following conclusions: (i) increasing N_b or blade's R results generally in a lower terminal v_v, but a too high value can be prejudicial due to the weight penalties associated; (ii) as one parameter is successively increased, the differences on the results obtained generally become smaller; (iii) the parameter's values that lead to lower v_v's also result in lower equilibrium ω's, enabling the system to maintain its steady state while avoiding blade's overspeed; (iv) blade's θ was observed to be the most defining design variable from the ones studied; (v) increasing θ generally leads to lower terminal v_v's and thus to a more efficient operation, but above a certain value the operation becomes inefficient since θ does not enable the blades to transit from being fully stalled to partially stalled; (vi) an approximate value of the θ which confers the most efficient operation was found, with a clear inefficiency being identified for θ's above this value; (vii) the more efficient the design, the more the transition from a blade's fully stalled operation to a partially stalled operation is "delayed", what leads to lower terminal v_v's. This study allowed to better comprehend the effects provoked on the system's performance by parametrically varying each design variable.

Following the parametric studies, a design optimisation was conducted in order to asses the rotor's design parameters that minimise the terminal v_v. The best design achieved a $v_v \approx 8.24\ m/s$, which reflects on a decrease of 72.7% from the initial v_v value. The performance of the system in this scenario was analysed and found to be realistic and promising.

Finally, the collective flare manoeuvre for touchdown was demonstrated so that the terminal v_v goal of $v_v = 5.95\ m/s$ was reached. This study was successful, with a further decrease of 52.8% on the terminal v_v in comparison to the best design presented, what represents a total decrease of 87.1%, without considering the vortex ring state's unstable effects, though. Such analysis confirms the potential capabilities of this manoeuvre, concluding that it is possible to safely land and recover the spacecraft.

To conclude, although a number of approximations and assumptions have been made, this proof of concept confirmed that it is feasible to resort to rotative wings to safely recover a rocket's first stage, with regard to its terminal v_v. Moreover, the proposed objectives were accomplished successfully.

The rotative wings recovery system presents advantages that make it extremely interesting in comparison to the most commonly used systems, especially regarding its versatility, and shows potential. However, and understandably, many other studies are still required, especially regarding stability, to fully address its feasibility.

5.2 Future Work

The model developed for this work, as described, is theoretical but contains computational and experimental data in order to improve the accuracy of the results. Nevertheless, being a proof of concept, some assumptions and approximations made can be improved in order to bring the model even closer to reality. In addition, further analysis in other fields of study are mandatory in order to completely comprehend this recovery method and fully address its viability. Thus, future work regarding this model and the study of the recovery system itself include:

- **Different blade's designs -** this thesis considered a rectangular blade shape, which is the simplest, and the NACA 0012 airfoil, a common choice in rotors. Nonetheless, different blade's shapes and airfoils should be studied in order to achieve an optimum result for this purpose. Moreover, the blade's were designed to have no twist, something that can bring even better results [52];

- **Inclusion of the vortex ring state's effects -** it was described that the vortex ring state provokes unstable aerodynamic flows from tip vortexes that can not be predicted by the theory [9]. Thus, it would be interesting to address such problem and, if possible, add its effects to the model;

- **Perform a CAD model of the system -** the conception of the rotor's CAD model would allow for more trustworthy values of I_{rotor} and m_{rotor} to be used in the calculations. Furthermore, this model (or the rotor plus first stage assembly's model) could be used for further CFD simulations;

- **Conduction of CFD and model's wind tunnel tests -** the testing of the system in CFD simulations or the testing of a model in a wind tunnel would be an asset so that the results obtained could be confirmed and compared quantitatively, especially for the measurements of the rotor's T, Q and ω;

- **Airfoil's wind tunnel testing at high angles of attack -** this work considered computational and experimental data for the NACA 0012 airfoil, for a wide range of α's. However, additional tests can be held in order to obtain an even better database of C_l and C_d for a wide range of Re;
- **Stability studies -** the literature studies of chapter 2 report several problems found on the dynamic stability of the models [12, 31, 37]. In addition, other instabilities on the vehicle related to the deployment of the blades or its overspeed are also mentioned [2]. This part of the work was not within the scope of this thesis and hence was not studied. Nevertheless, future studies in this field can eventually erase the doubts regarding the system's stability and are of extreme importance;
- **Inclusion of supersonic/hypersonic conditions -** in order to study the rotor's operation during re-entry, the model must consider supersonic and hypersonic velocities and the aerodynamic effects associated, such as shock waves. This adds a substantially higher degree of complexity and was not considered for this feasibility study, since the rotor can operate only at subsonic velocities and still accomplish the mission [2]. However, as a future enhancement, it would be interesting to simulate other situations such as the re-entry, descent and landing of a real size rocket, like the Falcon 9's first stage, allowing to draw direct comparisons with the controlled vertical landing;
- **Development of a θ control model -** in this thesis the blade's θ was assumed to be constant throughout the blade and during the simulation, only being varied in a simulation in order to perform the collective flare manoeuvre. Nonetheless, controlling θ is extremely important to maintain ω on a certain range, avoiding under or overspeed of the blades. In addition, the cyclic pitch, which is meaningful at supersonic velocities [37] and during a subsonic glide flight [12], requires the implementation of a control model to be studied, since θ varies from blade to blade;
- **Inclusion of the blade's flapping motion -** the flapping of the blades is particularly relevant in forward flight, with the blades periodically flapping up and down depending on the blade's position [9]. This improvement would enable to study the effects of coning angle, but more significantly of horizontal motion;
- **Inclusion of horizontal motion (glide) -** in order to address the full potential of the rotary wings recovery system, it is also important to analyse the gliding operation on the system. During the work herein presented, there were several tries to include such motion in the developed model. It was verified that the blades were performing according to what was expected and that the system achieved an autorotation equilibrium state. Nevertheless, v_v would increase, contrarily to the predictions. Thus, it was concluded that a cyclic control of θ would be necessary for this model to obtain the intended results, and such improvement was out of the scope of this master's thesis. Furthermore, considering flapping effects would also be a requirement in this part of the work;
- **Inclusion of the rotor's deploy -** performing the modelling of the blade's deploy event would be an asset of interest, allowing to study the rotor's performance during this moment;
- **Cost analysis -** a cost analysis of the system and its mission would be required in the future to assess if rotative wings are financially sustainable in comparison to the other methods.

Bibliography

[1] R. D. Launius and D. R. Jenkins. *Coming home: reentry and recovery from space (1st ed.)*. U.S. National Aeronautics and Space Administration, 2012.

[2] J. D. Hagen. Rotor Landing Technology for Crew Exploration Vehicle (CEV) Earth-to-Orbit Crew Transport. In *1st Space Exploration Conference: Continuing the Voyage of Discovery, AIAA 2055-2508*, 2005.

[3] EADS Astrium. *AMDL: Auto-Rotation in Martian Descent and Landing*. ESA Contract No. 21233/07/NL/CB, 2009.

[4] G. C. Hudson. Roton development and flight test program. In *AIAA Defense and Civil Space Programs Conference and Exhibit, AIAA 98-5258*, Huntsville, AL, U.S.A., October 1998.

[5] SpaceX. Mission, 2022. URL `https://www.spacex.com/mission/`. (Accessed on 19-08-2022).

[6] L. A. Davis. First Stage Recovery. *Engineering, Vol. 2*, pages 152–153, 2016.

[7] G. P. N. T. Breitinger, B. S. Aichele and R. Raja. Vertical Landing Rockets. In *TMAL02*, Linköping University, 2018.

[8] SKYbrary. Autorotation, 2015. URL `https://skybrary.aero/articles/autorotation`. (Accessed on 7-04-2022).

[9] J. Gordon Leishman. *Principles of helicopter aerodynamics (2nd ed.)*. Cambridge University Press, 2006.

[10] Federal Aviation Administration. *Helicopter Flying Handbook: FAA-H-8083-21B*. Aviation Supplies & Academics, Inc., 2019.

[11] A. Filippone. *Flight Performance of Fixed and Rotary Wing Aircraft (1st ed.)*. Cambridge University Press, 2006.

[12] Kaman Aircraft Corporation. *Investigation of Stored Rotors for Recovery*. Technical Documentary Report No. ASD-TDR-63-745, 1963.

[13] R. C. Smith and A. D. Levin. The unpowered rotor: a lifting decelerator for spacecraft recovery. In *AIAA Aerodynamic Deceleration Systems Conference*, El Centro, CA, U.S.A., September 23-25 1968.

[14] T. Steiner and L. A. Young. Rotary Wing Decelerator Use on Titan. In *8th International Planetary Probe Workshop*, Portsmouth, VA, U.S.A., June 2011.

[15] M. Kretz. *Space Rotor - A French Concept for a Reusable Recovery System*. SAE Technical Paper 670391, 1967.

[16] J. Gordon Leishman. Development of the autogiro: A technical perspective. *Journal of Aircraft, Vol. 41 No. 4*, 2004.

[17] M. Munk. *Model tests on the economy and effectiveness of helicopter propellers*. National Advisory Commitee for Aeronautics, Technical note No. 221, 1925.

[18] Bruce H. Charnov. Rediscovering the Autogiro: Cierva, Pitcairn and the Legacy of Rotary-Wing Flight. Hofstra University, 2016.

[19] D. Seter and A. Rosen. Theoretical and Experimental Study of Axial Autorotation of Simple Rotary Decelerators. *Journal of Aircraft, Vol. 51, No. 1*, pages 236–248, 2014.

[20] A. Azuma and K. Yasuda. Flight Performance of Rotary Seeds. *Journal of Theoretical Biology, Vol. 138*, pages 23–53, 1989.

[21] NASA. Throwback to Apollo Parachute Testing, 2018. URL `https://www.nasa.gov/mediacast/throwback-to-apollo-parachute-testing`. (Accessed on 3-08-2022).

[22] NASA. Space Shuttle: Solid Rocket Boosters, 2006. URL `https://www.nasa.gov/returntoflight/system/system_SRB.html`. (Accessed on 3-08-2022).

[23] NASA. Space Shuttle Image Gallery, 2017. URL `https://www.nasa.gov/mission_pages/shuttle/images`. (Accessed on 3-08-2022).

[24] SpaceX. Starship, 2022. URL `https://www.spacex.com/vehicles/starship/`. (Accessed on 19-08-2022).

[25] SpaceX. Official SpaceX Photos, 2022. URL `https://www.flickr.com/photos/spacex/`. (Accessed on 19-08-2022).

[26] Igor B. Bensen. *Performance of a Rotary Wing Air Brake in Supersonic Flow*. General Electric, Report No. 55260, 1947.

[27] V. E. Lockwood. *High-speed Drag and Opening Characteristics of a Kaman Rotochute Model*. NACA, 1954.

[28] Norman D. Ham. An Experimental and Theoretical Investigation of a Supersonic Rotating Decelerator. *Journal of American Helicopter Society, Vol. 8 No. 1*, pages 8–18, 1963.

[29] Justin J. Barzda. Rotors for Recovery. In *AIAA Entry Technology Conference*, Williamsburg and Hampton, VA, U.S.A., 1964.

[30] Charles E. Libbey. Rotary-Type Recovery Systems. In *Langley Research Center compilation of papers presented to meeting on space vehicle landing and recovery research and technology*, NASA HQ, 1962.

[31] R. A. Diaz-Silva, M. M. Sarigul-Klijn and N. Sarigul-Klijn. Rotary Decelerators for Spacecraft: Historical Review and Simulation Results. In *AIAA Space Conferences and Exposition*, San Diego, CA, U.S.A., 2013.

[32] M. Kretz. *Device for Ensuring the Re-entry into the Atmosphere and the Recovery of Space Vehicles*. US Patent # 3,412,807, 1968.

[33] A. D. Levin and R. C. Smith. *An analytical investigation of the aerodynamic and performance characteristics of an unpowered rotor entry vehicle*. NASA Ames Research Center, NASA TN D-4537, 1968.

[34] R. C. Smith and A. D. Levin. *Experimental Aerodynamic Performance Characteristics of a Rotor Entry Vehicle Configuration. 1 - Subsonic*. NASA TN D-7046, 1971.

[35] R. C. Smith and A. D. Levin. *Experimental Aerodynamic Performance Characteristics of a Rotor Entry Vehicle Configuration. 2 - Transonic*. NASA TN D-7047, 1971.

[36] R. C. Smith and A. D. Levin. *Experimental Aerodynamic Performance Characteristics of a Rotor Entry Vehicle Configuration. 3 - Supersonic*. NASA TN D-7048, 1971.

[37] R. C. Smith and A. D. Levin. Experimental Aerodynamics of a Rotor Entry Vehicle. In *AIAA Aerodynamic Deceleration Systems Conference*, El Centro, CA, U.S.A., September 23-25 1968.

[38] R. V. S. M. Sarigul-Klijn, B. Binnie and D. P. Gump. Safety and the Roton Development Program. In *1999 IEEE Aerospace Conference. Proceedings (Cat. No.99TH8403)*, 1999.

[39] L. A.Young, E. W. Aiken, M. R. Derby, R. Demblewski and J. Navarrete. Experimental Investigation and Demonstration of Rotary-Wing Technologies for Flight in the Atmosphere of Mars. In *58th Annual Forum of the AHS, International*, Montreal, Canada, June 2002.

[40] L. A.Young, G. Briggs, E. W. Aiken and G. Pisanich. Rotary-wing decelerators for probe descent throught the atmosphere of venus. In *2nd International Planetary Probe Workshop*, NASA Ames Research Center, Moffett Field, CA, U.S.A., August 2004.

[41] J. Moore. Nasa engineers test rotor reentry, 2012. URL `https://www.aopa.org/news-and-media/all-news/2012/november/13/nasa-engineers-test-rotor-reentry`. (Accessed on 24-06-2022).

[42] A. Brindejonc, J. Sirohi and I. Chopra. Rotary-wing Decelerators for Probe Descent Throught the Atmosphere of Venus. In *61st Annual Forum of the American Helicopter Society International*, Grapevine, TX, U.S.A., 2007.

[43] R. Cadenas, T. Peters, M. Graziano, D. Modenini, GM Saggiani, P. Tortora, E. Kervendal and J. Kohler. Beyond current EDL Technologies on Mars: Evaluation of ARMADA Concepts. In *10th workshop on advanced space technologies for robotics and automation ASTRA*, 2008.

[44] T. V. Peters, R. Cadenas, D. Modenini, P. Tortora, E. Kervendal and J. Kohler. ARMADA: Autorotation, feasible alternative to traditional Martian Entry, Descent and Landing. In *60th International Astronautical Congress*, 2009.

[45] D. Modenini, A. Rossetti, A. Talamelli. Aerodynamic assessment of a rotary entry vehicle for Mars landing: an experimental analysis. *Meccanica, Vol. 54, No. 7*, pages 967–984, 2019.

[46] D. Modenini, M. Zannoni and P. Tortora. Optimal Blade Pitch Profile for an Autorotative Entry Vehicle. *Advances in the Astronautical Sciences Series, Vol. 162*, page 765–776, 2018.

[47] C. Riegler, I. Angelov, F. Kohmann, T. Neumann, A. Bilican, T. Appelt ... R. Rath. Project Daedalus, Rotor Controlled Descent and Landing on REXUS23. In *23rd ESA PAC Symposium*, June 2019.

[48] Johanna Mehringer, Lennart Werner, Clemens Riegler and Frederik Dunschen. Suborbital Autorotation Landing Demonstrator on REXUS 29. In *4th Symposium on Space Educational Activities*, Barcelona, Spain, April 2022.

[49] Jan M. Wolf, Lennart Werner, Philip Bergmann, Clemens Riegler, and Frederik Dunschen. Electronics and Sensor Subsystem Design for Daedalus 2 on REXUS 29: An Autorotation Probe for Sub Orbital Re-Entry. In *25th ESA Symposium on European Balloons and Rockets Programmes and related Research*, Biarritz, France, May 2022.

[50] N. Hall. Inclination Effects on Lift, 2021. URL `https://www.grc.nasa.gov/www/k-12/airplane/incline.html`. (Accessed on 28-03-2022).

[51] John D. Anderson, Jr. *Fundamentals of Aerodynamics (6th ed.)*. McGraw-Hill, 2017.

[52] N. Amato, Z. Huamán, A. Hyland, J. Koslow, J. Pickunka, J. Procaccini ... J. Tappen. *Design, Analysis, and Test of a High-Powered Model Rocket*. Partial Fulfillment of the Requirements for the Degree of Bachelor of Science in Aerospace Engineering, Worcester Polytechnic Institute, 2020.

[53] H. P. Kritzinger, C. R. Kleijn and H. E. A. Van den Akker. Drag on a Confined Cylinder in Axial Flow. In *ASME-PVP Symposium on Computational Technologies for Fluid/Thermal/Structural/Chemical Systems with Industrial Applications*, San Diego, CA, U.S.A., July 2004.

[54] CCMC Metadata Registry. NRLMSIS Atmosphere Model, 2020. URL `https://kauai.ccmc.gsfc.nasa.gov/instantrun/msis`. (Accessed on 9-05-2022).

[55] André Deperrois. Part IV - Theoretical limitations and shortcomings of xflr5, 2019. URL `http://www.xflr5.tech/docs/Part%20IV:%20Limitations.pdf`. (Accessed on 3-04-2022).

[56] C. C. Critzos, H. H. Heyson and R. W. Boswinkle, Jr. *Aerodynamic characteristics of NACA 0012 airfoil section at angles of attack from* $0°$ *to* $180°$. National Advisory Commitee for Aeronautics, Technical note No. 3361, 1955.

[57] R. E. Sheldahl and P. C. Klimas. *Aerodynamic Characteristics of Seven Symmetrical Airfoil Sections Through 180-Degree Angle of Attack for Use in Aerodynamic Analysis of Vertical Axis Wind Turbines*. Sandia National Laboratories, Technical report No. SAND-80-2114, 1981.

[58] J. M. Rainbird, J. Peiró and J. M. R. Graham. Blockage-tolerant wind tunnel measurements for a NACA 0012 at high angles of attack. *Journal of Wind Engineering and Industrial Aerodynamics, Vol. 145*, pages 209–218, 2015.

[59] F. P. Beer, E. R. Johnston, Jr., D. F. Mazurek, P. J. Cornwell, B. P. Self. *Vector Mechanics for Engineers: Statics and Dynamics (12th ed.)*. McGraw Hill, 2018.

[60] Joaquim R. R. A. Martins and Andrew Ning. *Engineering Design Optimization (1st ed.)*. Cambridge University Press, 2021.

[61] AeroTéc. Rocket Experiment Division, 2022. URL `https://aerotec.pt/red`. (Accessed on 8-09-2022).

Appendix A

Model Flowchart

In order to better follow how the developed model works, a flowchart was conceived. The referred chart can be seen in figure A.1 and describes the framework of the model, which is extensively explained in chapter 3.

This flowchart only refers to the descent's part following the deployment of the rotor. Apart from this, the model herein represented is the model that uses v_i, since it has a more complex logic than the model that does not consider it.

The scheme presented in this appendix is merely illustrative for the comprehension of the code's logic, and misses some important parts of the code such as: initial design variables, the input of certain data, the functions that allow to create the smoothing splines for the plot of the curves of C_l and C_d or the atmosphere parameters, or the further calculation of parameters such as C_{d_R} and λ_{axial} for performance analysis. Nevertheless, the calculations and functions here observed assist on understanding the most complex part of the model's code and allow its reproduction.

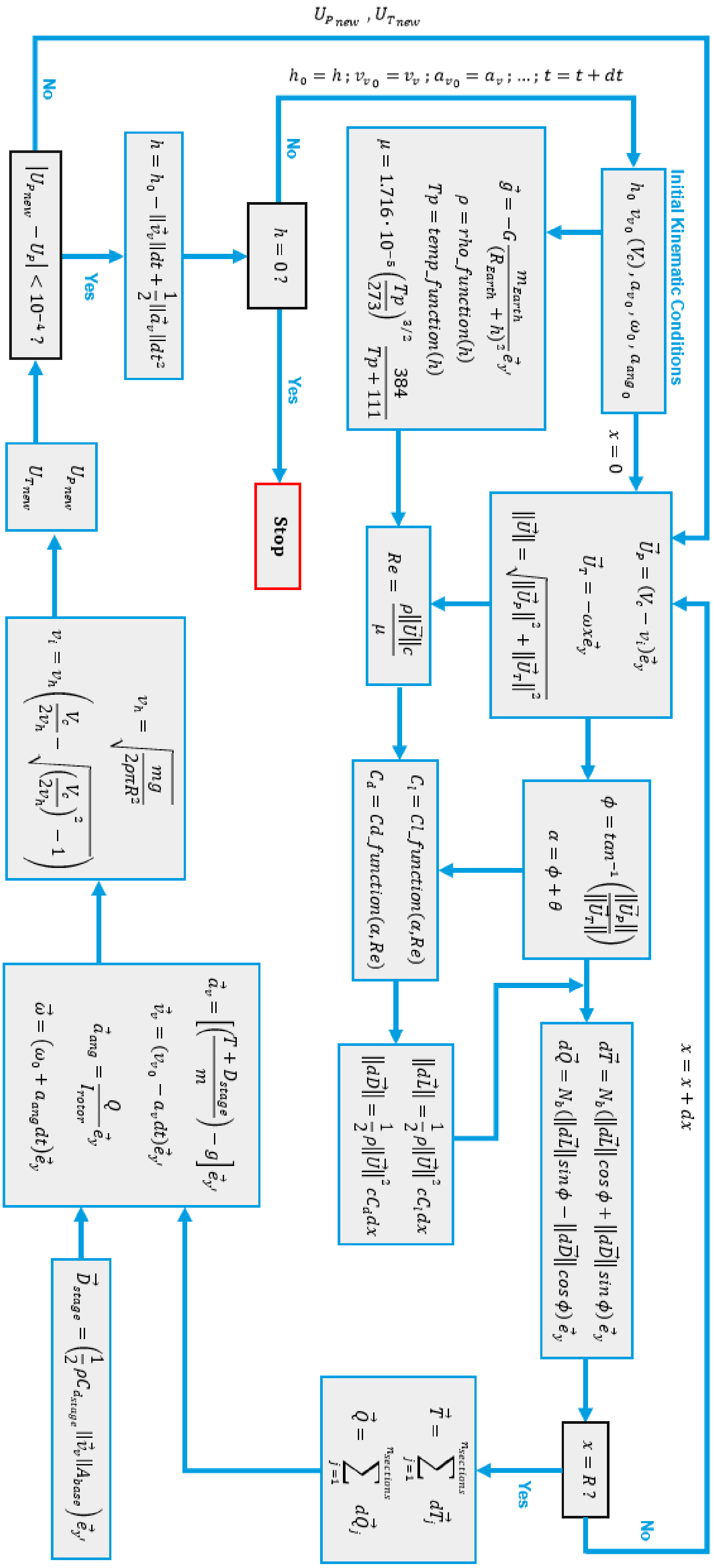
Initial Kinematic Conditions
h_0 v_{v_0} (V_c), a_{v_0}, ω_0, a_{ang_0}
x = 0
No
Yes
x = x + dx
x = R ?
h = 0 ?
Stop
|U_{P_new} − U_P| < 10^{-4} ?
U_{P_new} , U_{T_new}
h_0 = h ; v_{v_0} = v_v ; a_{v_0} = a_v ; … ; t = t + dt
ρ = rho_function(h)
Tp = temp_function(h)
C_l = Cl_function(α, Re)
C_d = Cd_function(α, Re)

Figure A.1: Flowchart representing the model's framework following the deployment of the rotor.

Appendix B

Axial Induced Velocity Study

As an additional part of this work, it is interesting to address the effect that v_i has on the results provided by the system. Despite meaning more accurate results, the inclusion of v_i is associated with an extensive raise of the model's computational time. For this reason, for certain cases it might be favourable to disregard this velocity. However, it is important to understand the differences provoked in the results by ignoring v_i, to comprehend when it is acceptable to make such assumption.

With this in mind, a simulation was run with the same mesh parameters and initial conditions as the ones utilised for the model's verification of subsection 3.2.2, but in this case without considering v_i. Figures B.1 and B.2 show the plots of v_v and a_v with t, respectively, highlighting the differences between running the model with and without v_i. Considering that the model that considers v_i provides more accurate results and using its values as a reference, the observed difference in terminal v_v is of approximately $1.20\ m/s$, representing an error of 4.9%. Curiously, the final value of v_i registered in the simulation of subsection 3.2.2 is of $v_i \approx 1.20 m/s$, being exactly the same value of the difference observed. This was also verified in other simulations run throughout this work.

On the other side, the error in the maximum a_v is around 12.2%. It is also seen that the model without v_i overpredicts the deceleration and thus results in a lower terminal v_v, what would be deceptive.

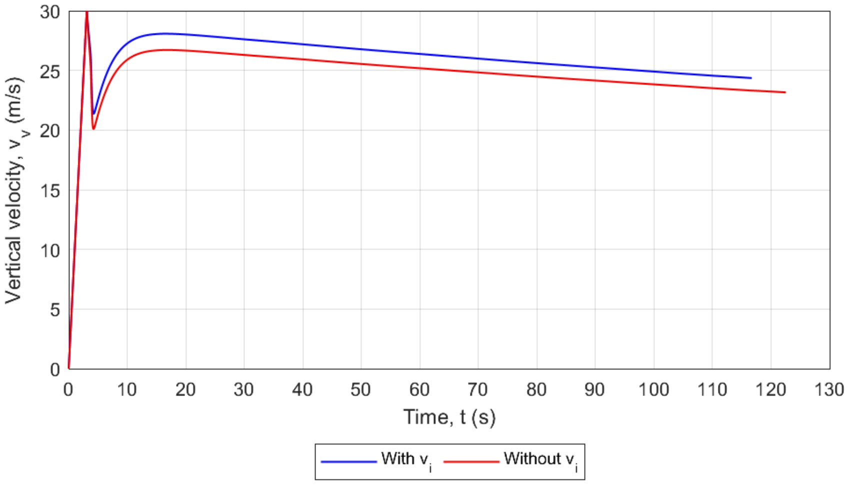

Figure B.1: Evolution of v_v with t for the v_i study.

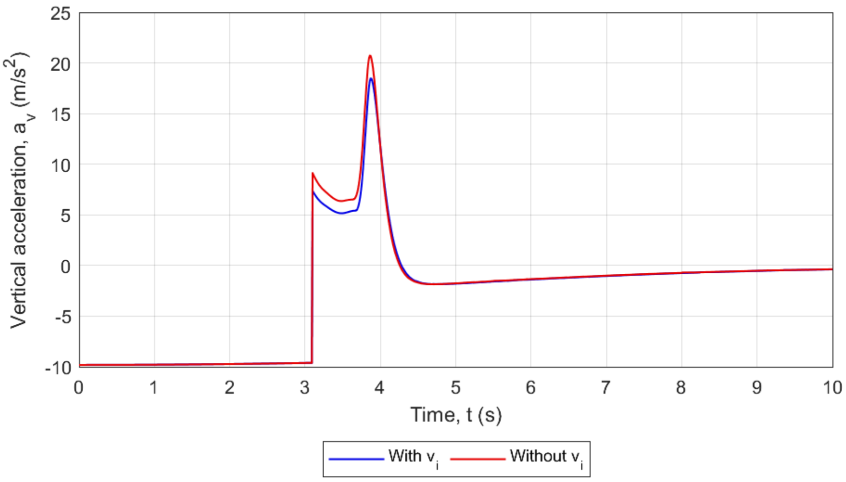

Figure B.2: Evolution of a_v with t in the first seconds of the simulation, for the v_i study.

Accordingly, the model that does not consider v_i predicts an excessive a_{ang} and consequently ω, which can be observed in figures B.4 and B.3, respectively. Nonetheless, this model overpedicts the terminal ω by only 0.04% and the maximum a_{ang} by approximately 7.9%.

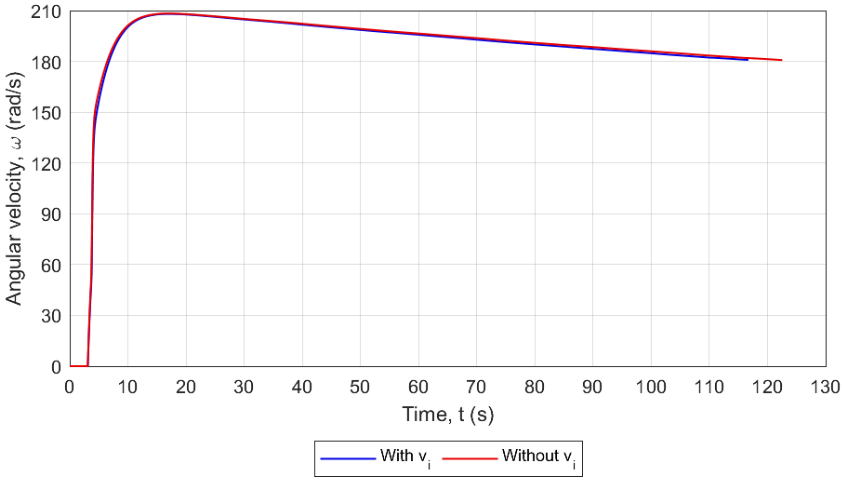

Figure B.3: Evolution of ω with t for the v_i study.

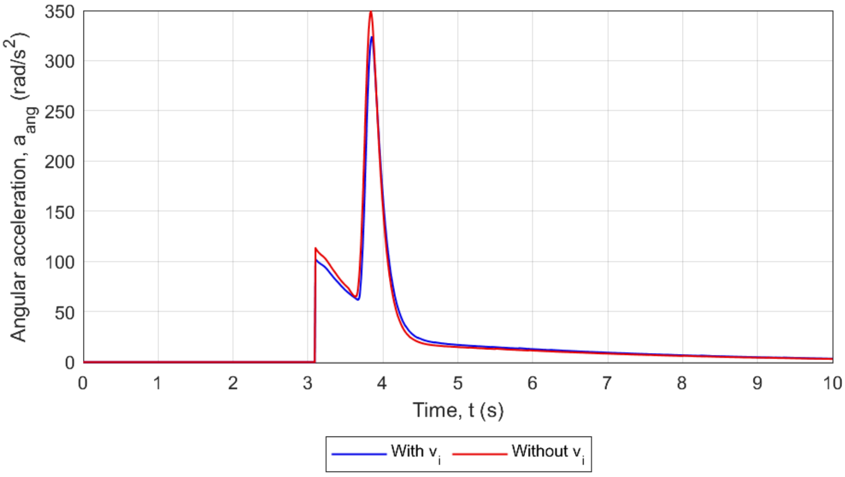

Figure B.4: Evolution of a_{ang} with t in the first seconds of the simulation, for the v_i study.

It goes without saying that T and Q behave accordingly to a_v and a_{ang}, respectively.

Finally, regarding the evolution of C_{d_R} with λ_{axial}, present in figure B.5, it is seen that the differences are also negligible. For the maximum C_{d_R}, an error of approximately 2% is obtained, while for its equilibrium value there is an error of only approximately 0.16%. As for the equilibrium λ_{axial}, the relative error computed was of 0.04%.

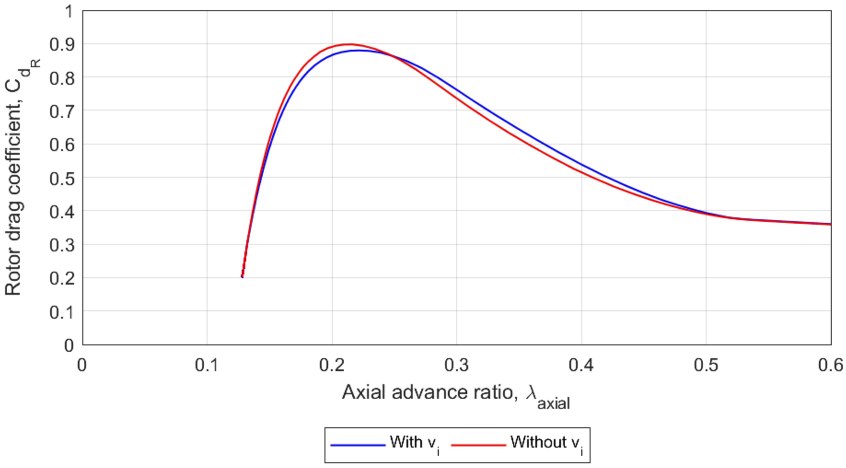

Figure B.5: Evolution of C_{d_R} with λ_{axial} for the minimised solution.

The errors computed are not substantial. Yet, they reduce the results' reliability. For this reason, it is concluded that the model should be run considering v_i. However, if for a certain simulation the computational time is overly jeopardised and the decision is to disregard v_i, the differences obtained in the results would not be worrying. This was the case of one specific study in subsection 4.2.3 - since many simulations had to be run to obtain certain points of figure 4.19, and since the errors observed above for C_{d_R} and λ_{axial} were low, it was decided to disregard v_i for those simulations.